THESIS

TECHNOECOMONIC OPTIMIZATION AND WORKING FLUID SELECTION FOR AN ENGINE COOLANT DRIVEN TURBO-COMPRESSION COOLING SYSTEM

Submitted by

Derek Nicholas Young

Department of Mechanical Engineering

In partial fulfillment of the requirements

For the Degree of Master of Science

Colorado State University

Fort Collins, Colorado

Summer 2018

Master's Committee:

Advisor: Todd M. Bandhauer

Jason C. Quinn
Jesse Burkhardt

ABSTRACT

TECHNOECOMONIC OPTIMIZATION AND WORKING FLUID SELECTION FOR AN ENGINE COOLANT DRIVEN TURBO-COMPRESSION COOLING SYSTEM

The abundance of low grade waste heat presents an opportunity to recover typically unused heat energy and improve system efficiencies in a number of different applications. This work examines the technoeconomic performance of a turbo-compression cooling system designed to recover ultra-low grade (≤ 100°C) waste heat from engine coolant in large marine diesel engine-generator sets. In addition, five different working fluids (R134a, R152a, R245fa, R1234ze(E), and R600a) were studied for this application to better understand the effects of fluid properties on technical and economic system performance. A coupled thermodynamic, heat exchanger, and economic model was developed to calculate the payback period of the turbo-compression cooling system. Then, the payback period was minimized by optimizing the surface area of the heat exchangers by varying the effectiveness of the heat exchangers. The sensitivity of the payback period to the heat exchanger effectiveness values was quantified to inform future design considerations. The turbo-compression cooling system with R152a had the lowest payback period of 1.67 years and an initial investment of $181,846. The R1234ze(E) system had the highest cooling capacity of 837 kW and the highest overall COP of 0.415. The R152a system provided cooling for $0.0060 per kWh which was nearly 10 times cheaper than the cost of cooling provided by a traditional electrically driven vapor compression system onboard a marine vessel.

ACKNOWLEDGEMENTS

I would like to first thank Dr. Todd Bandhauer for providing guidance and his expert opinions throughout my graduate career. Every day is interesting while working for Dr. Bandhauer because of his unending excitement for thermal sciences. He truly took a chance on me when I came to CSU because I didn’t know a thing about engineering. I appreciate his patience as I was coming up to speed the first two semesters (and beyond). I’m truly lucky to have him as a mentor! This short paragraph cannot do justice to how much he has influenced me.

I’d also like to thank the other graduate students in the ITS Lab, specifically Shane Garland, David Hobby, John Simon, Alex Grauberger, Spencer Gibson, and Torben Grumstrup. If I could put second authors on this thesis, I would. The hours upon hours we’ve spent bouncing ideas off each other (some really, really dumb ideas that led us to great ones) has been so important and helpful to me. Understanding different perspectives in solving the same problem has helped me grow as an individual and an engineer.

In addition, I’d like to give a shout out to some individuals at the Powerhouse Energy Campus: the Control Room Crew, Colin Gould, John Mizia, Andrew Zdanowicz, Chris van Roekel, Betsy Farris, Adam Friss, Max Flagge, and many more that I haven’t listed here (sorry, I have to send this thesis to Dr. B in ~30 minutes). When you work surrounded by great friends, it makes the work a lot more enjoyable. Further, the grassroots movement known as the Energy Institute Sports League (EISL) has been a great stress reliever and community builder for the last year or so.

I’d also like to thank my family and friends. Without your unending love and support, I wouldn’t be half the person I am today. Mom, Dad, G, L-Dog: thank you all so much. I love you guys with everything I have! I’d also like to thank Kendyl ‘*Kenny G’* Kelly: you are the best I could ask for! I appreciate your sense of adventure, compassion, and calming presence. I love ya a whole ton.

TABLE OF CONTENTS

LIST OF TABLES

LIST OF FIGURES

NOMENCLATURE

Variable	**Description**	**Units/Formula**
$\dot{Q}$	Heat transfer rate	W
$\dot{m}$	Mass flow rate	kg s^{-1}
c_{p}	Specific heat capacity	J kg^{-1} K^{-1}
T	Temperature	°C
i	Enthalpy	W kg^{-1}
C	Heat capacity rate	W K^{-1}
$\dot{W}$	Power	W
Ns	Dimensional specific speed	$ft^{3/4}$ $lbm^{3/4}$ min^{-1} $s^{-1/2}$ $lbf^{-3/4}$
N	Rotational speed	rev min^{-1}
$\dot{V}$	Volumetric flow rate	ft^3 s^{-1}
H	Head rise	ft lbf lbm^{-1}
Ds	Dimensional specific diameter	$lbf^{1/4}$ $s^{1/2}$ $lbm^{-1/4}$ $ft^{-1/4}$
D	Diameter	m (or ft)
COP	Coefficient of performance	-
NTU	Number of transfer units	-
Cr	Heat capacity rate ratio	-
U	Overall heat transfer coefficient	W m^{-2} K^{-1}
A	Area	m^2
N_{plate}	Number of plates	-
w_{plate}	Width of plates	m
h	Heat transfer coefficient	W m^{-2} K^{-1}
R_{wall}	Wall thermal resistance	m^2 K W^{-1}
Co	Convection number	$Co=\left(\rho_{\mathrm{g}}/\rho_{\mathrm{l}}\right)\left(\left(1-x\right)/x\right)^{0.8}$
Fr	Froude number	$Fr=G^2/\left(\rho^2 gD_{\mathrm{hyd}}\right)$
Bo	Boiling number	$Bo=q''/Gi_{\mathrm{fg}}=A_{\mathrm{c}}/A_{\mathrm{plate}}$
k	Thermal conductivity	W m^{-1} K^{-1}
Re	Reynolds number	$Re=4\dot{m}/P\mu$
Pr	Prandtl number	$Pr=c_{\mathrm{p}}\mu/k$
u	Velocity	m s^{-1}
L	Length	m
P	Wetted perimeter	m
ρ	Density	kg m^{-3}
x	Quality	-
G	Mass flux	kg m^{-2} s^{-1}
g	Acceleration from gravity	m s^{-2}

q''	Heat flux	W m^{-2}
i_{fg}	Enthalpy of vaporization	J
f	Friction factor	-
ΔP	Static pressure change	kPa
K	Loss coefficient	-
F	Cost multiplying factor	-
CEPCI	Chemical engineering plant cost index	-
ORC	Organic Rankine Cycle	-
VCC	Vapor Compression Cycle	-
ORVC	Organic Rankine-Vapor Compression Cycle	-

Greek and Latin

ε	Heat exchanger effectiveness	-
η	Efficiency	-
μ	Dynamic viscosity	kPa s
ν	Kinematic viscosity	m^2 s^{-1}

Subscripts and Superscripts

w	Water side
i	In
o	Out
r	Refrigerant side
h	Hot side
c	Cold side
s	Isentropic
ad	Adiabatic
min	Minimum
sc	Subcooled region
tp	Two-phase region
sh	Superheated region
cond	Condensing
l	Liquid
hyd	Hydraulic
c	Cross sectional
boil	Boiling
eq	Equivalent
VC	Vapor compression
gen	Generator
LHV	Lower heating value
MGO	Marine gas oil
PC	Power cycle
CC	Cooling cycle

CHAPTER 1. Introduction

1.1. Motivation for Waste Heat Recovery

The population on Earth is expected to grow from 7.4 billion to 9.5 billion in the next thirty years, which is going to increase the demand for energy, food, and other commodities [1]. As a result of population and economic growth, the global energy demand is expected to increase about 30%, from approximately 588 quadrillion British Thermal Units (quads) to 775 quads [2]. The increasing energy demand compels us to find new ways to improve the efficiency of energy conversion processes. In 2016, 80% of all energy was produced with nonrenewable resources including coal, petroleum, and natural gas [3]. The negative implications of using fossil fuels to produce energy are well-documented, including low thermal efficiency (~30%) and environmental impacts.

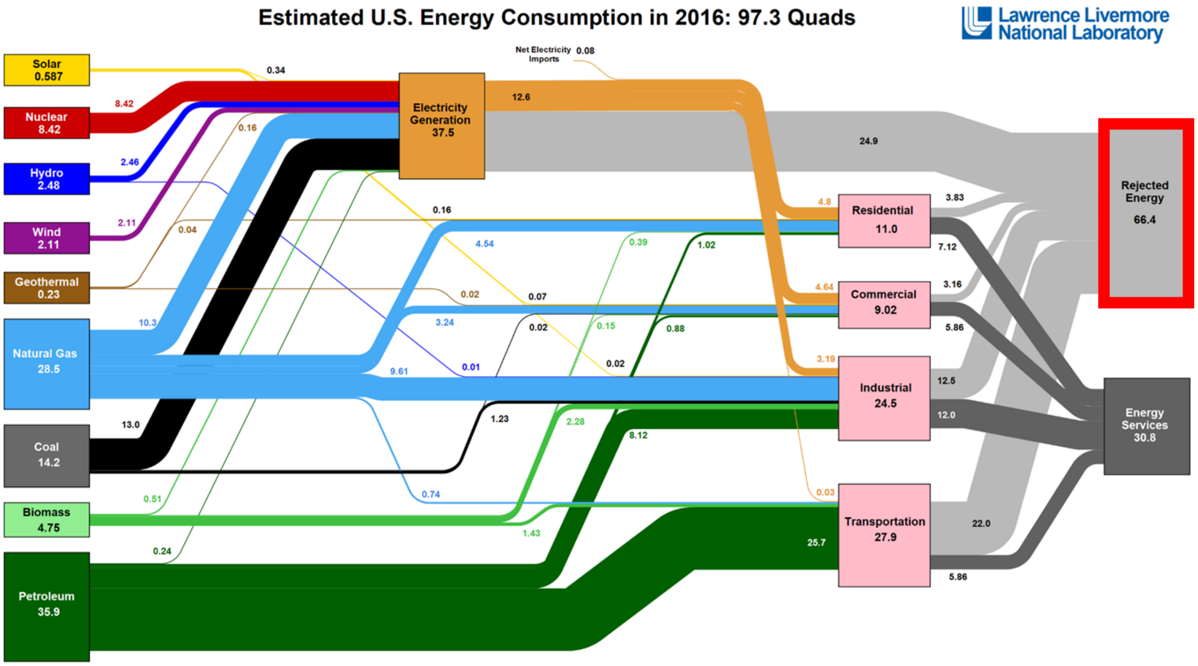

Figure 1-1: Energy flow diagram for United States energy consumption in 2016 [5].

Energy production with fossil fuels is highly inefficient due to thermodynamic limitations, about 2/3 of the energy input is rejected as waste heat [4]. In the United States, approximately 97 quads were consumed in 2016 to produce 31 quads of useful energy with 66 quads rejected as wasted energy. Figure 1-1 provides a breakdown of the processes and systems where the energy is consumed [5]. Waste energy is primarily released as heat, such as in cooling fluid for engines, hot exhaust gases from boilers, furnaces, and gas turbines, and heat losses through the walls of kilns and furnaces. Utilizing the wasted energy can improve the efficiency of these processes as evidenced by the inception of natural gas combined cycle (NGCC) power plants. NGCC power plants offer thermal efficiencies that are significantly higher than traditional coal fired power plants by using gas turbine exhaust to drive a bottoming steam Rankine cycle. In addition, many cement and metal processing plants have incorporated waste heat recovery devices to improve efficiency and decrease fuel consumption.

In addition to poor efficiency, using fossil fuels to produce energy has a significant impact on the environment. Releasing waste heat to the environment can cause imbalances in delicate ecosystems. Further, burning fossil fuels releases greenhouse gases (GHGs) which have contributed to warming of the Earth’s climate. Some of the more devastating climate impacts include rising ocean levels, melting Arctic and Antarctic sea ice, increasingly frequent extreme weather events, and extinctions of certain species of animals [6]. Improving the efficiency of power generating processes will reduce overall fuel consumption and help to reduce GHG emissions. There is also an economic benefit to improving the efficiency of power generating systems. In addition to the obvious cost savings from consuming less fuel, several nations have imposed a ‘carbon tax’. The carbon tax adds an additional cost to burning fossils and releasing harmful greenhouse gases into the atmosphere [7,8].

An effective way to improve the efficiency of fossil fuel systems is to utilize the two-thirds of the energy input that is typically wasted. This waste heat can be utilized in a waste heat recovery (WHR) system. Using this waste heat will increase system wide efficiency and thereby reduce fuel consumption. Consequently, it will diminish harmful greenhouse gas emissions and reduce operating costs through lower fuel expenditures and carbon taxes. The following sections will discuss types of waste heat and some common waste heat recovery systems. The primary types of waste heat recovery are internal heat recuperation or regeneration or the conversion of waste heat into useful mechanical work. The present work focuses on the conversion of waste heat into mechanical power.

1.2. Waste Heat Availability

The usefulness of waste heat energy depends on the quantity and quality of the waste heat source. The quantity of waste heat is the amount of energy contained in the stream in terms of mass flow rate and enthalpy. The quality of the waste heat is determined by the temperature of the stream. Waste heat sources are divided into three groups based on their temperatures (quality): less than 230ºC is considered low grade, 230ºC to 650ºC is medium grade, while above 650ºC is high grade waste heat [9]. An example of low grade waste heat is the cooling fluid from a diesel engine. Medium grade waste heat is in the exhaust streams of cement kilns and steam boilers. Many types of processing furnaces, including metals and glasses, exhaust streams of high grade waste heat [10]. Both aspects of waste heat—quality and quantity—influence how effectively the waste heat can be converted into useful mechanical work.

The exergy (or availability) of a waste heat source is defined as the maximum amount of work that can be extracted based on the heat input and the reservoir temperatures, as shown in Equation (1.1):

$$\dot{W}_{\text{max}} = \dot{Q}\left(1 - \frac{T_{\text{low}}}{T_{\text{high}}}\right) \tag{1.1}$$

The maximum amount of work is based on the heat input to system, $\dot{Q}$, and the temperatures of the hot and cold reservoirs in Kelvin. For example, a 90°C (363.15 K) low grade waste heat source transferring 2 MW of heat to a heat engine with a heat sink temperature of 32°C (305.15 K) will have a maximum work output of 319 kW. At the same conditions, a high grade waste heat source at 700°C (873.15 K) will have a maximum work output of 1373 kW. For a fixed heat sink temperature, the maximum amount of work that can be extracted will increase with heat source temperature. Thus, low grade waste heat is more difficult to effectively convert to work due to its low temperature. As the waste heat stream increases in temperature, a higher fraction of the input energy can be converted to work and in a more economically efficient manner.

Low grade waste heat is by far the most abundant of the three different types, but it also has the lowest availability, from Equation (1.1). It is estimated that there are 30 quads of waste heat available per year in the United States under 100ºC [11]. The low temperatures of these streams means the waste heat to power systems must have very large heat exchangers, very high mass flows, or high heat transfer coefficients because the thermal driving potential between streams is lower. These issues produce some problems for waste heat recovery of low grade streams because the heat exchangers are typically the most expensive piece of any waste heat recovery system. As the heat exchange area gets larger, the overall cost of the system will grow along with it. Advanced heat exchanger technology can increase the heat transfer coefficients, but come with a hefty price tag. This can lead to expensive systems with long payback periods, which is not ideal for implementation. The main goals of current studies are to increase the economic viability of low grade waste heat recovery systems using advanced cycles, advanced heat exchanger technology, and well-optimized working fluids.

Medium grade waste heat can be useful in several different applications including power generation, recuperation, reheats, and in cooling systems. Medium grade waste heat is not plagued by the same problems as low and high grade waste heat because the stream does not require extremely large heat exchangers or advanced materials to be used effectively. Unfortunately, medium grade waste is not as widely available as low or high grade waste heat.

High grade waste heat is of the highest quality and contributes a significant quantity of total waste heat, making it ideal to utilize. Streams of high grade waste heat can be used to vastly improve efficiencies in industrial processes through recuperation of heat energy within cycles and utilization of the heat in external cycles. Despite this, the challenges of high grade waste heat are numerous. There are challenges with material compatibility and the requirement of secondary heat exchangers. The high temperatures (and often highly oxidizing streams) present an environment that requires advanced heat transfer materials, which can not only be extremely expensive, but also difficult to design and manufacture. There is a significant body of work dedicated to studying high temperature alloy heat exchangers and ceramic heat exchangers for use in high temperature applications [12–14]. In addition, high grade waste heat often exceeds the decomposition/critical temperature of the most common working fluids used in waste heat recovery systems [15,16]. To combat this, a system utilizing high grade waste heat requires an intermediate heat exchanger where the high grade waste heat stream transfers heat to a thermal oil. Then, the thermal oil will exchange heat to the working fluid in another heat exchanger. This intermediate heat exchanger will increase the system cost and reduce the thermal efficiency of the system, which can be a barrier to implementation.

1.3. Waste Heat Recovery Systems and Applications

There are a number of different waste heat recovery systems. Some waste heat recovery systems transfer wasted heat to another location in the facility where heat is required. An example of this internal heat recovery is using waste heat from the outlet of a cement furnace to preheat the air entering a cement kiln. In addition, some waste heat recovery systems utilize waste heat in an external process to generate some useful output. The most common useful output is electric power, which can be produced from waste heat in a few different cycles. The most common waste heat to power system is the Rankine cycle, where waste heat boils a working fluid and then the fluid is expanded in a turbine to produce mechanical power. The Rankine cycle can operate with a number of working fluids (organic refrigerants, steam, or supercritical CO_2) depending on waste heat quality. The organic Rankine cycle typically has a heat to electric power efficiency between 15 and 20% [17–21].

Another type of waste heat recovery system uses the wasted heat energy to produce cooling, which is called a thermally activated cooling system. There are four primary types of heat activated cooling systems: absorption, adsorption, ejector, and organic Rankine-vapor compression. However, only absorption systems are commercially available. The adsorption system has a number of operational challenges including: low coefficient of performance (0.35), batchwise cooling, and very low gravimetric cooling density [22,23,32–37,24–31]. The challenges associated with the ejector cycle include low coefficient of performance (0.2 – 0.4) and inefficient ejector nozzles [38,39,48–51,40–47]. The literature review will focus solely on the absorption system and the organic Rankine-vapor compression cycle.

There are a number of applications where waste heat to cooling systems are attractive, including manufacturing plants (metals, cements), chemical processing plants, food processing plants (meats, brewing, dairy), and the transportation sector (marine or on-road). The primary considerations for waste heat to cooling applications are the presence of waste heat stream and the need for co-located cooling. The drivers for implementation are the reduction of expenditures to provide cooling, reducing greenhouse gas emissions, and improving energy efficiency. The present investigation focuses on the recovery of waste heat from marine vessels to provide useful shipboard cooling.

As of 2013, the International Maritime Organization (IMO) has enacted more stringent regulations regarding the emissions of marine vessels. Large marine ships emit CO_2, NO_X, SO_X, and particulate matter (PM), which are harmful in a number of ways to the environment. The two key parts of the legally binding IMO regulations are the Energy Efficiency Design Index (EEDI) and the Ship Energy Efficiency Management Plan (SEEMP). The EEDI is a measure of the amount of CO_2 released per capacity mile of the ship, where a lower EEDI represents a more efficient ship. The EEDI regulation imposes a maximum value for newly constructed ships in different classes based on capacity and type. Every 5 years, the maximum EEDI will decrease to push maritime technology toward energy efficiency. The SEEMP is a methodology developed by the IMO to help pre-existing marine vessels improve fuel economy through optimization of operational parameters (speed, voyage path, and electric use) and through implementation of new technology. The IMO encourages waste heat recovery installations on new and pre-existing ships to improve efficiencies, reduce emissions, and reduce fuel consumption [52].

The present work focuses on a waste heat recovery system applied to a large marine diesel engine to improve fuel economy and reduce greenhouse gas emissions by replacing traditional electrically driven cooling systems. The two main streams of waste heat are the exhaust gas and the engine coolant. The exhaust gas is typically high or medium grade waste heat with several contaminants, including SO_X and NO_X. The presence of these contaminants will cause corrosion and fouling which degrades the performance of the heat exchangers [53,54]. The engine backpressure from exhaust gas scrubbers and heat exchangers can lower engine efficiency and hamper performance. In addition, the high temperature exhaust stream could exceed the critical temperature or decomposition temperature of the WHR system working fluid, which can have dangerous consequences for system operation. The other waste heat stream, engine coolant, is much lower temperature (~90°C) and is in the liquid phase. The low temperature of this stream does not exceed the working fluid decomposition temperature or critical point, but it makes efficient waste heat recovery to power more difficult, due to the availability. However, the liquid phase of this stream has more favorable properties for heat transfer than the exhaust gas, namely higher thermal conductivity, density, and specific heat. The favorable heat transfer properties contribute to a more cost effective system with a smaller footprint. In addition, introducing extra pressure drop on this line does not have a negative impact on engine performance. Thus, engine coolant is an ideal waste heat stream for an ultra-efficient waste heat recovery technology.

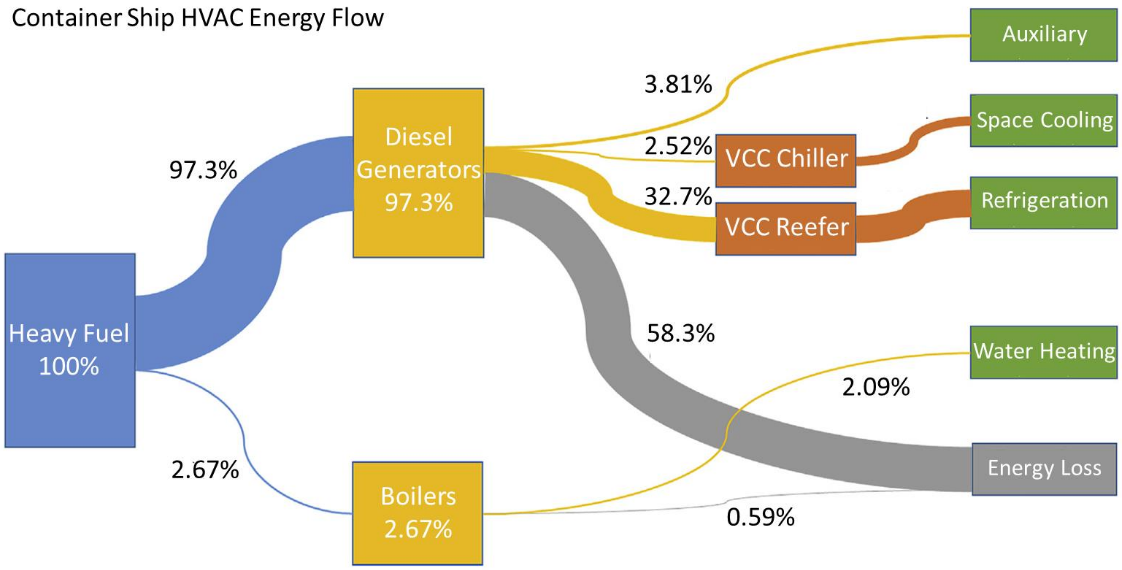

Figure 1-2: Sankey Energy flow diagram for the HVAC systems on a container ship [55].

In this work, the technoeconomic viability of implementing an advanced waste heat recovery system designed to provide useful cooling on a large marine vessel will be studied. Typical marine vessels have two groups of diesel generators onboard: one of the groups provides propulsion for the ship, while the other group produces electricity for cooling and auxiliary electronics. A Sankey diagram of the energy flows in the HVAC system for a container ship is provided in Figure 1-2 [55]. As shown, refrigeration and air conditioning is provided onboard marine vessels by electrically driven vapor compression systems, which accounts for about 1/3 of the electricity generated by the second group of diesel generators. About 59% of the original input energy is rejected as waste energy, existing primarily as heat in the exhaust gas and engine coolant. Utilizing waste heat to provide refrigeration or air conditioning will reduce the amount of fuel consumed, thereby reducing annual fuel expenditures and greenhouse gas emissions. Theoretically, the waste heat could be converted to cooling using any of the heat activated cooling systems briefly mentioned above. In practice, the only viable technology currently available in the marine market space is the absorption system. Although the technology is mature, the absorption system is not currently used onboard marine diesel ships to provide cooling from waste heat because it has a large footprint, reliability issues, and significant operational challenges. The system examined in this study is an advanced design of organic Rankine-vapor compression refrigeration system that overcomes many of the challenges associated with absorption refrigeration while achieving similar performance metrics. The details of the system will be provided in the literature review.

1.4. Research Objectives

The goal of this work was to simulate a new type of thermally driven cooling system implemented on a large marine diesel engine. The system is ideally suited to be integrated into a marine vessel because it is a combination of well-known and understood technologies and does not have the same operational inefficiencies and challenges as other heat activated cooling systems. The present work simulated a turbo-compression cooling system that was driven by 90°C engine coolant, rejected heat to 32°C seawater, and provided cooling to a water stream from 12°C to 7°C. Detailed plate and frame heat exchanger models were integrated into the thermodynamic modeling block of code to accurately calculate heat transfer coefficients, pressure drops, and size of the heat exchangers. Finally, an economic model that accounted for the cost of the major pieces of equipment was coupled to the thermodynamic and heat exchanger model to better understand how technical performance is related to economic performance. The whole system code was optimized to minimize the payback period by varying the heat exchanger sizes. Five different working fluids were examined in this study to quantify the effects of fluid properties on technoeconomic performance.

1.5. Thesis Organization

The following chapters detail a technoeconomic study of a turbo-compression cooling system driven by waste heat to provide chilling for large marine vessels. Chapter 2 of the document will provide a literature review of the available studies on thermally activated cooling systems regarding their performance and economics. The literature review will go into specific detail about absorption, adsorption, ejector, and organic Rankine-vapor compression cycles. Chapter 3 will thoroughly examine the modeling approach of this work and provide a representative calculation for the payback period of the system with R134a as the working fluid. Chapter 4 will present the results of the optimization routine to minimize payback period of the turbo-compression cooling system using five different working fluids. The final chapter will provide closing remarks and offer recommendations for future work.

CHAPTER 2. Literature Review

The present study will focus on the recovery of energy from low grade waste heat streams to produce useful cooling in a thermally activated cooling system. Thermally activated cooling systems use heat energy to produce a useful cooling effect. There are four main types of thermally activated cooling systems: absorption, adsorption, ejector, and organic Rankine-vapor compression cycles. Each of these systems has its own working principles, which will be briefly described. In addition, some characteristics of each system will be provided. After the overview, a survey of the available literature will be provided to give context to the current study.

All of the heat activated cooling systems have a few components in common: evaporators, condensers, and heat exchangers that transfer heat to the working fluid from the external stream of heat. The external stream is defined as the fluid that is not strictly contained in the cooling system. The cooling effect is generated in the evaporator, where the working fluid boils to draw heat from the external steam. Heat is rejected to some external stream, air or water, in the condensers. The primary performance metric to compare systems in the following literature review will be the coefficient of performance (COP), which is a ratio of the cooling duty to the input heat. The COP is defined in Equation (2.1):

$$\mathrm{COP} = \frac{Q_{\mathrm{chill}}}{Q_{\mathrm{heat}}} \tag{2.1}$$

where Q_{chill} is the amount of cooling provided by the system and Q_{heat} is the amount of heat input to the system. The operating conditions of heat activated cooling systems have a significant impact on the refrigeration COP. In general, COP improvements can be realized by decreasing the heat sink temperature and increasing the evaporator temperature. In some cases, increasing the heat source temperature can improve the COP.

The primary technoeconomic metrics used in this work are the payback period and the specific cost. When using waste heat to provide cooling, the payback period can be quantified in terms of energy savings, as shown in Equation (2.2):

$$\text{Payback Period} = \frac{\text{System Cost}}{\text{Energy Savings}} \tag{2.2}$$

In the case of shipboard cooling, heat activated cooling systems reduce the amount of fuel consumed by producing cooling from waste heat, instead of electricity. The payback period is strongly dependent on the cost of energy (fuel, electricity, etc.) and the total system cost. In places where electricity or fuel is expensive, thermally activated cooling systems can be an attractive option for reducing energy consumption. Different thermally activated cooling systems can be compared by examining their specific cost. The specific cost is defined in Equation (2.3):

$$\text{Specific Cost} = \frac{\text{System Cost}}{Q_{\text{chill}}} \tag{2.3}$$

A high specific cost implies that each unit of cooling is more expensive for that system.

In the sections below, a review is provided on the relevant literature on technical and economic studies for two major thermally activated cooling systems: absorption and organic Rankine vapor-compression. After the review of the literature, the primary gaps in the research will be identified to provide better context for the present work. Informed by the gaps in the literature, the specific aims of this study will be presented.

2.1. Absorption Refrigeration Technology

A process flow diagram of the absorption system is provided in Figure 2-1 [56]. In the absorption refrigeration system, a volatile liquid, serving as the working fluid, evaporates and provides the desired cooling (points 9 to 10). After the working fluid is in the gas phase, it is absorbed by another liquid (the absorbent), which must be less volatile, in the absorbing heat

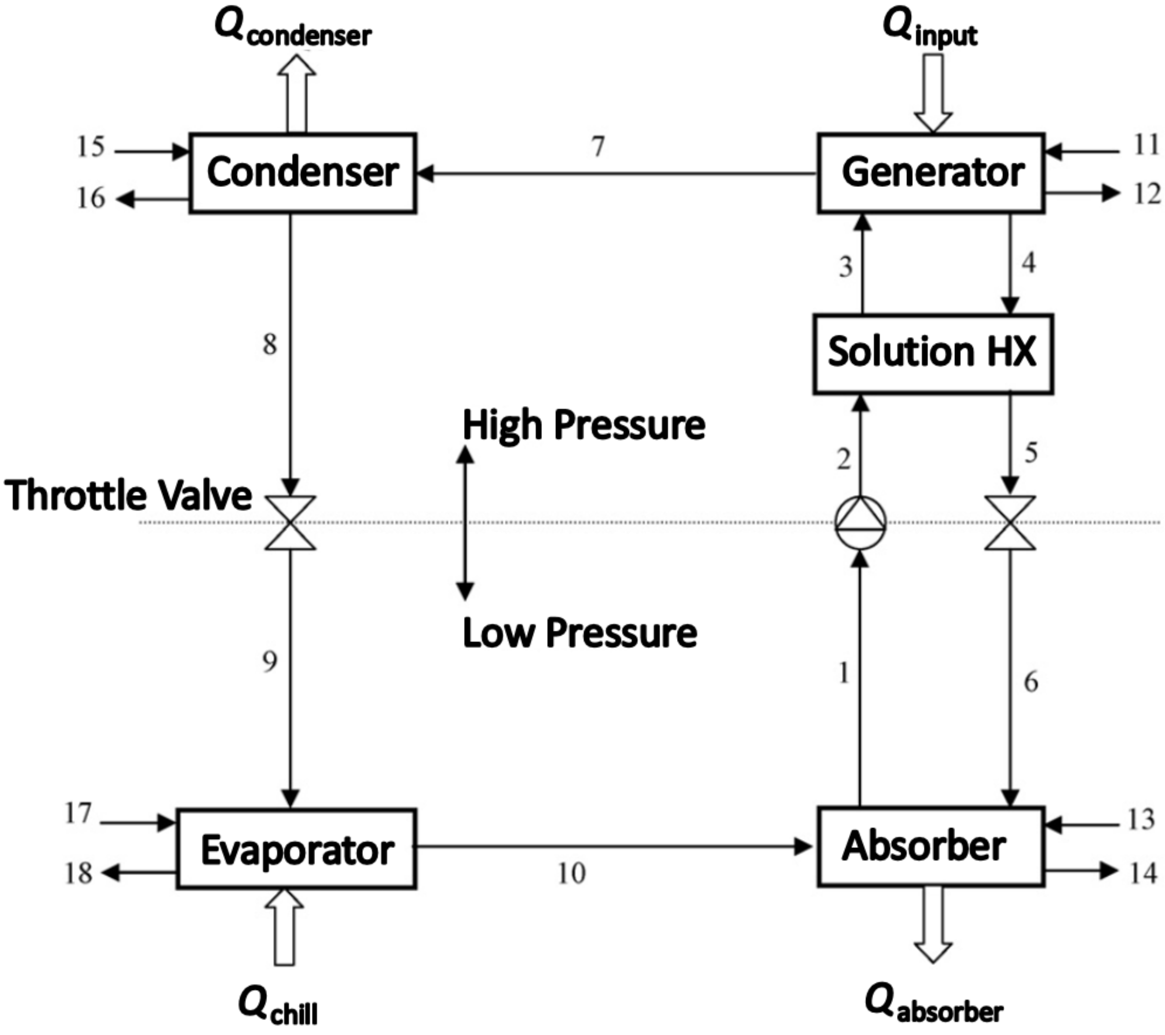

Figure 2-1: Process flow diagram of a single-effect LiBr-water absorption refrigeration system [56].

exchanger (10 to 1). Then, the mixture is pumped to a higher pressure (1 to 2) and exchanges heat with the strong absorbent solution in the solution heat exchanger (2 to 3). The high pressure mixture of working fluid and absorbent is heated from the available heat source to evaporate the working fluid, separating the working fluid and absorbent (3 to 7). The strong absorbent solution leaves the generator and passes through the solution heat exchanger on its way back to the absorber (4 to 5). After leaving the generator, the high temperature and pressure gas phase working fluid passes through a condenser to bring it back to the liquid phase (7 to 8). Then, the liquid working fluid is throttled in an expansion valve to greatly reduce its temperature and pressure (8 to 9). After this, it can evaporate again and provide the desired cooling effect to complete the cycle. Similar to vapor compression refrigeration systems, the condensation process takes place on the high pressure side of the process. The most common working fluid pairs for absorption systems are LiBr-water and Ammonia-water. In the first type, water is the working fluid and gets absorbed by a LiBr solution. The second type uses ammonia as the working fluid, which gets absorbed into water. Figure 2-2 shows an image, from Thermax, of a steam driven LiBr-water absorption unit [57].

Single effect LiBr-water absorption systems driven by low grade waste heat can have a relatively high Coefficient of Performance (COP) compared to other thermally activated cooling systems, up to 0.6 [58–65]. The COP of the absorption refrigerator depends greatly on the operating conditions and ambient conditions. One of the drawbacks for a LiBr-water absorption refrigerator is a phenomenon called crystallization where a high heat sink temperature can cause the salt to precipitate out of solution [66,67]. Crystallization can completely stop the performance

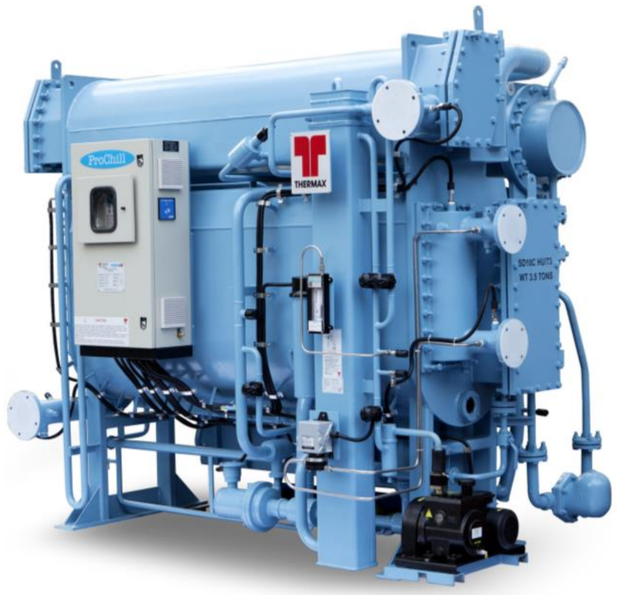

Figure 2-2: Steam-driven Thermax ProChill LiBr-H_2O absorption chiller [57].

of the machine making it unable to provide the desired cooling for hours or even up to days. The system must be heated and cooled down cyclically while maintaining the proper chemical balance to break up and eventually dissolve the crystallized salts in the heat exchangers. Further, these systems must operate at sub atmospheric pressures to facilitate the boiling and condensing of water, which can present operational challenges. On the other hand, ammonia-water absorption systems can provide chilling at temperatures down to -55°C because the freezing point of ammonia is much lower than water [63]. These systems operate at standard pressures, but contain a significant amount of ammonia which is a highly toxic fluid.

The relevant literature regarding thermodynamic performance characteristics of the absorption chiller will be described first followed by technoeconomic studies performed on the

Table 2-1: Summary of technology studies for absorption refrigeration.

Authors	**Working Fluid Pair**	**Generator Temp.**	**Condenser Temp.**	**Chiller Temp.**	**COP**	**Cooling Duty**
-	**-**	**°C**	**°C**	**°C**	**-**	**kW**
Al-Tahaineh et. al. ^{e} [58]	LiBr-Water	90†	-	5†	0.79	10
Cao et. al. [74]	LiBr-Water	280	35	6.7	0.64	4300
De Vega et. al.^{e} [68]	LiBr-Water	100	30	5†	0.72	7.5
Ge et. al.^{e} [63]	NH_3-Water	-	35	-5	0.45	12.5
Keinath et. al.^{e} [71]	NH_3-Water	173.2	35	12.8	0.695	2.2
Le Lostec et. al. [64,69]	NH_3-Water	85	22	19	0.5	9
Longo et. al. [72]	LiBr-Water	80 150	32	7	0.88‡	1050
Manzela et. al.^{e} [70]	NH_3-Water	-	27	5	0.013	0.0185
Palomba et. al. [73]	NH_3-Water	215	25	5	0.55	15

Note: The external stream temperatures are provided unless otherwise designated.
All studies with experimental component are labeled with ^{e}.

† Saturation temperature

‡ COP of a combined single and double effect absorption system

absorption refrigeration system. A summary of the operating conditions for each of the technology studies is provided in Table 2-1.

2.1.1. Review of technology research

There are a number of research examinations and case studies that describe the thermodynamic performance of absorption chillers. The two most common absorption chillers use lithium bromide-water or ammonia-water as working fluid pairs. The important results from the studies will be summarized and trends across the studies will be identified.

Al-Tahaineh et. al. performed an exergetic analysis on a small scale (1 kW and 10 kW) single effect LiBr-water absorption refrigeration system [58]. The effects of generator temperature on the energetic and exergetic performance were examined. For the 10 kW system, a maximum COP of 0.79 at generator temperature of 90°C and an evaporator temperature of 5°C was found. Regarding exergetic performance, the amount of exergy destroyed increased with higher generator temperatures with the greatest exergy destruction occurring in the generator and the evaporator. Optimizing the design of these heat exchangers is essential to minimize exergy loss, which would improve the performance of the refrigeration system. The study does not offer any specific details on how to improve exergetic performance of the heat exchangers. However, this will be a common finding throughout this literature review: the design of the heat exchangers is the most important factor in overall system performance and system cost.

Another study investigated strictly thermodynamic performance of the absorption chiller was performed by Ge et. al. [63].The work modeled and experimentally validated performance for a gas fired ammonia-water absorption chiller operating over a range of conditions, including heat source input, chilled water temperature, and ambient temperature. The gas fired absorption unit used to validate the mathematical model had a 12 kW capacity at 35°C ambient air temperature for a chilled water temperature of -5°C. The temperature of the ammonia-water solution at the outlet of the generator was 120°C in all cases. There was good agreement between the simulation results and experimental data for high and low side pressures, cooling capacity, and COP. The performance of the absorption chiller was simulated over a range of ambient air temperatures, chilled water temperatures, and heat inputs. Increasing the heat input decreased the COP of the absorption unit because the refrigerant mass flow rate increases, while the concentration of refrigerant is reduced in both the strong and weak solutions. The reduction in concentration drives the temperature of the chilled stream down and thus reduces the COP. If the chilled water stream was kept at a constant temperature, it seems likely that the COP would be either unchanged or increased. As a trend, increasing the chilled water temperature and decreasing the ambient air condenser temperature improved the performance (COP and cooling capacity) of the absorption chiller simulations. This trend is the norm for all heat activated cooling systems: the performance is heavily dependent on the operating conditions.

De Vega et. al. took the previous analyses one step further by incorporating heat exchanger models into the thermodynamic study [68]. The work modeled and experimentally examined the performance of a single effect LiBr-water absorption with plate heat exchangers and heat source temperature ranging from 75°C to 115°C. A thermodynamic model of the system was integrated with plate heat exchanger models for the generator, condenser, and the heat recovery unit. The plate heat exchangers used in the study were commercially available with grooved and corrugated surfaces and a 60 degree chevron angle with a plate spacing of 3.0 mm. The evaporator temperature had a more pronounced effect on the COP compared to the heat source temperature. At a heat source temperature of 100°C, evaporator temperature of 5°C, and condensing water temperature of 30°C, a COP of 0.72 was experimentally determined. Correlations were used from the literature to calculate single phase and two-phase heat transfer coefficients in the plate heat exchangers and were validated from experimental data. At increasing heat source temperatures, there was higher wall superheat and increased bubble generation in the generator, which improved heat transfer performance. The pressure drop through the heat exchangers was not modeled. This study is important because it integrates a compact heat exchanger model with the thermodynamic performance model.

Another study that integrated heat exchanger models with thermodynamic performance was performed by Le Lostec et. al. [64,69] The thermodynamic and heat transfer performance of a single effect ammonia-water absorption refrigeration system was simulated and validated against a commercially available absorption chiller. Mass transfer effects in the absorber were taken into consideration, as well as the condensation heat transfer of binary vapor in the condenser. Off-design performance was characterized. The absorption unit used shell and tube heat exchangers for the evaporator and absorber and plate heat exchangers for the generator, condenser, and solution heat exchanger. Similar to Ge et. al., this study found that the COP and cooling capacity improves by increasing the chilling circuit temperature. In addition, increasing the heat source temperature from 60°C to 95°C increased the cooling capacity from 7.5 kW to 12.5 kW, but decreased the COP from 0.65 to 0.58. The COP declines at high temperature heat sources because more exergy is destroyed due to excessive superheat of the vapor leaving the desorber. The COP of this absorption system was high for such a low generator temperature because the temperature of the chilled water stream was 19°C while the heat sink temperature was 22°C. The combination of high chilling water temperature and low heat sink temperature will improve the COP of the system. The flow of refrigerant into the evaporator of the absorption chiller is not regulated by the cooling load. When the cooling load of the absorption chiller was lower than the design point, too much refrigerant is sent to the evaporator and the performance will be degraded. The control of refrigerant for the absorption chiller should be influenced by the cooling load to maximize performance.

The above is a brief review of thermodynamic performance studies of absorption refrigerators. As this work is focused on waste heat recovery, the literature review will transition to typical studies featuring absorption refrigeration systems driven by waste heat from primary movers: internal combustion engines and gas turbines. Two studies examining absorption systems implemented on marine vessels will be reviewed to provide some context to the present work on marine diesel waste heat recovery.

Manzela et. al. experimentally examined an ammonia-water absorption refrigeration system driven by the exhaust gas of an internal combustion engine [70]. The commercially available refrigeration system was integrated directly onto the exhaust manifold of the engine and the absorption chiller was designed to cool an internal volume of air. The power output of the engine, temperature of the exhaust gas, and flow rate of the exhaust gas were not provided. At max throttle, they found the steady state cooling capacity of the absorption refrigerator was about 18.5 W with a COP of 0.013. The temperature of the chilled air was kept constant at 5°C. The COP in this study was over 40 times lower than what others have found. An absorption unit specifically designed for exhaust heat recovery would have an improved performance compared to an off-the-shelf device. No further justification was provided for the extremely low COP of the absorption unit. The performance of the absorption unit was also strongly dependent on the engine loading condition. When the engine was operating at over 2000 RPM, the heat input to the absorption chiller was too great and the temperature of the internal volume of air increased. This represents an important design consideration that must not be overlooked: the transient nature of waste heat sources can have an impact on the performance of the heat activated cooling system, as evidenced by the work from Manzela et. al. and Le Lostec et. al.

Another work that simulated the performance of an ammonia-water absorption chiller driven by the exhaust of an internal combustion engine was completed by Keinath et. al. [71]. The study simulated a single effect ammonia-water absorption heat pump system driven by diesel engine exhaust waste heat. This system could provide heating or cooling depending on its operational mode. The system was driven by thermal oil that entered the absorber at 173°C. The thermal oil was heated in an intermediate heat exchanger from diesel engine exhaust gas at 398°C. The chilled water temperature was 12.8°C and the ambient air temperature was 35°C. During the cooling mode, the COP was 0.70 and provided 2.1 kW of cooling. The COP and cooling load decrease with increasing ambient air temperature. Although, heat exchanger *UA* was included as a preliminary sizing parameter to better understand capital cost and system footprint, no indication heat exchangers design was given. Unfortunately, the results of the *UA* study were not included. It would be interesting to quantify the impact of increasing heat exchanger *UA* on the thermodynamic performance and system cost. While the authors included *UA* calculations, the economic viability of this system is still unknown because no economic modeling was performed.

Building from the previous works, Longo et. al. simulated a LiBr-water absorption refrigeration system that utilizes waste heat in two different forms from a 1 MW Otto Cycle engine [72]. In this analysis, the internal combustion engine had 600 kW of low grade heat available in the engine coolant which was used to drive a single effect absorption chiller. In addition, there was 585 kW of high grade waste heat available in the exhaust of the engine that drove a double effect LiBr-water absorption system. The mechanical power of the Otto Cycle engine was used to drive a traditional vapor compression refrigeration cycle. The study modeled each heat exchanger in the system. At nominal operating conditions for commercial air conditioning systems, the combined COP of the absorption chillers was approximately 0.88. Nominal operating conditions are 32°C condensing temperature and 7°C chilled water outlet temperature. The primary energy ratio (PER), defined as the ratio of total refrigeration capacity to total thermal energy input to the engine, increased from 1.2 to 1.6 after implementation of the waste heat recovery system. The absorption chillers provided 1.05 MW of cooling while the vapor compression unit provided 3.1 MW of cooling. The absorption system could only operate with cooling water inlet temperature lower than 35°C and chilled water outlet temperature higher than 3°C because the working fluid is water in a LiBr-water system.

Regarding absorption chillers used for marine waste heat recovery, Palomba et. al. simulated a waste heat driven ammonia-water absorption refrigeration system for use onboard a fishing vessel to generate cooling [73]. 75% of the electricity production on small fishing vessels is used for refrigeration purposes, according to a number of case studies reviewed by Palomba. To reduce electricity consumption, an exhaust gas driven absorption system was implemented. The exhaust gas heated a thermal oil in an intermediate heat exchanger and the hot thermal oil drove the absorption system. When the system operated with 215°C oil and a cooling water temperature of 25°C, the COP was 0.55 and the cooling capacity was approximately 15 kW. Although the absorption system only utilized about 4% of the waste heat available in the exhaust gas, energy consumption was reduced by 4.7 MWh per a year, fuel consumption by 1212 kg per year, and CO_2 emission by 3.15 tons per year. The absorption system provided significant savings, but the cost of the system is an unknown and must be examined further to demonstrate viability in this application. From this work, it is obvious that the implementation of absorption chillers can significantly reduce energy consumption and emissions onboard marine vessels.

Cao et. al. is another example study of absorption chiller integrated onto a marine vessel. This work quantified the fuel economy improvements by implementing a waste heat driven LiBr-water absorption system for shipboard cooling on a large cargo ship in three different locations: Baltimore, Miami, and Abu Dhabi [74]. A transient model of an absorption system was developed where the waste heat was recovered from a marine diesel engine. The study assumed that the absorption system could completely replace the electrically driven vapor compression chillers onboard. The absorption system was driven by hot water produced from the engine exhaust gas and cooled using seawater. The cooling system supplied chilled water at 6.7°C. The exhaust gas temperature was a function of the engine power ratio and ranged from 240°C to 280°C as the power ratio increased. The condenser cooling water temperature ranged from 22°C to 35°C based on operating location. As the heat sink temperature increases, the concentration of the strong solution will increase and eventually lead to crystallization. The model ensured crystallization never occurred by varying the flow rate of the solution. The absorption system had a higher COP (0.64 vs. 0.61) in Baltimore than in Abu Dhabi, presumably due to cooler heat sink temperature. The absorption system reduced fuel consumption by 68% in Abu Dhabi, 62% in Miami, and 38% in Baltimore. The largest fuel consumption reduction was realized in Abu Dhabi because the cooling needs are the most extreme of the three cases. The study should be extended to understand the economic impact of implementation – i.e., how much money does a 68% reduction in fuel consumption save the operators and how long would it take to pay back the absorption system? In addition, the cooling requirements for a cargo ship are miniscule compared to the cooling needs on a luxury cruise ship. Cooling systems onboard cargo ships represent about 0.11% of the total fuel consumption, while cooling systems for cruise ships represents about 13.3% of the total fuel consumption [74]. Waste heat driven cooling systems are an attractive option for reducing fuel consumption and greenhouse gas emissions for marine vessels, especially luxury cruise lines. There is a significant quantity of waste heat and cooling needs which is an ideal scenario for a thermally activated cooling system. This study demonstrates the economic benefits for waste heat to cooling technology onboard marine vessels.

The most important trends from the above technical studies on the absorption refrigerator are summarized here: energetic performance will improve when the condenser temperature is decreased or when the evaporator temperature is increased, the typical COP of the single effect absorption refrigerator lies in the range of 0.5 to 0.7 (at a generator temperature around 90°C), and increasing the heat source temperature will increase the cooling capacity but lower the COP because there are more exergetic losses when the temperatures between the heat source and working fluid are farther apart. A summary of the above studies is provided in Table 2-1. Marine vessels are an application where heat activated cooling systems are particularly attractive because fuel is expensive, the amount of waste heat is significant, and the cooling needs are large. The two studies on marine vessels demonstrated that significant savings could be realized by recovering waste heat to provide cooling.

2.1.2. Review of technoeconomic research

Experimental and simulated performance studies on the absorption chiller are abundant in the literature, but technoeconomic analyses are somewhat limited. The most common type of analysis is an exergy based optimization where the goal is to minimize the amount of exergy destroyed through the cycle. These analyses highlight where the largest amount of exergy destruction occurs in system components. In some cases, a monetary value is assigned to the exergy flow to quantify the ‘cost’ of exergetic inefficiency.

Bereche et. al. performed a thermoeconomic analysis of a 316 kW LiBr-water absorption chiller chosen to provide cooling for a university hospital in Brazil [75]. For a single effect system, they examined two cases: direct fired or hot water driven with cogeneration. The highest exergetic losses occurred in the evaporating heat exchanger and the throttling valve because both components have high irreversibility, again showing the design of the heat exchangers are critically important to system performance. Direct fired or hot water driven with cogeneration single effect absorption chillers would be suitable for implementation with waste heat sources between 80°C and 120°C. A comparison between costs of a traditional vapor compression system and the absorption system would be useful to help the hospital understand how the economics of these two systems compare.

Misra et. al. examined the thermoeconomic performance of a single effect LiBr-water absorption system using the structural optimization method [76]. The single effect absorption chiller was driven by 100°C steam and chilled a water stream from 20°C to 12°C. The condenser cooling water inlet temperature was 30.4°C. The optimization routine sought to minimize the operating cost per year by varying the heat exchanger surface area. To minimize the operating cost per year, the exergy destruction was minimized, which decreased the total irreversibility in the system and increased efficiency, thus requiring less fuel to produce the same amount of cooling. Total exergy destruction could be reduced by 47% if the total area of the heat exchangers was 1.55 times larger. Larger heat exchangers increased the initial investment of the optimized design by 33% but the extra cost incurred would be paid back in 4 years. The total system capital cost of the optimized design was $60,731 with a cooling capacity of 201 kW, which is approximately $301 per kWth. This study shows that heat exchangers are the most important component to design in a heat activated cooling system because they are often the most expensive components. Optimizing the heat exchanger design can have a huge impact on the total cost of the system without sacrificing performance.

Misra et. al. extended their previous study to a single effect ammonia-water absorption system [77]. The absorption system uses 170°C steam to chill water from 20°C to 10°C and rejects heat to 27°C cooling water with a total cooling capacity of 100 kW. The goal of this study was to minimize the cost of the product (chilled water) by optimizing the generator temperature, the isentropic efficiency of the pump, and the effectiveness of the refrigerant and solution heat exchangers. The cost of the seven heat exchangers in this system was calculated based on heat exchanger area. The pump and motor cost was included in the analysis. The chilled water cost was minimized by: increasing the generator temperature from 150°C to 155°C, decreasing the isentropic efficiency of the pump from 0.75 to 0.70, increasing the effectiveness of the refrigerant heat exchanger from 0.60 to 0.825, and increasing the effectiveness of the solution heat exchanger from 0.60 to 0.90. Decreasing the isentropic efficiency of the pump seems counterintuitive, but the cost of the pump is directly related to the efficiency, where a decrease in efficiency will cause a decrease in cost. The exergetic efficiency of the system was increased by 44.6%, the COP was increased by 44.2%, and the cost of the chilled water was decreased by 10.3%. After optimization, the total investment cost of the absorption system remained the same, approximately $240,000 which yields a cost of $2400 per kW_{th}. This study found an extremely high specific cost for the system, where most absorption systems lie below $400 per kW_{th} [78]. It is unclear why the cost of this system was so much greater than others.

Another work that sought to improve the exergetic efficiency of the absorption system was performed by Kizilkan et. al. [56]. A thermoeconomic optimization of a 20 kW single effect LiBr-water absorption system was performed. The operating temperature of each heat exchanger was varied to minimize the capital cost. In this work, the heat transfer coefficient of each heat exchanger was assumed to be 500 W m^{-2} K^{-1}. A simple cost model was applied to each heat exchanger to calculate the total cost of the system. The total system cost was $24,526, with the evaporator and condenser being the largest heat exchangers (37.1 m^2 and 7.2 m^2, respectively). Minimizing irreversibility does not necessarily lead to the minimum system cost because highly efficient heat exchangers are more expensive. This is a subtle, but critically important point: having a high COP does not necessarily mean the system is the best choice for an end user. The economics must be studied in conjunction with technical performance. The cost of the system was $1226 per kW_{th}. The study could be improved by using realistic heat exchanger models. Abbaspour et. al. did a very similar study to Kizilkan, but instead used a genetic algorithm to optimize the single effect LiBr-water system and found similar results [79]. The COP increased from 0.451 to 0.787 after the optimization routine with similar trends as mentioned above (increased generator and evaporator temperatures, decreased condensing temperatures). Abbaspour et. al. didn’t include component cost models to understand how the capital cost of their system is increased by the increased thermodynamic efficiency. Again, it was demonstrated the heat exchanger design is the most important factor in technoeconomic performance because they are the most expensive components.

Boer et. al. performed a similar study to the work from Misra et. al., where the goal was to understand the exergy flows in a single effect ammonia-water absorption refrigeration [80]. A 1 MW chiller was analyzed with the following assumptions: chilled water temperature drop from 12°C to 6°C, a condenser temperature lift from 27°C to 32°C, hot water inlet temperature of 90°C, and the minimum temperature difference in the heat exchangers was 5°C. A COP of 0.67 was found with these conditions as a base case, with the largest exergy destruction occurring in the absorber. Then, a structural analysis was performed to understand how reducing irreversibility in a certain component affects overall cycle performance. Increasing the *UA* of the absorber resulted in a coefficient of structural bond (CSB) of 3.29 for the absorber. The CSB represents the system wide improvements in efficiency from improving a single component efficiency, due to interaction between components. A CSB of 3.29 means that reducing the exergy destruction in the absorber by 1 kW will reduce total system exergy destruction by 3.29 kW. Small improvements of the absorbing heat exchanger can significantly improve system performance – again showing heat exchangers are the critical piece of the design work. The study did not provide any insight into physical component cost or payback period.

Two works will be provided below that provide more insight into physical component cost and payback periods of the absorption chiller. The first, from Lu et. al., performed a technoeconomic case study on a waste heat driven single effect absorption chiller with LiBr-water as the working fluid pair [81]. The absorption chiller was driven by 200°C waste heat from the exhaust stack of an unnamed industrial process, where 200 kW of heat was available. To calculate the payback period, the authors compared the cost of providing an equivalent amount of cooling with a vapor compression system where electricity was $0.12 per kWh. The authors gathered quotes from commercially available absorption refrigeration systems to estimate the initial capital cost of their system based on 200 kW of heat recovery. The system could provide about 165 kW of cooling, which yields a cost of approximately \$354 per kW_{th}. The COP of the absorption system was 0.825 which could save up to $23,000 per year with a payback period of approximately 2.54 years. This study is interesting because it provides a direct comparison between the economic performance of a traditional electrically driven chiller and a heat driven chiller. In facilities where there is waste heat and a need for cooling, a heat activated cooling system can be economically feasible. The key driver here is having ‘free’ energy. The economics of a direct fired absorption unit are not nearly as favorable because of the low COP (~0.6) compared to an electrically driven vapor compression chiller (COP ~ 4).

Farshi et. al. built on the study from Lu et. al. and included detailed heat exchanger and cost models in a combined ejector and double effect absorption cycle that utilized heat sources at temperatures where a single cycle may not operate efficiently [82]. Thermodynamic and exergoeconomic performance of the combined cycle was compared to a traditional double effect absorption system. The cycles are heated by steam at 127°C, reject heat to a cooling water stream at 29°C, and chill a water stream from 12°C to 7°C. In the combined ejector double effect absorption refrigeration system, one stream of water vapor from the high pressure generator is sent to the primary nozzle in the ejector. This draws some water vapor from the low pressure generator and then the mixed streams are sent to the condenser. For a 300 kW refrigeration load, the combined cycle is more suitable for heat source temperatures from 92°C to 157°C because it has a higher COP than the double effect absorption and single effect absorption systems in that range. The second part of the study coupled the thermodynamic model to an exergoeconomic model [83]. Cost models were applied to the heat exchangers, pump, motor, and the valves in the system. Detailed heat exchanger calculations were performed to calculate the total heat exchange area of each heat exchanger. The condenser and generators were modeled as horizontal single pass shell and tube heat exchangers. Solution heat exchangers were modeled as tube in tube heat exchangers. The absorber and evaporator were modeled as a vertical single pass shell and tube heat exchanger. Then, a parametric study was performed on the temperatures in the high pressure generator, condenser, absorber, and evaporator as well as the effectivenesses of the heat exchangers to understand how the total investment cost was influenced by these parameters. Similar performance trends as other thermally activated cooling system were found. Lower total system costs are realized when the saturation temperature in the high pressure generator and the evaporator are increased. System costs are lowered when the condenser saturation temperature is decreased and the effectivenesses of the solution heat exchangers are low. When compared to a traditional double effect LiBr-water system, the investment cost of the combined cycle was lower. The cost of the combined cycle was \$50,120, yielding \$167 per kW_{th}, while the cost of the double effect system was \$61,860 which gives a specific cost of \$206 per kW_{th}. This is the most comprehensive study available in the literature because it provides a high-fidelity examination into technoeconomic performance of the absorption chiller, including integration of heat exchanger models into full system performance.

There are a number of studies investigating the exergoeconomic performance of absorption cycles, but each study lacks an important consideration. Almost all of the studies perform detailed thermodynamic cycle modeling. Some of the studies integrate the thermodynamic cycle models with heat exchanger models. The studies that integrate thermodynamic cycle models and heat exchanger models typically use highly simplified heat exchanger models that have potential to be inaccurate. This is a problem in the literature because heat exchangers are the most expensive component and have the largest impact on the system performance. Significant work must go into heat exchanger design to optimize technoeconomic performance. The two studies from Farshi et. al. are the only works that integrate thermodynamic, heat exchanger, and high fidelity economic models to perform a comprehensive technoeconomic study and truly understand the economics of absorption refrigeration systems.

2.2. Organic Rankine-Vapor Compression Refrigeration

The organic Rankine-vapor compression cycle (ORVC) uses waste heat to drive a turbine that provides power to a compressor which runs a vapor compression system. A process flow diagram of the ORVC is shown in Figure 2-3. The turbine and compressor can be mechanically or electrically coupled. The simple organic Rankine cycle utilizes waste heat to boil an organic working fluid in a boiling heat exchanger. After this, the vaporized working fluid is expanded through a turbine that provides power to the compressor. Then, the working fluid is cooled to a liquid phase in a condensing heat exchanger. The liquid working fluid is pumped to a higher pressure and sent to the boiler, which completes the cycle. On the simple vapor compression cycle, a liquid refrigerant is evaporated in a chilling heat exchanger to provide the desired cooling. The vaporized working fluid is brought to a higher pressure through the compressor and then cooled until it becomes a subcooled liquid in the condensing heat exchanger. The liquid working fluid is

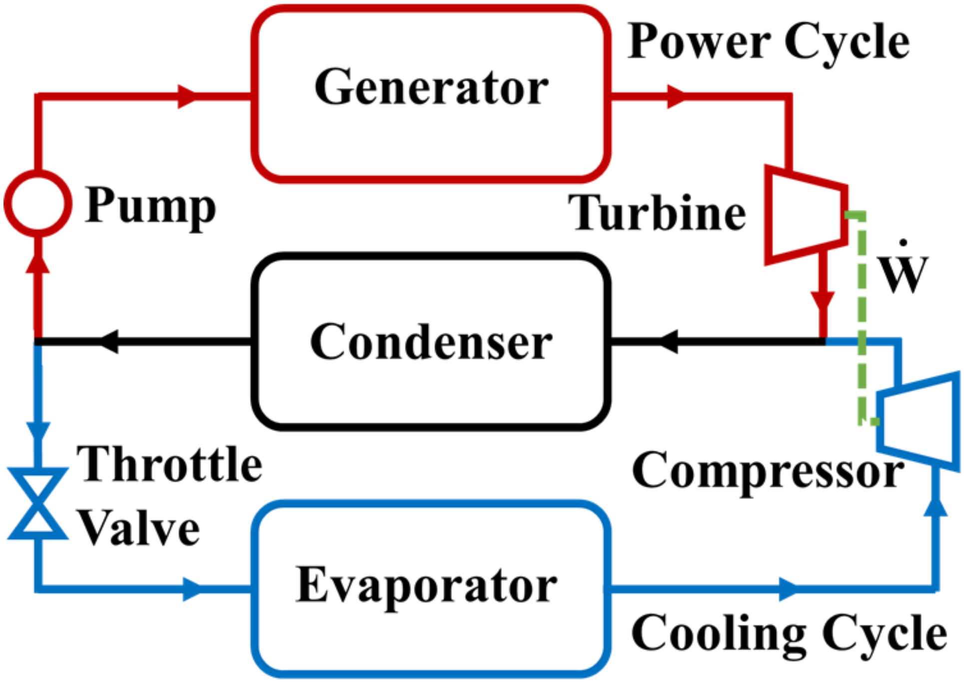

Figure 2-3: Process flow diagram of the simple organic Rankine-vapor compression cycle for heat activated cooling.

sent through an expansion valve where its pressure and temperature is greatly decreased. Then, the working fluid returns to the chiller to complete the cycle. The typical ORVC system uses the same working fluid on the organic Rankine cycle (power cycle) and the vapor compression cycle (cooling cycle). In addition, the power and cooling cycles often share a single condenser to reduce overall heat exchanger footprint. The efficiency of the turbine and compressor are critically important to the overall COP of these systems. The COP of these systems are generally around 0.6, comparable to the absorption refrigeration system. The COP of the ORVC can be improved by incorporating recuperative heat exchangers on the power and cooling cycles. The following section will provide a review of the technology research on combined ORVCs. After that, the next section survey the literature regarding technoeconomic performance of ORVCs and two ORCs specifically for marine diesel waste heat recovery.

2.2.1. Review of technology research

The important studies regarding working fluid selection and advanced cycle configurations for the ORVC will be reviewed here. The choice of working fluid is essential for efficient conversion of heat into useful cooling in the ORVC. Additional components can be incorporated into the ORVC to improve thermodynamic performance. These two facets of current technology research into ORVCs will be explored here. Unfortunately, there is not as much research available on the ORVC as there is on the absorption, adsorption, or ejector cycles.

Kim and Blanco analyzed a combined ORVC that utilized the same working fluid on both sides for cooling and electricity production [84]. The organic Rankine cycle had a recuperator and both cycles shared a single condenser. The ORC was driven by 150°C hot air at a flow rate of 1 kg s^{-1}. Eight different working fluids were examined, including ammonia, R134a, and butane. The condensing water temperature was 25°C and the evaporator saturation temperature was set to 5°C.

A parametric study of the cycle performance using the turbine inlet pressure, turbine inlet temperature, and the flow division ratio was completed. The flow division ratio is defined as the mass flow through the organic Rankine cycle divided by the mass flow through the condenser (or the total mass flow). Using this parameter, the system could produce cooling, power, or a combination of both. To produce only electricity, the flow division ratio was set to unity so all of the fluid was contained in the ORC and thus no fluid went through the vapor compression cycle. Any flow division ratio less than unity would produce cooling and power. There exists a critical flow division ratio where all of the power produced from the organic Rankine cycle is used by the compressor on the cooling cycle and there is no net power output. Refrigerants with high critical temperatures had the highest refrigeration capacity when the turbine pressure was low. For example, butane had a refrigeration capacity of 140 kW when the turbine inlet pressure was 14 bar, while R134a had a refrigeration capacity of 75 kW. Refrigerants with low critical temperatures have higher refrigeration capacity when the turbine inlet pressure is higher. At 26 bar, butane had a refrigeration capacity of about 70 kW while R134a had a capacity of 150 kW. All working fluids saw improvements in thermal efficiency as turbine inlet pressure increased. Thermal efficiency was defined as the sum of net power output and refrigeration capacity divided by the heat input. As the flow division ratio increases from the critical value, the refrigeration capacity decreases and the net power increases. At all turbine inlet pressures, butane, isobutane, and propane had the highest overall thermal efficiencies and the smallest total number of transfer units (NTUs) for the heat exchangers. Low NTU values imply the heat exchangers are smaller. For isobutane, the ideal turbine inlet temperature was 102°C to maximize cooling capacity. The net power output saw a similar trend where the maximum power output was achieved with a flow division ratio of 1.0 and a turbine inlet temperature of 102°C. At this point with isobutane, the power output was 30 kW.

Increasing turbine inlet temperature and pressure decreased the total number of transfer units for the heat exchangers in the system, denoting smaller and cheaper devices. Barring any practical flammability concerns, natural hydrocarbon refrigerants are the best choice for this ORVC due to their high thermal efficiencies and small heat exchanger sizes.

Li et. al. expanded on the work from Kim and Blanco to better understand which hydrocarbon refrigerants are most suitable for use in an ORVC [85]. In this work, a working fluid study of hydrocarbon refrigerants for use in an organic Rankine cycle coupled to a vapor compression cycle for low grade waste heat recovery was performed. The turbine and compressor are directly coupled, both cycles use the same working fluid, and they share a common condenser. The working fluids in this study were R290 (propane), R600 (butane), R600a (isobutane), and R1270 (propylene). Two performance metrics were used to characterize the system: overall COP and the working fluid mass flow rate per unit of cooling capacity. From the simulations, R600 had the highest overall COP through the range of boiler temperatures. At 80°C, the highest COP was 0.40 for R600 and the lowest COP was 0.32 for R1270. In addition, R600 had the lowest mass flow rate per unit of cooling capacity, indicating that this system provided the highest amount of cooling with the lowest flow rate. Lower flow rates are desirable to decrease parasitic losses from pressure drop and pumping power. The turbine pressure ratio increased while the compressor pressure ratio decreased as the boiler and evaporator saturation temperatures increased. Increasing the condenser saturation temperature had the opposite effect on the turbine and compressor sizing. The turbine pressure ratios for all of the working fluids were within 5% of each other. When the boiler temperature was 80°C with R600, the turbine pressure ratio was 2.75 and the compressor pressure ratio was 2.1. The largest compression ratio of 2.6 was found with R290 at a boiler saturation temperature of 80°C. Similar to the previous work from Kim and Blanco, this study found that hydrocarbon refrigerants are a thermodynamically favorable choice for low temperature heat recovery in organic Rankine vapor compression cycles.

Another working fluid study that incorporated hydrocarbon refrigerants was completed by Bu et. al., where four different working fluids were examined for a solar heat driven organic Rankine-vapor compression system, designed for ice production [86]. The boiler on the organic Rankine cycle is a parabolic trough solar collector where working fluid is pumped through the tubes and vaporized directly by solar energy. The same working fluid is used on both sides and the turbine and the compressor are directly coupled. The performance of R600, R600a, R123, and R245fa was examined for the ice making system. The evaporator saturation temperature was held constant at -5°C while the boiler saturation temperature ranged from 60°C to 160°C and the condenser saturation temperature ranged from 35°C to 45°C. The total direct solar radiation value used in this study corresponds to a location on the border between the United States and Canada or in the southeastern region of China. Similar trends to others mentioned previously in this literature review were found: increasing the boiler temperature and decreasing the condenser temperature will improve the overall COP of the system. The overall COP of the system for all working fluids is within 5% until the boiler temperature reaches 110°C. When the boiler temperature was greater than 110°C, the R123 system had a significantly higher COP than the other systems and reached a maximum value of 0.65 at 150°C. R600a reached a maximum value of 0.45 at 120°C while R245fa and R600 had a maximum COP of 0.50 at 130°C. In terms of the turbine and the compressor, the R600 and R600a systems had the most favorable characteristics. The specific volume ratio and the size of the turbine was the lowest for these two working fluids. In addition, the compressor pressure ratio (CPR) was the lowest and the ratio of vapor compression COP to CPR was the highest for R600 and R600a, implying that these systems can get the most cooling for the least amount of compressor work. The R600 had a sub atmospheric pressure at the compressor inlet which means air can leak into the system, and poses a practical hazard to operation. Thus, R600a is the most viable working fluid for the range of conditions examined in this study from a practical and equipment cost perspective. In terms of strictly thermodynamic performance, the R123 system had the best overall performance of all the working fluids, but the turbomachinery characteristics were not as favorable as the R600a system. The viability of a solar heat driven ORVC was demonstrated in this study. The system performance and payback period should be examined further to determine if a dry cooled condenser or a wet cooled condenser would be more appropriate to reject heat from the ORVC.

The previous working fluid studies were performed for strictly subcritical ORVCs, but the work from Li et. al. and performs a working fluid study for a transcritical ORVC [87]. The work theoretically analyzed an internally recuperated transcritical organic Rankine cycle coupled to a vapor compression chiller. The transcritical ORC was driven by waste heat available in flue gas. R22, R134a, and R290 were examined for use in the ORVC. The transcritical cycle allows the working fluid temperature profile to more closely follow the waste heat temperature profile which decreases the irreversibilities in the boiler, improving the system COP. The power and cooling cycles shared the same air coupled condenser, which implies the same working fluid was used on both cycles. The turbine on the organic Rankine cycle was connected to a generator and the compressor. The system could be run in full refrigeration mode where all of the power output is used to drive the compressor, part load mode where some of the turbine power is used to produce electricity and some to drive the compressor, or full electrical load where all of the turbine power is used to produce electricity. The organic Rankine cycle was driven by 190°C exhaust gas and the outlet temperature of the exhaust was set to 100°C with a mass flow rate of 10 kg s^{-1} which yields a heat input of approximately 980 kW. The saturation temperature in the evaporator was 7°C and in the condenser was 60°C. The condenser rejected heat to 35°C ambient air, while the outlet temperature of the chilled water was 10°C. In full refrigeration mode with R134a, the system could provide approximately 330 kW of cooling that resulted in a COP of 0.34. The total exergy destroyed and exergetic efficiency in the system decreased when increasing the condenser saturation temperature. The exergetic efficiency decreased because it scales with cooling capacity, which decreases sharply as the condenser saturation temperature increases. In this configuration, refrigeration power and electrical power are linearly related so that in the part load operation, as the refrigeration capacity increases, the electrical power output decreases accordingly. When the system was simulated in full electric mode, it was able to produce about 140 kW of electric power which yields approximately 13% thermal efficiency for the ORC. When the system was in full refrigeration mode, R134a had the highest refrigeration output at 330 kW. This study is interesting because the overall system COP was lower than others reviewed above, but the ORC thermal efficiency is slightly higher. The recuperated transcritical ORC has a better efficiency than the subcritical ORCs in previous studies. Regardless of the COP, the work provides a good theoretical base for an experimental investigation into the transcritical ORVC for combined power and cooling.

As shown above, thermodynamic performance improvements can be realized by choosing the correct working fluid to the ORVC based on the operating conditions (driving heat source temperature, heat sink temperature). In addition, the choice of working fluid has a significant impact on the size, speed, geometry, and pressure ratio of the turbine and compressor. The relevant research regarding advanced cycles will be presented next as a means to further improve thermodynamic performance.

A study that investigated using advanced positive displacement machinery in the ORVC was performed by Wang et. al. [88]. The study theoretically and experimentally investigated the performance of a combined organic Rankine cycle and vapor compression cycle that utilized a scroll expander and compressor and microchannel heat exchanger technology. The ORVC was driven by waste heat from stationary and on road internal combustion engines. The vapor compression refrigeration cycle had a nominal cooling capacity of 5 kW. A hot oil loop at 200°C was used to simulate the waste heat source on the internally recuperated power cycle. There was a direct mechanical coupling between the expander and compressor using a torque sensor, which eliminated the mechanical to electrical energy conversion losses. The power cycle used R245fa and the cooling cycle used R134a as working fluids. The experimental investigation rejected heat to 22°C ambient air in the condensers, while the cooling cycle provided refrigeration to ambient air at 22°C. They used plate heat exchangers for the boiler and recuperator, while using microchannel heat exchangers for the condensers and chiller. A maximum cooling capacity of 4.25 kW was achieved at an overall system COP of 0.47. The expander power output at this point was 0.92 kW and the isentropic efficiency of the expander was nominally 80%. This study experimentally showed that the ORVC can operate efficiently with scroll machinery, which offer a smaller alternative with lower mass than traditional turbomachinery. High efficiency targets can be met more easily with scroll machinery in comparison to traditional rotating machinery.

To take the previous analysis one step further, Wang et. al. simulated various different configurations for the ORVC to maximize the COP of the system [89]. Three different system configurations were examined: a baseline cycle with a recuperator on the power cycle, a cycle that adds a subcooler between the condenser and expansion valve on the cooling cycle, and a cycle that includes a suction line heat exchanger on the cooling cycle to transfer heat from the subcooler outlet to the evaporator outlet. In all configurations, the power and cooling cycle share a single condenser as shown in Figure 2-4. The cycle was simulated when the evaporator saturation

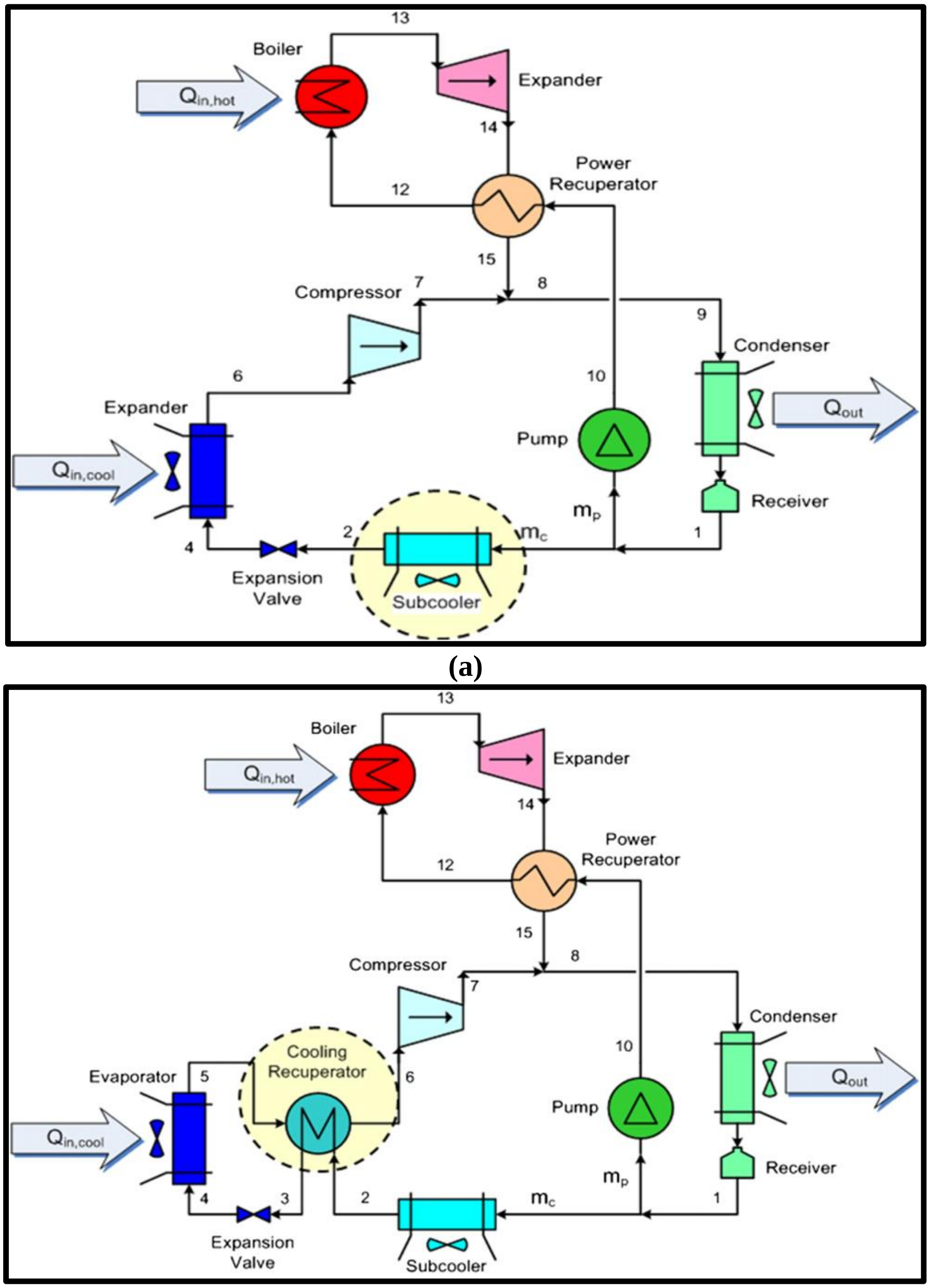

Figure 2-4: The advanced ORVC cycles with (a) subcooler before the expansion valve and (b) suction line heat exchanger after the chiller and subcooler [89].

temperature was 18°C and the condenser saturation temperature was 67°C. The temperature lift is high because the system was designed to reject heat from the condensers to ambient air at 48.9°C and cool indoor air at 32°C. In the simulations, R245fa was used in both the power and cooling cycles. The cycle with additional subcooler improves the COP of the baseline system from 0.54 to 0.63, which can reduce overall weight and size of every component because the subcooling heat exchanger is approximately 1/8th the size of the condenser. The suction line heat exchanger has a smaller effect on the COP, improving from 0.63 to 0.66. Although it did not have a large impact on the COP, the suction line heat exchanger is useful because it provides additional superheat at the compressor inlet which can help prevent working fluid condensation during the compression. Increasing the saturation temperature in the condenser decreased the COP of the system and increased the total system weight while increasing the evaporator saturation temperature and the isentropic efficiency of the expander will increase the COP and decrease the weight. The isentropic efficiency of the expander has the largest impact on system performance and weight. There was an optimal high side pressure on the power cycle which maximized COP and minimizes weight, at approximately 3200 kPa. The optimum value for the effectiveness of the power cycle recuperator was 0.85, where the performance is maximized and the system weight is minimized. Concepts for two advanced ORVC systems were also proposed: a system with a second recuperator where heat is transferred from the compressor outlet to the stream exiting the power cycle pump and a system where two different fluids are used on the power and cooling cycles. The second recuperator allows a closer match between heat capacities entering the first recuperator on the power cycle which will decrease heat transfer irreversibilities. Using different fluids on the power and cooling cycles can maximize the COP by tailoring operating conditions to the specific cycles. The high boiling point of R245fa increased the size of the compressor and chilling heat exchanger on the cooling cycle, highlighting an opportunity for potential improvements by using different fluids. This study shows that a number of components can be added to the ORVC to improve thermodynamic performance. The additional components can also decrease the size and weight of the system, improving viability in spaces where footprint is a concern (transportation sector, for example). Another work that sought to characterize the performance of an ORVC using positive displacement machines was carried out by Aphornratana and Sriveerakul [90]. This study theoretically investigated a recuperated organic Rankine cycle directly coupled to a vapor compression chiller for low grade waste heat recovery. In this work, the ORVC uses a free-piston expander-compressor unit to link the power and cooling cycles. The free-piston expander-compressor makes it more suitable for small scale refrigeration because of its high efficiency at small sizes. A schematic of this system is shown in Figure 2-5. The unit has two pistons connected via a shaft that transfer power from the ORC to the vapor compression cycle. On the organic Rankine cycle, the high pressure and temperature working fluid leaving the boiler enters the left

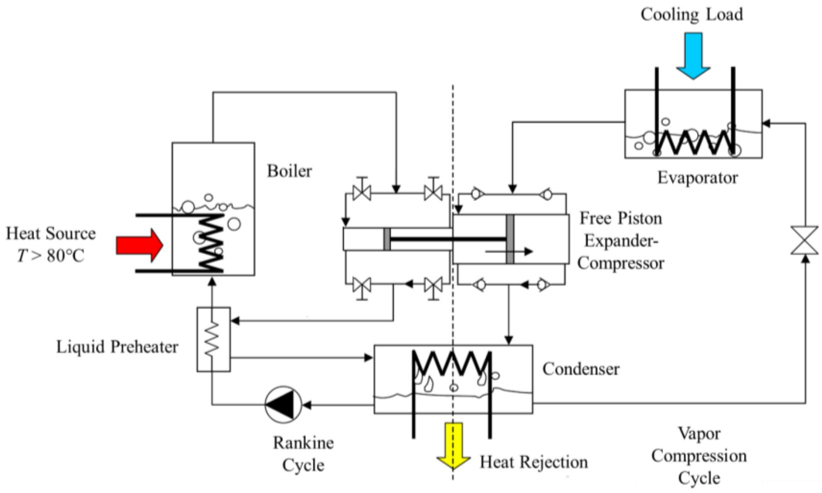

Figure 2-5: Schematic of the small scale organic Rankine-vapor compression cycle where the cycles are connected with a Free Piston Expander-Compressor [90].

chamber of the device and pushes the piston to the right. The movement of the piston to the right compresses the working fluid in the right chamber which provides the necessary driving force for the refrigeration cycle. The ORC and vapor compression cycle shared a condenser and used the same working fluid. The compressor piston had a fixed cross section of 20 cm^2 with a fixed stroke length of 15 cm. Then, a parametric study was completed to understand the performance of the system based on boiler, condenser, and evaporator saturation temperatures. As the chiller and boiler saturation temperatures are increased, the cross sectional area of the expander decreases while increasing the condenser saturation temperature has the opposite effect. The cross sectional area of the expander decreases when increasing boiler temperature because the density of the refrigerant increases with temperature and pressure. The cooling duty was independent of boiler temperature because the geometry of the compressor and the properties at the chiller outlet were fixed. Increasing boiler temperature, decreasing condenser temperature, and increasing chiller temperature improve the COP of the system. When the boiler saturation temperature was 80°C, the condenser saturation temperature was 35°C, and the chiller saturation temperature was 5°C, the system had a COP of 0.40 with a cooling duty of 0.75 kW. The system could even utilize waste heat at temperatures as low as 60°C but the COP decreased to 0.28. This work demonstrates that the free piston expander-compressor is a promising technology for small scale, heat driven refrigeration. Further experimental work is needed to confirm the simulation results.

Again, the important trends from the ORVC studies are similar to other thermally activated cooling systems, as presented above. For small scale refrigeration, positive displacement devices (scroll machinery or free piston expander-compressor) are viable options as opposed to traditional rotating machinery. The typical COP for the ORVC is around 0.6, comparable to single-effect absorption systems. A summary of the above ORVC studies is presented in Table 2-2.

Table 2-2: Summary of technology studies for ORVC cycles.

Authors	Working Fluid	Generator Temp.	Condenser Temp.	Chiller Temp.	COP	Cooling Duty
-	-	°C	°C	°C	-	kW
Aphornratana et. al. [90]	R134a	80†	35†	5†	0.4	0.75
Bu et. al. [86]	R600a	120	40†	-5†	0.45	-
Kim et. al. [84]	R600a	150	25	5†	-	140
Li et. al. [87]	R134a	190	35	10	0.34	330
Li et. al. [85]	R600	80†	40†	5†	0.4	-
Wang et. al.[e] [88,89]	R134a	200	22	22	0.47	4.25

Note: The external stream temperatures are provided unless otherwise designated.
All studies with experimental component are labeled with [e].

† Saturation temperature

2.2.2. Review of technoeconomic research

The technoeconomic research on the combined organic Rankine-vapor compression cycles is extremely limited. Only two papers studying the technoeconomic performance of an ORVC were found and will be presented below. Since there are no studies that describe the technoeconomic performance of ORVCs specifically applied to waste heat recovery onboard marine vessels, the technoeconomic performance of the two traditional organic Rankine cycles for marine diesel waste heat recovery will be presented as well.

A study that examined the energetic and economic performance of a novel Vehicle Energy System (VES) was performed by Yue et. al. In this work, an organic Rankine cycle and a vapor compression refrigeration cycle were integrated onto a turbocharged 176 kW diesel engine [91]. The waste heat from the exhaust of the turbocharger vaporized the refrigerant on the ORC. The mechanical power from the turbine is used to produce additional electricity in a generator. Some of the electricity generated from the ORC is used to drive the compressor on a vapor compression refrigeration cycle which provides cabin air conditioning. Cost models were applied to the major components in the system including the turbine, heat exchangers, pump, working fluid, piping, and liquid holding tank. The generators or the vapor compression system were not included in cost modeling. The heat exchangers in this study were plate type for the evaporators and condensers. Four different working fluids were examined: n-pentane, R245fa, R134a, and cyclopentane. The ambient temperature was 30°C and the outlet temperature of the turbocharger exhaust was set to 577°C. The cooling duty of the vapor compression cycle was 30 kW. The heat transfer area of the boiler was fixed at 10 m^2 and the overall heat transfer coefficient of the boiler was set to 0.13 kW m^{-2} K^{-1}. At these conditions, R134a had the best thermodynamic and economic performance, achieving a thermal efficiency of 9.7% and a power output of 16.5 kW with R134a. The system had an initial investment cost of $7,200 and a payback period of about 4818 operating hours. The system reduced fuel consumption because the automobile no longer diverted power from diesel engine to drive the vapor compression chiller. The R245fa system had the worst performance and yielded a payback period of 5427 hours and a thermal efficiency of 8.4%. The proposed ORVC system improved the thermal efficiency of the engine by about 10% in all working fluid cases. As is the case for all thermally activated cooling systems, the performance of the system improves when the boiler temperature increases, the condenser temperature decreases, and the evaporator temperature increases. This study performed a robust TEA for an ORVC specifically designed for waste heat recovery which coupled thermodynamic, heat exchanger, and cost models.

Another study, from Molés et. al., performed a technoeconomic analysis and working fluid study on an ORVC [92]. The working fluid study examined low global warming potential (GWP) refrigerants on the power and cooling cycles. On the ORC, the performance with R1233zd(E) and R1336mzz(Z) was analyzed, which have a GWP of 1 and 2, respectively, and similar properties to R245fa. On the vapor compression system, the thermodynamic performance with R1234yf and R1234ze(E) was examined, which have zero GWP and similar properties to R134a. The system had a recuperator on the power cycle, a suction line heat exchanger on the cooling cycle, and a cross cycle recuperator. The cross cycle recuperator uses the hot fluid leaving the compressor to pre-heat the fluid leaving the pump in the power cycle. System performance was studied by sweeping through a range of saturation temperatures in the boiler, condensers, and chiller. Similar trends were found regarding overall system performance and saturation temperatures as previous studies (to improve performance: raise saturation temperatures in the boiler and chiller, lower saturation temperature in the condenser). R1336mzz(Z) had higher ORC efficiency throughout all simulations until the power cycle condenser saturation temperature reached 47°C, above which R1233zd(E) had higher ORC efficiency. Using R1234ze(E) on the vapor compression side resulted in higher temperatures at the compressor outlet which increased the amount of heat transferred between cycles and improved the performance of the ORC. The two working fluids on the vapor compression cycle had only small differences, but R1234ze(E) had a slightly higher vapor compression COP throughout the range of design conditions. The COP ranged from 0.3 to 1.1 for the overall cycle. Using R1336mzz(Z) on the ORC had a slightly higher overall COP than R1233ze(E). A feasibility study was performed on the economics of implementing the advanced configuration for the ORVC. The feasibility study used R1336mzz(Z) and R1234ze(E) on the power and cooling cycles, respectively, and assumed a condenser saturation temperature of 27°C, boiler saturation temperature of 127°C, and an evaporator saturation temperature of 2°C. The system provided cooling for 4000 hours of the year and produced electricity for the other 4000 hours of the year. It was assumed that the heat source in the feasibility study was freely available at no cost, i.e. waste heat. The system had an overall COP of about 0.84 and could provide 100 kW of cooling or 16.23 kW of electricity. Assuming an energy cost of $0.15 per kWh, the ORVC system could save $17,603 per year and have a payback period of 3.2 years. The cost of the system was estimated to be $55,644. This study is significant because it shows that reasonable payback periods can be achieved with the ORVC. In addition, it provides some insight into the performance of modern low GWP working fluids and shows that certain working fluids have better performance at high ambient temperatures.

Since the only technoeconomic studies on the ORVC found in the literature were provided above, the review will transition to marine diesel waste heat recovery with organic Rankine cycles.

Another technoeconomic and working fluid study was performed by Wang et. al. for an organic Rankine cycle designed to recover low grade waste heat available in flue gas from a marine diesel engine [93]. In this work, the ambient air temperature was 20°C while the flue gas inlet temperature varied from 150°C to 250°C. In addition, the pinch point temperatures in the boiler and the condenser were set to be 5°C or greater. Eleven different working fluids were examined for the organic Rankine cycle and included isentropic, dry, and wet fluids. Cost models were applied for the heat exchangers, pump, turbine, cooling fan, and the generator while setting the cost of electricity at a constant value of $0.10 per kWh in the payback period analysis. When the flue gas inlet temperature was 150°C, all of the working fluids examined had comparable payback periods (around 12 years), but R236fa had the highest power output (90 kW). At this design point, isobutane had the next highest power output of nearly 75 kW. When the flue gas inlet temperature is raised to 200°C and 250°C, R236fa, R245fa, and R113 are the optimal working fluids in terms of payback period and power output. The working fluid that yielded the shortest payback period does not necessarily have the highest power output or system thermal efficiency. This is an important point that many researchers overlook: sometimes the cost of high efficiency systems is not worth the extra investment cost from the perspective of the end user. Most of the research on waste heat recovery aims to maximize thermodynamic efficiencies, but lack a detailed analysis of the system economics. In addition, maximizing thermodynamic efficiencies should not be a major concern if the heat source is ‘free’.

Another work that examined the viability of marine diesel waste heat to power was completed by Yang and Yeh [94]. This study performed a thermoeconomic optimization of an organic Rankine cycle designed to recover waste heat from a marine diesel engine in the cooling jacket and the exhaust gas. The Net Power Output Index (NPI) was used as a metric to gauge the thermoeconomic performance of their system. The NPI is the ratio of net power output to the total system cost, where a higher NPI denotes more power output per dollar spent on implementation. The engine considered in this study was a 6 cylinder WARTSILA marine diesel engine with power rated at 34.3 MW. The exhaust gas mass flow rate of this engine is 267,323 kg hr^{-1} and the cooling jacket water volume flow rate was 273 m^3 hr^{-1}. The cooling jacket water heats the working fluid from a subcooled liquid to a saturated vapor and then the vapor is superheated by the higher temperature exhaust gas in a second heat exchanger. The evaporator, superheater, and condenser were designed as shell and tube heat exchangers that were subdivided into 20 regions to accurately simulate heat exchanger performance. Empirical heat transfer correlations were used to determine the overall heat transfer coefficient and the total area of each heat exchanger. Cost models were applied to each heat exchanger, the pump, and the turbine to get the total system cost. The exhaust gas inlet temperature was 170°C and the cooling jacket water inlet temperature was 90°C while the cooling water inlet temperature was 25°C. The turbine inlet pressure and temperature were varied to characterize the thermodynamic and economic performance of the ORC with five different working fluids: R152a, R245fa, R600a, R1234yf, and R1234ze. The system with R1234yf had the highest net power output and highest total cost at all turbine inlet pressures. As the turbine inlet pressure increased, the net power output, thermal efficiency, and total cost increased while the NPI increased and then decreased after it reached a maximum value. Each working fluid had nearly the same thermal efficiency throughout the range of turbine inlet pressures. The ORC with R1234yf had a highest overall NPI of 0.266 W $\$^{-1}$, which was achieved at a turbine inlet pressure of 2 MPa. R245fa had the lowest NPI of 0.245 W $\$^{-1}$. The ORC system in this work was compared to a traditional ORC that recovered waste heat only from the engine exhaust gas and found that the proposed system improves total thermal efficiency by an additional 6% compared to the traditional ORC. The fuel savings were not quantified to calculate a payback period of the system. The result from this work is interesting because the highest thermal efficiency system yielded the best thermoeconomic performance according to their NPI metric. The NPI metric may not be an accurate indicator of practical economic performance because there should be a point where further increases in thermodynamic efficiency are too costly to yield a reasonable NPI.

Building upon their previous study, Yang and Yeh also performed a payback period analysis of an ORC driven strictly by exhaust waste heat from a large marine diesel engine [95]. R1234ze, R245fa, R600, and R600a were analyzed as working fluids for the ORC. The inlet and outlet temperature of the exhaust gas was set to 180°C and 140°C, respectively while the mass flow rate was 20 kg s^{-1}. The condensing saturation temperature was set to 35°C and the turbine inlet temperature was 110°C. Cost models were applied to each heat exchanger, the pump, and the turbine to get a total system cost. For the baseline case, R245fa had the highest NPI at 0.159 W $\$^{-1}$, while R1234ze had the lowest NPI at 0.151 W $\$^{-1}$ and the highest thermal efficiency at 9.61%. Then, two separate optimization routines were performed using the high and low side system pressures. The aim of the first optimization was to maximize thermal efficiency. The second optimization routine sought to minimize payback period. The system with R1234ze had the highest thermal efficiency of 11.27% when parameters were optimized. The R600 system had the lowest thermal efficiency of 11.06% after optimization. When the systems were optimized for a minimum payback period, the R245fa system had the lowest payback period of 6.19 years while the R1234ze had the longest payback period of 6.52 years. The optimal turbine pressures for the payback period minimization were higher than for the thermodynamic optimization. In addition, the ORC system can reduce CO_2 emissions by 76% per kWh of electricity produced. It is interesting to note that in this study the results for working fluids were in disagreement with the previous work from Yang and Yeh. When the ORC is strictly driven by exhaust gas, R245fa has the best thermodynamic and economic performance. When exhaust gas and jacket water are used, R1234yf had the best performance and R245fa had the worst performance. The two studies are useful to understand waste heat recovery in the marine diesel sector.

As evidenced by the literature provided above, the technoeconomic work on the organic Rankine-vapor compression cycle is limited. Very few studies are available that examine the interaction between thermodynamic performance and economic performance. There are no studies that integrate thermodynamic modeling with heat exchanger modeling and economic modeling to get a detailed understanding of the technoeconomic performance of the ORVC. Additionally, there are no technoeconomic studies of the ORVC that specifically apply to marine diesel waste heat activated cooling. Thus, the present work fills the gap by building detailed models for thermodynamic, heat exchanger, and economic performance and applying the modeling platform to marine diesel waste heat recovery.

2.3. Research Needs for Thermally Activated Cooling Systems

The above literature review provides a summary of the current state of research into four thermally activated cooling systems: absorption, adsorption, ejector, and organic Rankine-vapor compression. There are a number of challenges associated with each of these systems. In the LiBr-water absorption system, a high condenser temperature can cause crystallization. During crystallization, the LiBr salt precipitates out of solution and solidifies. The solidification of the salt impedes system piping and heat exchangers and can completely halt the operation of the machine, discontinuing the cooling effect. This phenomenon can be challenging to remedy as it requires careful chemical balancing and heat cycling. The ammonia-water absorption system does not have this problem, but ammonia is an extreme health risk where leaking must be prevented at all costs. The adsorption system has a low COP and has poor heat transfer performance in the adsorption bed. This contributes to a very high ratio of system weight to cooling capacity. Further, the adsorption system must utilize multiple beds to provide continuous cooling which also compounds the high weight challenge and adds more complexity to the operation of the system. The primary challenges associated with the ejector refrigeration cycle are the low COP and inefficient operation of the ejector nozzles over a range of operating conditions. The nozzle design must be tailored to the operating conditions and working fluid to achieve efficient performance. The primary challenge with the organic Rankine-vapor compression cycle is the low efficiency of turbomachinery at small scales. Besides this, the ORVC can achieve good performance without the challenges that plague other heat activated cooling systems. Further, the ORVC has flexibility in regards to waste heat temperature, working fluid selection, and operating conditions.

Recently, a waste heat recovery system for utilizing low grade waste heat has been investigated to improve the viability of dry-air cooling for power plants [96,97]. The system examined in this study is a type of organic Rankine-vapor compression cycle, called a turbo-compression cooling system (TCCS), where a highly efficient centrifugal turbocompressor directly couples the organic Rankine power cycle and vapor compression refrigeration cycles. The turbine on the organic Rankine cycle and compressor on the vapor compression refrigeration cycle share the same shaft, which transfers power between the two cycles. To maximize the efficiency of both the turbine and compressor, different working fluids can be used on each side of the system. This increases the complexity of the system because a hermetic seal between the turbine and compressor is required. The application of the turbo-compression cooling system will determine if the increase in COP is worth the increased system complexity by using different working fluids. This system has the opportunity to increase the performance of traditional ORVC systems if the techno-economic performance can be evaluated.

In general, ORVCs have a much more limited body of work dedicated to understanding the thermodynamic performance than the absorption system. The limited amount of studies that examine the thermodynamics of the ORVC have been provided above, but none of these studies incorporate accurate heat exchanger modeling or economic modeling. Regarding ORVC literature, the specific needs for further research are as follows:

- Incorporate detailed heat exchanger models directly coupled to thermodynamic models. This would include specifying types of heat exchanger (shell and tube, plate frame, etc.) and using specific correlations from the literature to calculate heat transfer coefficients, pressure drops, and heat exchanger area.
- Incorporate accurate models of turbomachinery to understand how the turbomachinery affects system performance, including Cordier analyses to calculate size, speed, and efficiency of the machinery.
- Examine the effects of advanced cycle configurations on the technoeconomic performance of the ORVC. For example, answering the questions: Does including a power cycle recuperator drive the size of the boiling heat exchanger down? Is the

total size of the heat exchangers now smaller or larger by incorporating a recuperator? How does this affect total system cost? The answers to these types of questions would inform future designers on how best to utilize heat to provide useful cooling.

- Examine the economic performance of the ORVC to understand how the total cost of the system is related to the thermodynamic and heat exchanger performance. In addition, understanding how the end use application affects technoeconomic performance would be helpful. The technoeconomic analysis is essential for bringing the ORVC technology out of the research space and into the commercial market.

2.4. Specific Aims of this Study

The literature reviews shows there is a need for further investigation regarding the organic Rankine-vapor compression heat activated cooling system. The literature contains only one study that addresses the relationship between thermodynamic and economic performance of ORVC systems. This work aims to fill the gap in the literature with the following three specific aims:

- Develop a high fidelity thermodynamic, turbomachine, heat exchanger, and cost model for a turbo-compression cooling system (TCCS) designed to recover waste heat from the cooling jacket water in large marine diesel engines.
- Optimize the TCCS using the heat exchanger effectiveness as a parameter to find the minimum payback period from reducing fuel consumption.
- Characterize the effects of various working fluids on the technoeconomic performance of the system.

Completing the three specific aims will provide deeper insight in the technoeconomic performance of an organic Rankine cycle directly coupled to a vapor compression cycle with high fidelity heat exchanger models included the analysis. At the end of this work, recommendations for future analysis on the turbo-compression cooling system will be provided.

CHAPTER 3. Modeling Approach

There are a number of research needs on the organic Rankine-vapor compression cycle. Thermodynamic models coupled with high fidelity heat exchangers models are sparse in the literature. In addition, the analysis of the turbomachinery required for these systems is not prevalent in the literature. Further, there are very few studies that incorporate detailed economic models to understand the interaction between technical and economic performance of the ORVC.

A highly flexible modeling platform was develop to analyze the effects of various waste heat scenarios and working fluids on the thermodynamic, heat transfer, and economic characteristics of the turbo-compression cooling system. In this work, a single waste heat scenario was analyzed with five different working fluids to understand which working fluid had the most favorable thermodynamic and economic performance. In addition, a technoeconomic optimization was performed for each working fluid to determine the minimum payback period for the turbo-compression cooling system.

This chapter will provide an introduction to the turbo-compression cooling system. Then, a brief overview of the modeling approach will be provided before going into the specific details of the models developed in this work.

3.1. Turbo-Compression Cooling System

The turbo-compression cooling system is a waste heat recovery system designed to provide useful cooling from heat energy that is typically unused. The turbo-compression cooling system is comprised of an organic Rankine cycle and a vapor compression cycle that are coupled via a high efficiency centrifugal turbocompressor. A process flow diagram of a liquid coupled turbo-compression cooling system is provided in Figure 3-1. The organic Rankine cycle, or power cycle, contains a centrifugal turbine, a condensing heat exchanger, a working fluid pump, and a waste heat boiler. The waste heat boils the working fluid which is then expanded through the turbine. The turbine provides the work to the compressor which drives the vapor compression refrigeration cycle. Then, the power cycle fluid is condensed through a condensing heat exchanger and pumped to a higher pressure. Finally, the high pressure working fluid is heated in the waste heat boiler and the cycle is complete. The vapor compression cycle, or cooling cycle, has a centrifugal compressor, a condensing heat exchanger, an expansion/throttle valve, and an evaporating heat exchanger. The working fluid is compressed through the centrifugal compressor and then condensed through a condensing heat exchanger. Then, the pressure of the fluid is dramatically decreased through a throttling valve and it is boiled in an evaporating heat exchanger, which provides the cooling effect. After this, the vaporized working fluid is compressed by the centrifugal compressor and the cycle is complete.

The turbo-compression cooling system has a number of advantages over current state of the art technology. The high-efficiency turbocompressor and advanced heat exchanger technology allow the system to operate with a high COP. In addition, the power cycle and cooling cycle can

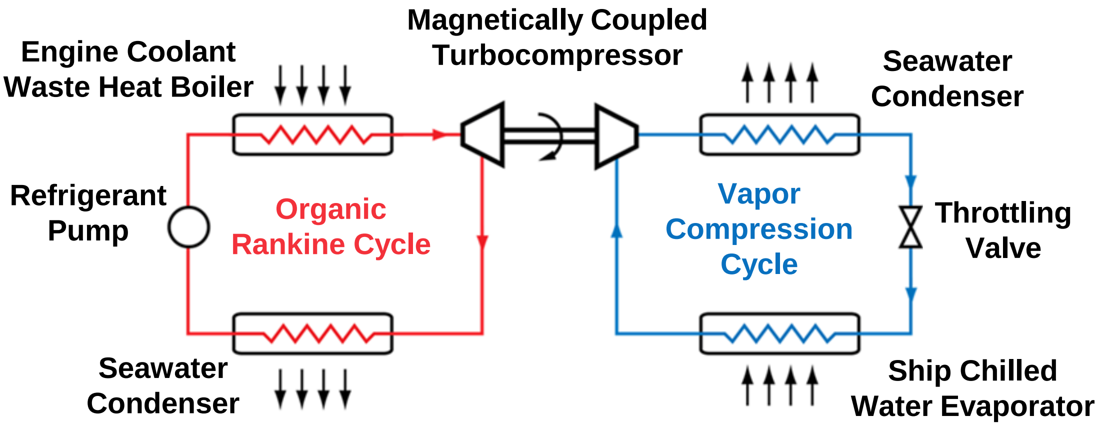

Figure 3-1: Process flow diagram for the waste heat driven turbo-compression cooling system with liquid coupled heat exchangers.

be designed with different working fluids to maximize the efficiency of the turbine and compressor and thus, the efficiency of the overall cycle. The design of the compact heat exchangers can be tailored to the specific waste heat phase and capacity while avoiding material compatibility issues. The system is highly flexible: it can be used for low, medium, and high grade waste heat with liquid or gas phase waste heat streams. In addition, the system may have a smaller footprint than absorption systems and does not use toxic/corrosive working fluids. A conceptual rendering of a liquid coupled turbo-compression cooling system is shown in Figure 3-2 with compact plate and frame heat exchangers. The turbocompressor linking the power and cooling cycles is at the center of Figure 3-2, while the evaporating heat exchangers are on the front right of the figure. The condensers that reject heat from each cycle are on the back of the skid as shown in Figure 3-2. Now that the working principles of the turbo-compression cooling system have been described, an overview of the technoeconomic modeling approach of this waste heat recovery system will be presented.

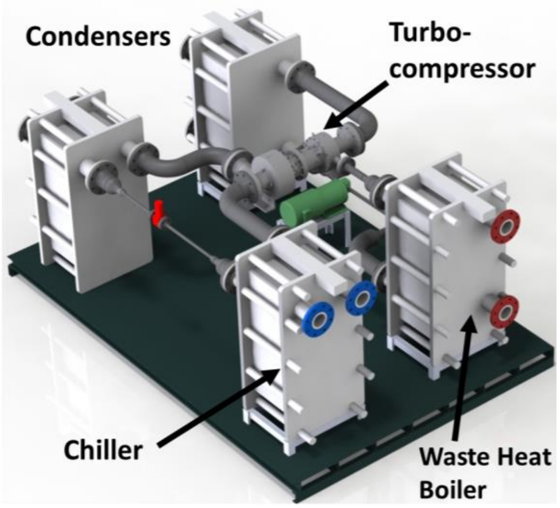

Figure 3-2: Conceptual solid model rendering of a liquid coupled turbo-compression cooling system with compact plate frame heat exchangers.

3.2. Overview of Modeling Approach

An overview of the modeling approach for the TCCS is given in Figure 3-3. The following sections of this chapter will present a detailed examination of each block of modeling. The thermodynamic block of modeling will be provided first. The thermodynamic block of the model used fundamental equations to calculate the state points at each location of the cycle, the refrigerant and external stream mass flow rates, the heat duties of the heat exchangers, and the size and speed of the turbo-compressor. In addition, a discussion on the importance of working fluid selection on system performance is provided. Further, a Cordier analysis to calculate the size and speed of the turbocompressor is presented. Using the relevant inputs from the thermodynamic model, the heat

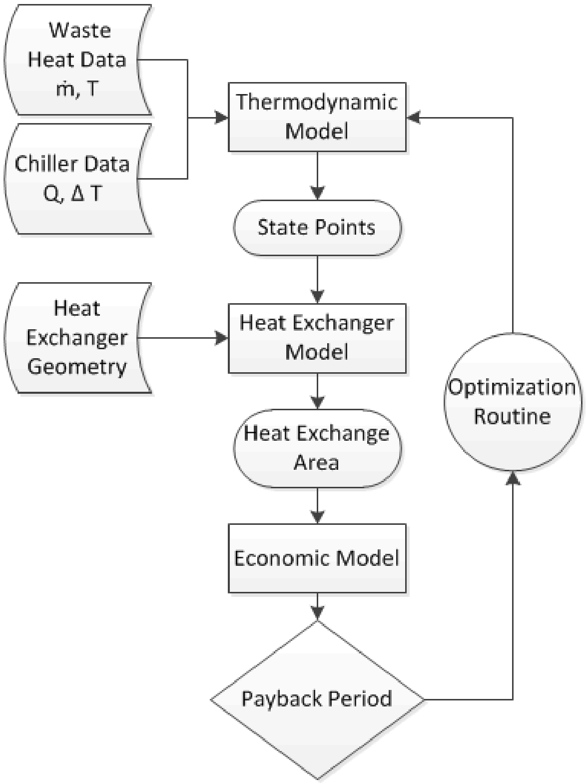

Figure 3-3: Block diagram of the modeling approach. The thermodynamic, heat exchanger, and cost models are coupled to perform the technoeconomic analysis and payback period optimization.

exchanger model used empirical correlations to determine the heat transfer coefficients and pressure drop through each region of all the heat exchangers. Then, the overall heat transfer coefficient was used to calculate the total heat exchange area of each heat exchanger in the system. The cost of each component in the system was calculated using high fidelity cost models. Using the amount of cooling provided from the turbo-compression cooling system, the amount of power displaced from the traditional electrically driven vapor compression systems was calculated, which translates to a reduction in expenditures on fuel. The total cost of the system was divided by the amount of money saved from reducing fuel consumption to calculate the simple payback period. Finally, the method of technoeconomic optimization is explained in detail to minimize the payback period of the turbo-compression cooling system. The coupled thermodynamic, heat exchanger, and economic set of equations was solved simultaneously using Engineering Equation Solver [98].

3.3. Thermodynamic Modeling

A set of fundamental thermodynamic equations was solved to understand the performance of the coupled organic Rankine cycle and the vapor compression cycle. The thermodynamic model was assumed to operate at steady state. Further, it was assumed that all the piping in the model was well-insulated, so there was no heat loss through pipe runs. It was also assumed the throttling valve on the vapor compression cycle was isenthalpic, so the enthalpy at the inlet and outlet of the valve are the same [99].

The waste heat stream examined in this study was the engine coolant of diesel engines on board large cargo ships. It was assumed that the condensers used seawater to cool and condense the working fluid on both the cooling and power cycles. Currently, some of the power produced by the diesel engines is routed to vapor compression systems which provide cooling for the ship.

The turbo-compression cooling system would replace the vapor compression chillers and use the engine coolant to provide the same cooling effect while reducing overall fuel consumption.

The constant inputs to the thermodynamic model are shown in Table 3-1. The engine coolant inlet temperature (90°C) and mass flow rate (78.5 kg s^{-1}) are typical of large diesel generator sets, while the boiler heat duty (2 MW) was a conservative input of how much waste heat is available in the engine coolant. The seawater condensing temperature (32°C) was a highly conservative estimate based on typical operating locations of cargo ships. Further, the chilled water temperature drop (12ºC to 7ºC) is typical for commercial chilled water delivery systems.

Table 3-1: Fixed inputs for the current study.

Fixed Inputs	**Value**
$T_{\text{boiler,i}}$	90°C
$\dot{m}_{\text{boiler}}$	78.5 kg s^{-1}
Q_{boiler}	2 MW
$T_{\text{seawater,i}}$	32°C
$\dot{m}_{\text{condensingwater}}$	250 kg s^{-1}
$T_{\text{chillwater,i/o}}$	12°C/7°C
$\eta_{\text{s,turbine}}$	0.80
$\eta_{\text{s,compressor}}$	0.80
$\eta_{\text{mechanical}}$	0.95
$\eta_{\text{s,pump}}$	0.80
$\eta_{\text{generator}}$	0.975
COP_{vc}	4
$q_{\text{combustion}}$	42,806 kJ kg^{-1}
$Cost_{\text{MGO}}$	\$533 mt^{-1}

The following sections will introduce and examine in detail the important pieces of the thermodynamic analysis, beginning with a discussion on the specifics of the full system model. After that, the importance of working fluid selection will be discussed, followed by the details of the thermodynamic calculations for each point in the cycles. Following the thermodynamic calculations, the Cordier analysis on the turbo-compressor will be presented.

3.3.1. Full System Model

A diagram of the turbo-compression cooling system cycle is provided in Figure 3-4. The heat exchangers were divided into sections where each region represents a different working fluid phase. The boiler and condenser heat exchangers were divided into three sub sections: superheated, two-phase, and subcooled (sh, tp, and sc in Figure 3-4). The chiller (cooling cycle evaporator) was divided into two sub sections: two-phase and superheated. The chiller had two regions because the fluid is two-phase after exiting the throttling valve. The boiler and condensers were modeled as counter flow plate heat exchangers, while the chiller was modeled as a parallel flow plate heat exchanger.

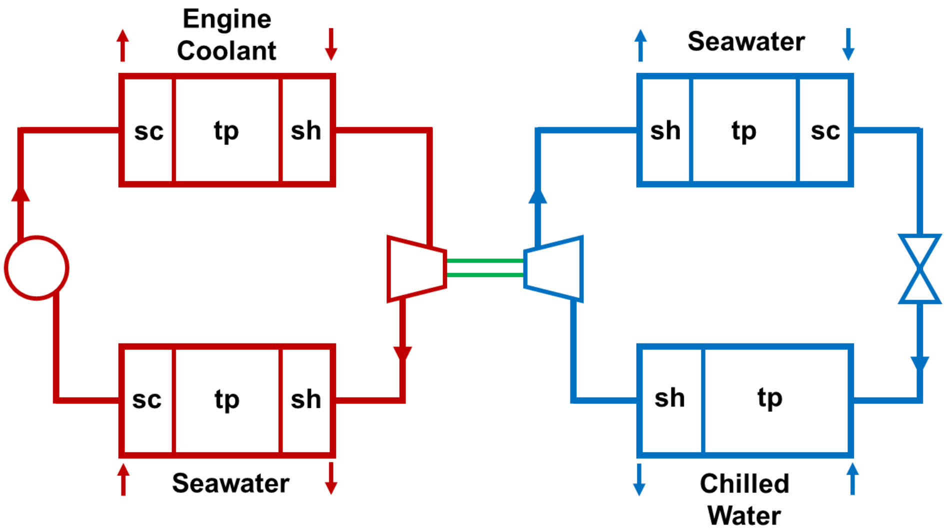

Figure 3-4: Cycle diagram of the turbo-compression cooling system with the heat exchangers divided into sections, each representing a different working fluid phase.

Temperature-entropy diagrams of typical organic Rankine and vapor compression cycles with R134a as the working fluid are shown in Figure 3-5. On the organic Rankine cycle, or power cycle, the waste heat boils a working fluid (2-3 in Figure 3-5b) which is then expanded through a high-efficiency centrifugal turbine (3-4). This high-efficiency turbine is mechanically coupled to a compressor which runs a vapor compression cycle. After expansion through the turbine, the working fluid is condensed in a condensing heat exchanger (4-1) and then pumped to a higher pressure (1-2). From there, the working fluid passes through the boiler and the cycle is complete. On the vapor compression cycle, or cooling cycle, the working fluid is compressed to a high pressure (1-2 in Figure 3-5a) and then condensed through a condensing heat exchanger (2-3). The liquid working fluid is passed through an expansion valve to decrease its temperature and pressure (3-4). After that, the working fluid is evaporated in a chilling heat exchanger to provide the cooling effect (4-1). The vaporized fluid is sent through the compressor and the cycle is complete.

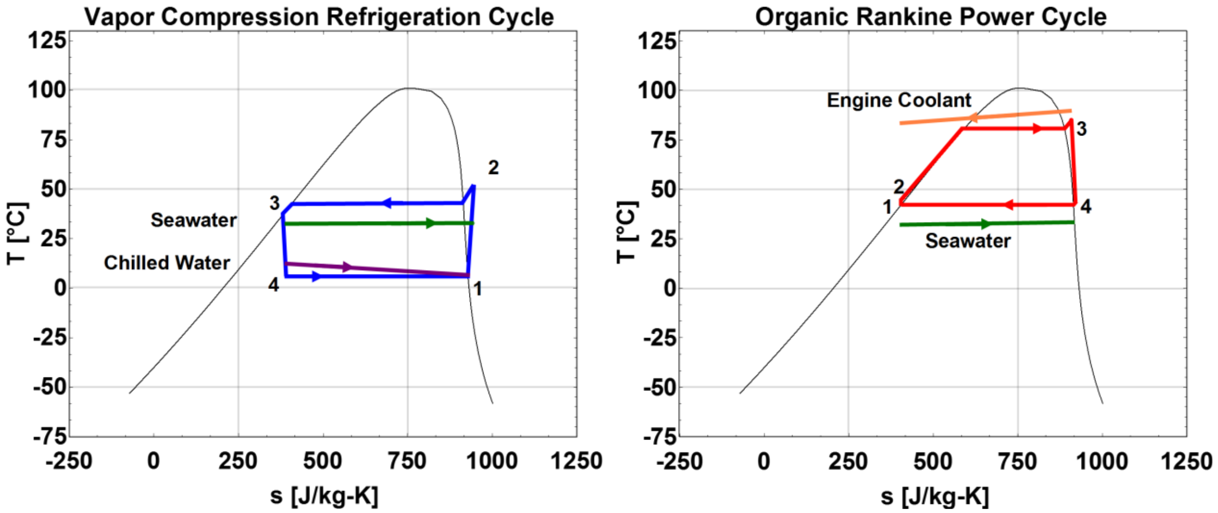

(a) (b)

Figure 3-5: Temperature-Entropy diagrams of representative (a) vapor compression refrigeration cycle and (b) organic Rankine power cycle with R134a as the working fluid. The engine coolant water flow (orange), cooling seawater flow (green), and chilled water flow (purple) are overlayed.

3.3.2. Working Fluid Selection

The choice of working fluid is critically important to the performance of both the power and cooling cycles. There are certain thermodynamic and physical characteristics of working fluids that make them particularly attractive for use in an ORC or a vapor compression cycle. The critical temperature and pressure must be sufficiently high to ensure the critical point is never reached.

Further, the slope of the saturated vapor line on a temperature-entropy diagram is an important factor for organic Rankine cycles. If a working fluid has a negatively sloped saturated vapor line, an isentropic expansion could drive the fluid into the two-phase region of the vapor dome. If liquid droplets form in the turbine as the fluid expands, the blades can be seriously damaged or begin eroding. A fluid with a negative slope is called a wet working fluid, and an example of this type is water. A fluid which has an infinite slope is called isentropic. This fluid is preferable to a wet working fluid, but a fluid that has a positive slope is the best candidate for an organic Rankine cycle. A dry working fluid (one with a positive slope) won't enter the vapor dome after it undergoes an isentropic expansion, which is ideal to preserve the turbomachinery.

In addition, there are several safety factors that make certain fluids attractive for use in these cycles. Due to the potential for leaks in real systems, the flammability, toxicity and environmental factors should be considered when choosing a working fluid. The Ozone Depletion Potential (ODP) and Global Warming Potential (GWP) are two important factors to consider. There are many working fluids that have favorable thermodynamic properties, but can cause serious harm to the ozone layer and contribute to global warming. The next generation of working fluids have low GWP and favorable thermodynamic properties.

This study examined five different working fluids, including next generation low-GWP refrigerants: R134a, R245fa, R1234ze(E), R152a, and R600a. The five different working fluids

Table 3-2: Characteristics of the working fluids chosen for this study. Each refrigerant had an Ozone Depletion Potential of zero.

Fluid	**GWP**	**Class**	**Type**	**Flammable**	**Toxic**	**T_{crit}/P_{crit}**	**Cost**
	(100 yr)	-	-	-	-	°C / kPa	\$ kg^{-1}
R134a	1430	HFC	Isentropic	No	No	101/4059	11.00
R245fa	1030	HFC	Dry	Yes	No	154/3651	41.40
R1234ze(E)	6	HFO	Isentropic	No	No	109/3632	33.00
R152a	124	HFC	Dry	Yes	No	113/4520	12.20
R600a	3	Natural	Isentropic	Yes	No	135/3640	41.80

examined in this study and their characteristics are compared in Table 3-2. R134a and R1234ze(E) were chosen in this work because they are used in state-of-the-art commercially available vapor compression chillers [100–102]. R245fa is a commonly used working fluid in commercially available ORC systems for low grade waste heat recovery [103]. R152a was chosen based on guidance from a recently constructed air-cooled turbo-compression cooling system [96,97]. R600a was chosen based on results found in the literature regarding the generally favorable performance of hydrocarbon refrigerants. The operating conditions of this TCCS ensure that none of the fluids will reach the critical point. The cost for the fluids was found based on quotes received from suppliers.

In the present study, the same working fluid was used on both the power and cooling cycles. Using the same fluid reduces complexity of the turbocompressor because a hermetic seal between the rotating shafts is not needed. Without the hermetic seal, the efficiency of the mechanical power transfer between the turbine and the compressor is higher.

3.3.3. Turbo-compression Cooling Thermodynamic Model

The following section will outline the governing equations used in the thermodynamic model and provide a representative calculation for the power cycle of the turbo-compression cooling system. Each subsection of the heat exchangers was modeled using energy balance and heat exchanger design equations. The set of Equations (3.1) - (3.3) was used to model each region of the heat exchanger. Equation (3.1) represents the heat transferred to or from the water side of the heat exchanger (engine coolant, condensing seawater, chilled water):

$$\dot{Q} = \dot{m}_{\mathrm{w}} c_{\mathrm{w}} \left(T_{\mathrm{i}} - T_{\mathrm{o}} \right) \tag{3.1}$$

where T_{i} and T_{o} represent the inlet and outlet temperatures of the water stream and c_{w} is the specific heat of the water. Equation (3.2) represents the heat duty of the heat exchanger:

$$\dot{Q} = \varepsilon C_{\mathrm{min}} \left(T_{\mathrm{h,i}} - T_{\mathrm{c,i}} \right) \tag{3.2}$$

where ε is the effectiveness of the heat exchanger, C_{min} is the minimum heat capacity rate, $T_{\mathrm{h,i}}$ is the hot fluid inlet temperature and $T_{\mathrm{c,i}}$ is the cold fluid inlet temperature. Equation (3.3) represents the heat transferred to or from the working fluid stream:

$$\dot{Q} = \dot{m}_{\mathrm{r}} \left(i_{\mathrm{i}} - i_{\mathrm{o}} \right) \tag{3.3}$$

where i_{i} and i_{o} are the inlet and outlet enthalpies of the working fluid.

The Coefficient of Performance of the turbo-compression cooling system was calculated with Equation (3.4):

$$COP = \frac{\dot{Q}_{\mathrm{chiller}}}{\dot{Q}_{\mathrm{boiler}} + \dot{W}_{\mathrm{pump}}} \tag{3.4}$$

The turbine was modeled using Equations (3.5) and (3.6):

$$\eta_{\mathrm{s}} = \frac{i_{\mathrm{i}} - i_{\mathrm{o}}}{i_{\mathrm{i}} - i_{\mathrm{o,s}}} \tag{3.5}$$

$$\dot{W}_{\mathrm{turbine}} = \dot{m}_{\mathrm{r}} \left(i_{\mathrm{i}} - i_{\mathrm{o}} \right) \tag{3.6}$$

where η_{s} is the isentropic efficiency of the turbine, $i_{\mathrm{o,s}}$ is the isentropic enthalpy at the turbine outlet, and $\dot{W}_{\mathrm{turbine}}$ is the power output of the turbine. The compressor and pump were modeled with Equations (3.7) and (3.8):

$$\eta_{\mathrm{s}} = \frac{i_{\mathrm{o,s}} - i_{\mathrm{i}}}{i_{\mathrm{o}} - i_{\mathrm{i}}} \tag{3.7}$$

$$\dot{W} = \dot{m}_{\mathrm{r}} \left(i_{\mathrm{o}} - i_{\mathrm{i}} \right) \tag{3.8}$$

where η_{s} is the isentropic efficiency of the compressor or pump, $i_{\mathrm{o,s}}$ is the isentropic enthalpy at the compressor or pump outlet, and $\dot{W}$ is the power output. The isentropic efficiencies of the turbine, compressor, and pump were set to 80%, as shown in Table 3-1. These values were selected based on realistic isentropic efficiency targets for centrifugal turbomachines at this scale and with guidance from the Cordier diagrams developed by Barber-Nichols, Inc. [96,97]. The turbine and compressor are directly coupled because they share a single shaft rotating at the same speed. The mechanical coupling has a torque transfer efficiency given by Equation (3.9):

$$\eta_{\mathrm{mech}} = \frac{\dot{W}_{\mathrm{comp}}}{\dot{W}_{\mathrm{turbine}}} \tag{3.9}$$

The next section outlines a Cordier analysis that determined the size and speed of the turbine and compressor, which are important factors to achieving the 80% isentropic efficiency target.

3.3.4. Cordier Analysis

The high efficiency turbocompressor is one of the key enabling technologies for the turbo-compression cooling system. Having high efficiency turbomachinery is essential to meeting high COP targets. To determine the isentropic efficiency of the turbine and the compressor, a Cordier analysis was performed. The Cordier analysis calculated the specific diameter, specific speed, and actual size and speed of both the turbine and the compressor. After the specific speed and diameter were calculated, the isentropic efficiency of the machine can be found by reading the Cordier maps shown in Figure 3-6. Equations (3.10) and (3.11) were used to calculate the specific speed and specific diameter of the turbine and compressor:

$$Ns = \frac{N\sqrt{\dot{V}}}{\left(H_{\mathrm{ad}}\right)^{0.75}} \tag{3.10}$$

$$Ds = \frac{D\left(H_{\mathrm{ad}}\right)^{0.25}}{\sqrt{\dot{V}}} \tag{3.11}$$

where N is the rotation speed of the shaft in revolutions per minute, $\dot{V}$ is the volumetric flow rate in $\mathrm{ft}^3\ \mathrm{s}^{-1}$, H_{ad} is the adiabatic head across the device in ft lbf lbm^{-1}, and D is the diameter of the machine in feet. It is important to note that in typical Cordier analyses, the specific speed, *Ns*, and the specific diameter, *Ds*, are dimensionless, but that is not the case in this work. The specific speed has units of $\mathrm{ft}^{3/4}\ \mathrm{lbm}^{3/4}\ \mathrm{min}^{-1}\ \mathrm{s}^{-1/2}\ \mathrm{lbf}^{-3/4}$. The specific diameter has units of $\mathrm{lbf}^{1/4}\ \mathrm{s}^{1/2}\ \mathrm{lbm}^{-1/4}\ \mathrm{ft}^{-1/4}$. An *Ns-Ds* diagram was produced by Barber Nichols, Inc. to show isentropic efficiencies of typical turbomachinery as a function of dimensional specific speed and specific diameter. The Barber Nichols, Inc. *Ns-Ds* map was used in this work to determine the ideal specific speed and specific diameter to maximize the efficiency of both the turbine and the compressor. The Cordier map is provided as Figure 3-6 for each component. In general, the specific speed of the turbine must be between 50 and 150 while the specific speed of the compressor must be between 60 and 200 for each to have 80% isentropic efficiency. In this work, a specific speed of the turbine was chosen, which set the rotational speed of the shaft from Equation (3.10). From the shaft rotational speed, the specific speed of the compressor could be found. Once the specific speed of the machine is determined, the specific diameter can be calculated from the equation of the line that borders the upper limit of the 80% isentropic efficiency island. The upper bound of the island was used to maximize the physical diameter of the turbomachine. As the device gets physically smaller, the 80% efficiency target becomes increasingly unreasonable. The ratio of the tip clearance and the length of the blades gets larger which increases the inefficiencies of the machine because there is more fluid leaking ‘around’ the blades, between the tip and the hub, instead of turning the blades

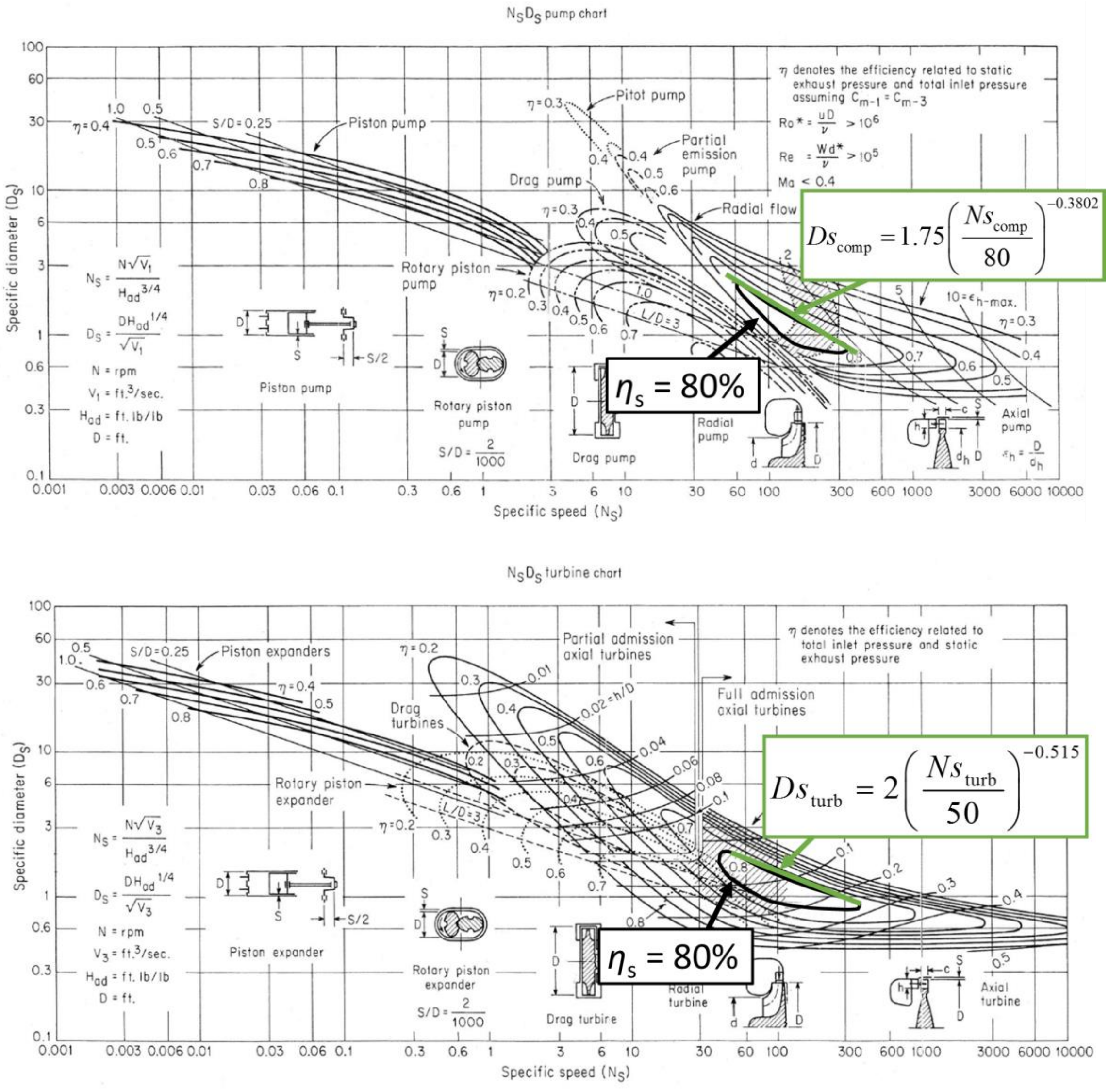

Figure 3-6: Cordier maps for pumping/compressing machines (top) and for expanding machines (bottom).

and producing power. There is a practical lower limit on tip clearance due to material and manufacturing technologies which means that small machines tend to have more losses. Larger machines reach high efficiency targets more easily because the tip clearance losses become smaller. Equations (3.12) and (3.13) determine the specific diameter of the turbine and compressor from the specific speed in the 80% island:

$$Ds_{\text{turb}} = 2\left(\frac{Ns_{\text{turb}}}{50}\right)^{-0.515} \tag{3.12}$$

$$Ds_{\text{comp}} = 1.75\left(\frac{Ns_{\text{comp}}}{80}\right)^{-0.3802} \tag{3.13}$$

The above equations are solved simultaneously in Engineering Equation Solver. This completes the thermodynamic modeling block. The heat exchanger block of the simulation will be explained in detail in the next section.

3.4. Plate and Frame Heat Exchanger Modeling

The present study modeled compact, liquid coupled plate frame heat exchangers for the condensers, boiler, and chiller. The construction a counter flow plate heat exchanger in shown in

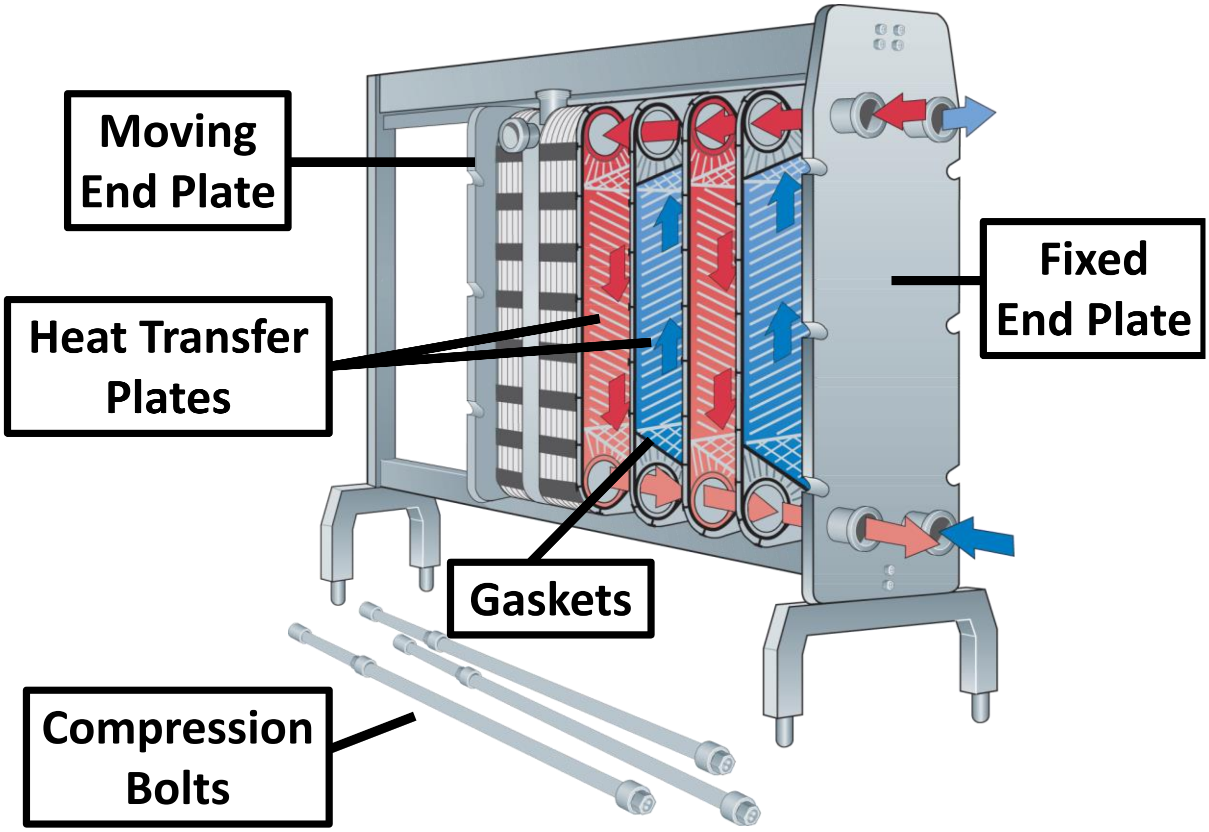

Figure 3-7: Plate heat exchanger construction [104].

Figure 3-7. Plate heat exchangers are made up of a heat transfer plate pack, gaskets, a fixed end plate, a moving end plate, long bolts that span the length of the plate pack, and a frame. The heat transfer plate pack consists of thin plates (~0.0003 m – 0.0007 m) that are separated by gaskets. After the plates and gaskets are compressed between the two end plates using the long bolts, alternating channels for the hot and cold heat transfer fluids are formed, shown in red and blue on Figure 3-7 [104]. The gaskets are used to keep the fluids in their respective flow channels. The channel spacing between the plates is typically on the order of 0.005 m. As shown in Figure 3-7, the fluids enter the device in the inlet header and are distributed to each alternating flow channel. Then, the fluid will flow up or down the plates and recollect in the return header to exit the device. The plates typically have corrugated herringbone patterns to increase heat transfer surface area and induce additional turbulence to improve heat transfer performance.

Plate frame heat exchangers have a number of advantages for this application of the turbo-compression cooling system: small footprint, ease of scalability, and flexibility. Plate frame heat exchangers are compact which is essential as extra space is not readily available onboard large cargo ships. Furthermore, the heat duty of the plate frame heat exchangers can be easily modified by adding or subtracting plates. In addition, the plates and gasket seals can be manufactured out of various materials based on user needs. For example, the condenser plates in this system are titanium to prevent corrosion from seawater exposure and the boiler and chiller plates are stainless steel. If a high pressure is required for the device, then gasket selection can improve the pressure rating. The boiler and condensers are in a counter flow arrangement, while the chiller is a parallel flow heat exchanger. The channel geometry of the plates can also be tailored specifically for boiling or condensation to improve the performance of the device. Plate heat exchangers are an ideal choice for a turbo-compression cooling system that requires a small footprint while maintaining a high performance standard. Each of these enhancements (titanium plates, higher pressure rating, etc.) has an associated cost which is addressed in this work. The details of the heat exchanger design calculations will be provided next.

3.4.1. Epsilon-NTU Heat Exchanger Method

The goal of the heat transfer modeling is to calculate how much heat exchange area is required to achieve the necessary heat duty based on the heat exchanger effectivenesses, calculated mass flows, and temperature differences from the thermodynamic model. The heat transfer modeling also calculated the pressure drop through the heat exchangers and through the system piping.

Figure 3-8 provides a schematic of a single plate in each of the heat exchangers in the TCCS. As discussed above, the plates are connected in parallel with a gasket between each plate. The gasket is depicted in gray, keeping the external water and refrigerant streams separate. The condensers and boiler were modeled as counter flow devices. The chiller was modeled as parallel

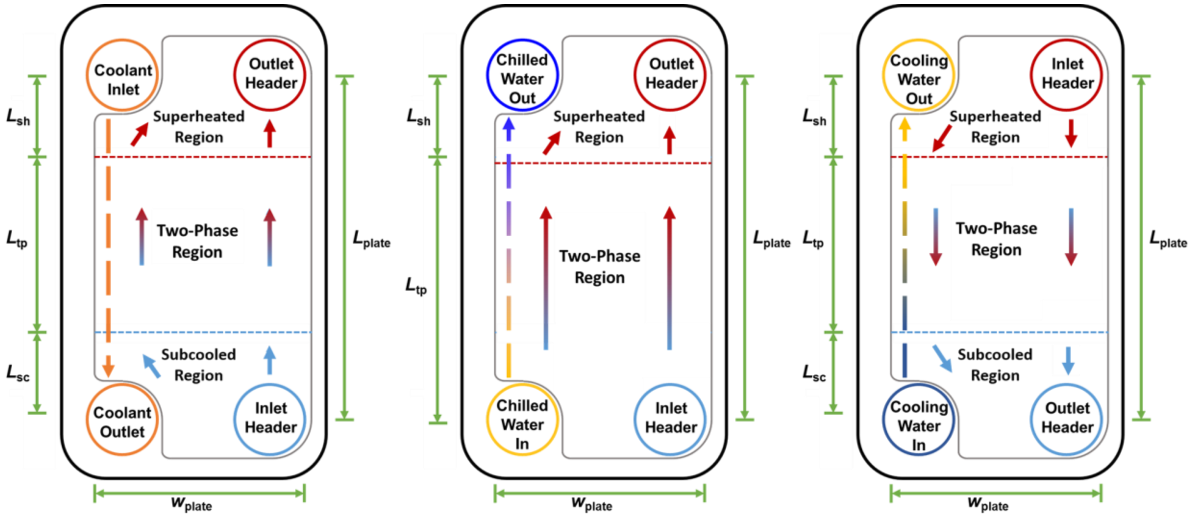

(a) Boiler **(b) Chiller** **(c) Condenser**

Figure 3-8: Flow path and working fluid regions for a single plate in the (a) power cycle boiler (b) cooling cycle chiller and (c) power and cooling cycle condensers.

flow. Compressing the plates creates the refrigerant channels between every second plate and the water channels in the other plates. Each working fluid phase occupies a certain area of every refrigerant plate. As shown in Figure 3-8a, the refrigerant enters the boiler at the bottom header as subcooled liquid and is heated by the hot engine coolant. As it travels upward along the plate, energy is transferred to the working fluid until it becomes a superheated vapor and then exits the heat exchanger through the top manifold. The engine coolant enters in the top header and travels down its respective plates as it heats the refrigerant. In the chiller plates, shown in Figure 3-8b, refrigerant enters at the bottom header of the device as a two-phase mixture and is heated by the external chilled water stream. The refrigerant exits the chiller as a superheated vapor. Since the chiller was modeled as a parallel flow device, the chilled water stream also enters in its respective bottom header and is chilled as it travels upwards along its plate channels. In the power and cooling condenser plates, shown in Figure 3-8c, the refrigerant enters the device as a superheated vapor in the top header. The refrigerant is cooled and condensed to the liquid phase as it travels down the plates to the return header at the bottom of the device. The cooling water stream enters the bottom header and absorbs heat from the refrigerant as it travels upward to the return header.

The epsilon-NTU method was used to calculate the total heat transfer area of each region (subcooled, two-phase, and superheated) of the heat exchangers. The boiler and condensers were counter flow devices, while the chiller was a parallel flow device. The relationship between the effectiveness of a counterflow heat exchanger and the number of transfer units (*NTU*) is given by Equation (3.14):

$$NTU = \frac{1}{Cr-1}\ln\left(\frac{\varepsilon-1}{\varepsilon Cr-1}\right) \tag{3.14}$$

where $C_{\text{ratio}} = C_{\text{min}}/C_{\text{max}}$ is the ratio of heat capacity rates. The relationship from Equation (3.14) was used for the boiler and the condensers. For a parallel flow device, the relationship between effectiveness and number of transfer units is defined in Equation (3.15):

$$NTU = -\frac{\ln\left[1-\varepsilon\left(1+Cr\right)\right]}{1+Cr} \tag{3.15}$$

Equation (3.15) was used to model the chiller. From the overall heat transfer coefficient and the number of transfer units (*NTU*), the heat exchange area is calculated according to Equation (3.16):

$$NTU_{\text{region}} = \frac{U_{\text{region}} A_{\text{region}}}{C_{\text{min}}} \tag{3.16}$$

where U is the overall heat transfer coefficient, A_{region} is the heat exchange area of the distinct regions (subcooled, two-phase, and superheated), and C_{min} is the minimum heat capacity rate. Equations (3.14) - (3.16) were used to calculate the heat exchange area in every region of all the heat exchangers.

The sum of the areas of the specific heat exchanger regions is the total heat exchange area required, as shown in Equation (3.17):

$$A_{\text{total}} = A_{\text{sc}} + A_{\text{tp}} + A_{\text{sh}} \tag{3.17}$$

Once the total heat exchange area was calculated, the number of plates required for the heat exchanger was calculated according to Equation (3.18):

$$A_{\text{total}} = A_{\text{plate}}\left(N_{\text{plate}} - 1\right) = w_{\text{plate}}\left(L_{\text{sc}} + L_{\text{tp}} + L_{\text{sh}}\right)\left(N_{\text{plate}} - 1\right) \tag{3.18}$$

The area enhancements from the corrugation pattern in the plates were not accounted for in the area calculations. The corrugation depth and pitch was not provided from the manufacturer, so the enlargement factor could not be calculated, but the heat transfer and pressure drop correlations accounted for a corrugated herringbone pattern. The reduction in heat transfer surface area from the inlet and outlet headers was accounted for by subtracting a header radius from the appropriate plate regions. The chiller on the cooling cycle does not have a subcooled region area because the working fluid is two-phase at the exit of the expansion valve. Equation (3.18) will approximate the heat transfer area for each heat exchanger which is consistent with the methods in the literature [105].

To calculate the heat transfer area in each region of the heat exchangers, the overall heat transfer coefficient must be calculated. The overall heat transfer coefficient for each region, U, is defined Equation (3.19):

$$\frac{1}{U} = \frac{1}{h_\mathrm{r}} + R_\mathrm{wall} + \frac{1}{h_\mathrm{w}} \tag{3.19}$$

where h_r is the refrigerant side heat transfer coefficient, R_wall is the wall resistance of the plate, and h_w is the water side heat transfer coefficient. R_wall is equal to t_plate / k_plate, where t_plate was determined from plate heat exchanger quotes and data sheets. The geometry specifications of the plates in this study are provided in Table 3-3. With the overall heat transfer coefficient and the *NTU* of each region calculated, the area of each region (subcooled, two-phase, and superheated) could be found using Equation (3.16).

Table 3-3: Plate geometry inputs for the heat exchanger model.

Input	Value	Units
L_plate	1.32	[m]
w_plate	1.17	[m]
t_plate	0.0007	[m]
s_plate	0.0045	[m]
D_header	0.35	[m]
k_titanium	22.1	[W m^{-1} K^{-1}]
$k_\mathrm{stainless}$	13.3	[W m^{-1} K^{-1}]

To understand how the footprint of the TCCS compares to the current shell and tube radiator onboard these ships, the Kern method was used to calculate the size of the engine coolant radiator [106]. The details of the Kern method for shell side heat transfer coefficient can be found in *Process Heat Transfer* from Hewitt et. al.

For this analysis, the same temperature and flow rate inputs were used as the power cycle boiler and condenser. The heat duty was 2 MW, the engine coolant entered at 90°C and exited at 83.9°C with a mass flow rate of 78.5 kg s^{-1}. The seawater entered at 32°C with a flow rate of 250 kg s^{-1}. The effectiveness of this heat exchanger was 0.1045. The seawater flowed on the tube side to facilitate cleaning and maintenance while the engine coolant flowed on the shell side.

The geometric inputs of the shell and tube heat exchanger were chosen with guidance from Hewitt et. al. [106]. The inner diameter of the shell was set to 2.5 m, while the outer diameter of the tubes was 76 mm. The inner diameter of the tubes were 73.3 mm. The tube pitch was 1.3 times the outer diameter of the tubes, resulting in a pitch of 98.8 mm. The length of the tubes was 5.03 m and there were 26 tubes. There were 9 baffles spaced every 0.5 m throughout the length of the shell with a thickness of 5 mm. A representative calculation to determine the size of the shell and tube radiator is provided in Appendix A.4.

3.4.2. Correlations for Heat Transfer Coefficients in Plate and Frame Heat Exchangers

There are a number of correlations for heat transfer coefficients available in the open literature for both condensation and boiling of refrigerants in plate frame heat exchangers. In addition, typical correlations for single phase heat transfer of refrigerants in plate heat exchangers were used. The two-phase and single phase correlations for heat transfer will be discussed in detail in this section. A summary of the correlations used for each heat exchanger and the regions is provided in Table 3-4.

The Kuo correlation for condensation in compact plate frame heat exchangers is represented in Equation (3.20) [107]:

$$h_{\mathrm{r,cond}} = h_{\mathrm{r,l}}\left[0.25Co^{-0.45}Fr_{\mathrm{l}}^{0.25} + 75Bo^{0.75}\right] \tag{3.20}$$

where $h_{\mathrm{r,l}}$ is the single phase heat transfer coefficient for liquid refrigerant in a plate heat exchanger, Co is the convection number, Fr_{l} is the Froude number, and Bo is the boiling number. As shown in Table 4-3, the Kuo correlation was used for the two-phase regions of the refrigerant in the power and cooling cycle condensers. The Kuo correlation was developed for R410a. The single phase liquid heat transfer coefficient is defined according to Equation (3.21):

$$h_{\mathrm{r,l}} = 0.2092\left(\frac{k_{\mathrm{l}}}{D_{\mathrm{hyd,chan}}}\right)\mathrm{Re}_{\mathrm{l}}^{0.78}\,\mathrm{Pr}_{\mathrm{l}}^{1/3}\left(\frac{\mu_{\mathrm{ave}}}{\mu_{\mathrm{wall}}}\right)^{0.14} \tag{3.21}$$

where k_{l} is the thermal conductivity of the liquid phase refrigerant, $D_{\mathrm{hyd,chan}}$ is the hydraulic diameter of the channel, Re_{l} is the liquid Reynolds number, Pr_{l} is the liquid Prandtl number, and μ is the viscosity of the liquid refrigerant. In this case, the ratio of the average and wall viscosities was taken to be unity. The hydraulic diameter is defined and calculated for this plate geometry in Equation (3.22):

$$D_{\mathrm{hyd,chan}} = \frac{4(A_{\mathrm{c}})}{P_{\mathrm{wetted}}} = \frac{4\left(w_{\mathrm{plate}}s_{\mathrm{plate}}\right)}{P_{\mathrm{wetted}}} = 0.008966\ [\mathrm{m}] \tag{3.22}$$

Table 3-4: Summary of heat transfer correlations used for each heat exchanger region.

Heat Exchanger	Fluid Side	Subcooled	Two-Phase	Superheated
Condensers (Power and Cooling Cycle)	Refrigerant	Thonon [107]	Kuo [106]	Thonon
	Seawater	Dittus-Boelter [109]		
Boiler	Refrigerant	Thonon	Hsieh [108]	Thonon
	Engine Coolant	Dittus-Boelter		
Chiller	Refrigerant	-	Hsieh	Thonon
	Chilled Water	-	Thonon	

where w_{plate} is the width of a single plate, s_{plate} is the spacing between each plate, and P_{wetted} is the wetted perimeter. The values of w_{plate} and s_{plate} are shown in Table 3.3. P_{wetted} is equal to 2 × (w_{plate} + s_{plate}). In the literature, the hydraulic diameter of the plate channels is simplified to 2 × s_{plate} because the width of the plates is much larger than the spacing [107–109]. The simplified hydraulic diameter yields a value of 0.009 m for the plate dimensions in this study. When comparing the results for the reduced hydraulic diameter and the actual hydraulic diameter, the payback period of the system was only changed by 0.3%. The dimensionless numbers used in the Kuo Correlation are given as Equations (3.23) through (3.27):

$$Re_{\text{l}} = \frac{uL}{\nu} = \frac{4\dot{m}_{\text{plate}}}{P\mu_{\text{l}}} \tag{3.23}$$

$$Pr_{\text{l}} = \frac{\mu_{\text{l}} c_{\text{l}}}{k_{\text{l}}} \tag{3.24}$$

$$Co = \frac{\rho_{\text{g}}}{\rho_{\text{l}}}\left[\frac{1-x}{x}\right]^{0.8} \tag{3.25}$$

$$Fr_{\text{l}} = \frac{G_{\text{plate}}^2}{\rho_{\text{l}}^2 g D_{\text{hyd,chan}}} \tag{3.26}$$

$$Bo = \frac{q}{G_{\text{plate}} i_{\text{fg}}} \tag{3.27}$$

where c_{l} is the liquid specific heat capacity, x is the quality, G is the refrigerant mass flux, g is the acceleration due to gravity, and i_{fg} is the refrigerant enthalpy of vaporization. The term $\dot{m}_{\text{plate}}$ is defined in Equation (3.28):

$$\dot{m}_{\text{plate}} = \frac{\dot{m}_{\text{r}}}{0.5\left(N_{\text{plate}} - 1\right)} \tag{3.28}$$

where N_{plate} is the number of plates. The term in the denominator of Equation (3.28) represents the number of channels where either working fluid or water is flowing. In the same vein, refrigerant mass flux, G_{plate}, is defined in Equation (3.29):

$$G_{\text{plate}} = \frac{\dot{m}_{\text{plate}}}{s_{\text{plate}} w_{\text{plate}}} \tag{3.29}$$

where s_{plate} is the spacing between plates and w_{plate} is the width of the plate.

The Hsieh correlation for boiling R410a in a vertical plate heat exchanger is presented in Equation (3.30) [109]:

$$h_{\text{r,boil}} = h_{\text{r,l}} \left(88 Bo^{0.5} \right) \tag{3.30}$$

As shown in Table 3-4, the Hsieh correlation was used for the two-phase regions of the refrigerant in the boiler and the chiller.

For the single phase regions of the refrigerant side of all the heat exchangers, the Thonon correlation was used, as shown in Table 3-4. In addition, the Thonon correlation was also used for the water side of the chiller because the Reynolds number was typically around 900, which means that the flow was probably not turbulent. The Thonon correlation is defined in Equation (3.31) [108]:

$$h = 0.2998 Re_{\text{plate}}^{0.645} Pr^{1/3} \frac{k}{D_{\text{hyd,chan}}} \tag{3.31}$$

The Reynolds number range for the Thonon correlation is $50 < Re < 15{,}000$.

The Dittus-Boelter correlation was used for the water side (engine coolant and seawater, heat transfer coefficient on the boiler and condensers, as shown in Table 3-4. The Dittus-Boelter correlation was valid for the water sides of these heat exchangers because the flows were highly turbulent and single phase [110]. For R134a, as shown in Appendix A, the Reynolds number for the power and cooling condensers were 5,000 and 15,000, respectively. Those Reynolds number imply turbulent flows, especially in plate heat exchangers. Since the Reynolds number of the water side of the chiller was around 900, the Dittus-Boelter correlation was not used. The Dittus-Boelter correlation is defined according to Equation (3.32):

$$h = 0.023 Re_{\mathrm{plate}}^{0.8} Pr^{\mathrm{n}} \frac{k_{\mathrm{l}}}{D_{\mathrm{hyd,chan}}} \tag{3.32}$$

where n = 0.3 for cooling and 0.4 for heating. For example, n = 0.3 was used for the boiler water stream because the water side was cooling as it traveled through the heat exchanger. In the condenser, n = 0.4 because it was heating as it traveled through the heat exchanger. The calculation procedure for the heat transfer coefficients for all regions of the heat exchangers has been outlined here. The details of the pressure drop calculations will be presented next.

3.4.3. Pressure Drop in Plate and Frame Heat Exchangers

Figure 3-9 shows a schematic of the refrigerant flow path in the power cycle boiler. The fluid enters as a subcooled liquid in the bottom manifold. The fluid is equally distributed to the channels along the length of the header. Then, the refrigerant is heated by hot engine coolant flowing counter in the second set of channels, represented as orange arrows in the figure. The fluid is vaporized and recombines in the top manifold as it exits the device.

The pressure drop through the heat exchanger was calculated to be the sum of the pressure losses in the single phase and two-phase regions, as shown in Equation (3.33):

$$\Delta P_{\mathrm{HX}} = \Delta P_{\mathrm{sp}} + \Delta P_{\mathrm{tp}} \tag{3.33}$$

In the two-phase region of the heat exchanger, Equation (3.34) was used to calculate pressure drop:

$$\Delta P_{\mathrm{tp}} = \frac{2 f_{\mathrm{tp}} G^2}{\rho} \frac{L_{\mathrm{tp}}}{D_{\mathrm{h,channel}}} \tag{3.34}$$

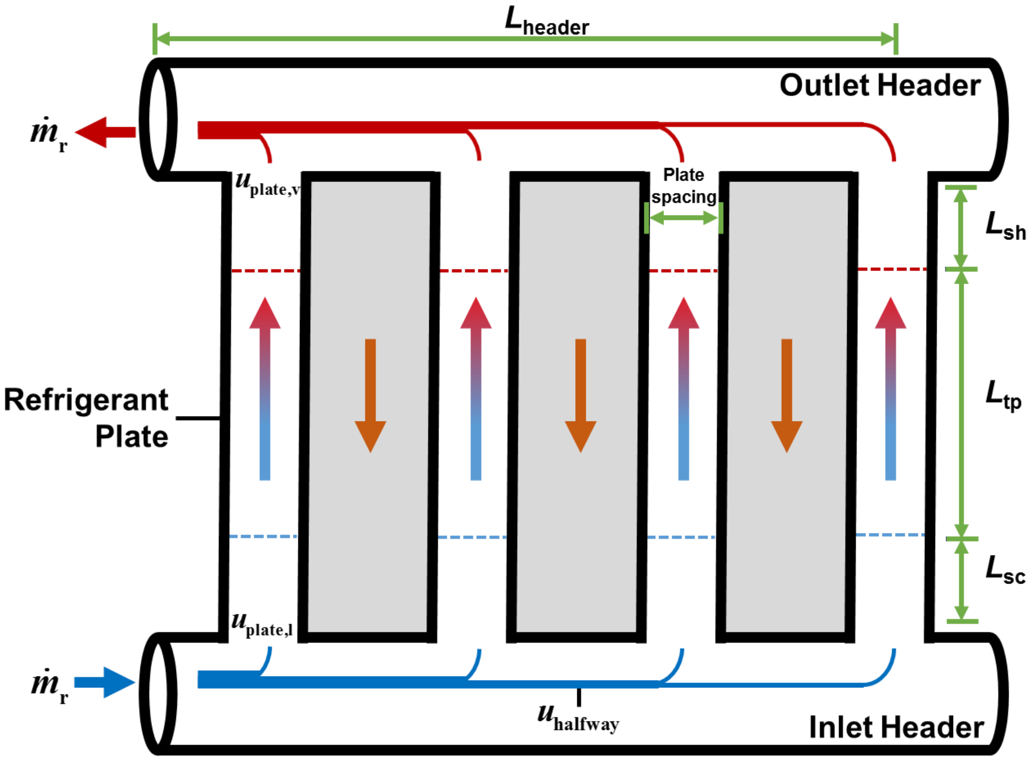

Figure 3-9: Cross section of the flow path in the power cycle boiler. The gray regions represent flow area of hot engine coolant.

where f_{tp} is the two-phase friction factor, G^2 is the mass flux, L_{tp} is the vertical length of the two-phase region, and $D_{h,channel}$ is the hydraulic diameter of the channel. The length of the working fluid region in the plate channels is defined in Equation (3.35):

$$L_{region} = \frac{A_{region}}{\left(N_{plates} - 1\right) w_{plate}} \tag{3.35}$$

The friction factor in the two-phase regions was calculated using the Hsieh and Kuo correlations [107,109]. The Hsieh friction factor for a boiling refrigerant in a vertical plate heat exchanger is given as Equation (3.36):

$$f_{tp,boil} = 61000 Re_{eq}^{-1.25} \tag{3.36}$$

where Re_{eq} is the equivalent Reynolds number. The Kuo friction factor for a condensing refrigerant in a vertical plate heat exchanger is given as Equation (3.37):

$$f_{\text{tp,cond}} = 21500 Re_{eq}^{-1.14} Bo^{-0.085} \tag{3.37}$$

The equivalent Reynolds number is defined in Equation (3.38):

$$Re_{\text{eq}} = \frac{G_{\text{eq}} D_{\text{hyd}}}{\mu_{\text{l}}} \tag{3.38}$$

where G_{eq} is the equivalent mass flux. The equivalent mass flux is defined as Equation (3.39):

$$G_{\text{eq}} = G_{\text{plate}} \left[\left(1 - x_{\text{m}}\right) + x_{\text{m}} \left(\frac{\rho_{\text{l}}}{\rho_{\text{g}}} \right)^{1/2} \right] \tag{3.39}$$

where x_{m} is the mean quality through the heat exchanger region. The pressure drop in the single phase regions of the heat exchangers was modeled as the sum of the pressure drop through the headers, from the flow leaving the headers and entering the plate channels, and through the heat exchanger plates, as shown in Equation (3.40):

$$\Delta P_{\text{sp}} = \Delta P_{\text{header}} + \Delta P_{\text{tee}} + \Delta P_{\text{channel}} \tag{3.40}$$

The pressure drop analysis was simplified by assuming the flow is equally distributed so that each heat exchanger channel has an equal mass flow rate. This flow rate was determined by dividing the refrigerant mass flow rate by the number of working fluid channels in the heat exchanger. The pressure drop through the heat exchanger headers is defined in Equation (3.41):

$$\Delta P_{\text{header}} = K_{\text{tee,line}} \frac{\rho u_{\text{halfway}}^2}{2} + 2 f_{\text{Fanning}} \frac{\rho u_{\text{halfway}}^2 L_{\text{header}}}{D_{\text{header}}} \tag{3.41}$$

where u is the velocity of the working fluid in the header, $K_{\text{tee,line}}$ is the minor loss coefficient from a 90 degree tee measured in the straight line of pipe (equal to 0.9), and f_{Fanning} is the Fanning friction factor [111]. The velocity at each point along the length of the manifold is not constant because flow is branching into and out of the headers. Thus, the pressure drop is not constant throughout the manifold. To simplify this calculation, the velocity at the halfway point of the manifold was used to approximate the pressure drop through the manifold. At the halfway point, half of the total mass flow has entered the plate channels. The calculations in Appendix A for the pressure drop of R134a in the power cycle boiler show that the sum of the inlet and return header pressure drop was 1% of the total pressure drop through the heat exchanger. The sum of the inlet and return header pressure drops was 8.5 Pa, while the total pressure drop through the boiler was 769 Pa. The Fanning friction factor through the headers of the heat exchangers is defined in Equation (3.42) and (3.43):

$$f_{\text{Fanning}} = \frac{16}{Re} \qquad Re \leq 2300 \tag{3.42}$$

or

$$f_{\text{Fanning}} = \frac{0.316Re^{-0.25}}{4} \qquad Re > 2300 \tag{3.43}$$

where Re is the Reynolds number in the header.

The pressure drop through the inlet header to the channel was calculated using Equation (3.44):

$$\Delta P_{\text{tee}} = \frac{\left(K_{\text{tee,branch}} + K_{\text{con/exp}}\right)\rho u_{\text{channel}}^{2}}{2} \tag{3.44}$$

where $K_{\text{tee,branch}}$ is the minor loss coefficient from the 90 degree tee measured in the branched line and K_{con} is the minor loss coefficient due to a sudden contraction or expansion. $K_{\text{tee,branch}}$ is equal to 2, while K_{con} and K_{exp} are defined in Equations (3.45) and (3.46) [112]:

$$K_{\text{con}} = 0.5\left(1 - \frac{A_{\text{c}}}{A_{\text{c,header}}}\right) = 0.473 \tag{3.45}$$

$$K_{\text{exp}} = \left(1 - \frac{A_{\text{c}}}{A_{\text{c,header}}}\right)^{2} = 0.8935 \tag{3.46}$$

The refrigerant velocity in the channels was calculated according to Equation (3.47):

$$u_{\text{channel}} = \frac{\dot{m}_{\text{r}}}{0.5N_{\text{plates}}} \frac{1}{\rho A_{\text{c}}} \tag{3.47}$$

The pressure drop in the single phase heat exchanger channels was modeled according to Equation (3.48):

$$\Delta P_{\text{channel}} = \frac{2 f_{\text{Thonon}} \rho u_{\text{channel}}^2 L_{\text{sp}}}{D_{\text{h,channel}}} \tag{3.48}$$

where L_{sp} is the length of the single phase region (subcooled or superheated) as shown in Figure 3-7. The Thonon friction factor is defined in Equation (3.49):

$$f_{\text{Thonon}} = 0.6857\left(Re\right)^{-0.172} \tag{3.49}$$

The sum of the single phase pressure drops (header and channels) was multiple orders of magnitude smaller than the pressure drop in the two-phase regions. which confirms the assumption that the flow was well distributed [112]. For example, the total pressure drop of the power cycle boiler with R134a was 768.8 Pa, with the single phase regions accounting for 57.3 Pa of the total (7.5% of the total). Appendix A provides a representative calculation of the heat transfer and pressure drop calculations for the boiler power cycle.

The pressure drop through each run of piping was set to 1 kPa and the length of each pipe run was set. The diameter of each piping run was calculated by setting the length and pressure drop through each section of pipe. The length of each pipe was estimated based on guidance from solid modeling efforts of a liquid coupled turbo-compression cooling system and physical construction of an air coupled system. The piping lengths are provided in Table 3-5. In all simulations, the diameter of the pipe was less than 6 inches. The hydraulic diameter required for the single phase regions was calculated using Equation (3.50) :

$$\Delta P_{\text{pipe,sp}} = \frac{\rho f_{\text{Fanning}} u_{\text{pipe}}^2}{2} \frac{L_{\text{pipe}}}{D_{\text{h,pipe}}} \tag{3.50}$$

The friction factor for Equation (3.50) was calculated from Equation (3.42) or (3.43).

From the throttle valve to the chiller, the working fluid is two-phase. The homogeneous method was used to calculate the pressure drop through this region. The hydraulic diameter of this pipe run was calculated using Equation (3.51):

$$\Delta P_{\text{pipe,tp}} = \frac{2 f G^2}{\rho_{\text{eq}}} \frac{L_{\text{pipe}}}{D_{\text{h,pipe}}} \tag{3.51}$$

where the friction factor is calculated from Equations (3.42) or (3.43). The equivalent density is defined by Equation (3.52):

$$\rho_{\text{eq}} = x_{\text{m}} \rho_{\text{g}} + \left(1 - x_{\text{m}}\right) \rho_{\text{l}} \tag{3.52}$$

The homogenous method accounts for two-phase flow by assuming a homogeneous mixture of liquid and gas phases based on the quality of the fluid.

The heat transfer model calculated the required heat exchange area for all four heat exchangers, the pressure drop through all four heat exchangers, and the required diameter for all sections of piping. These outputs were coupled to the economic model to determine system-wide costs.

Table 3-5: Pipe lengths for the power and cooling cycles.

	Pipe Run	**Phase**	**Length [m]**
Power Cycle	Pump to Boiler	Liquid	3
	Boiler to Turbine	Vapor	3
	Turbine to Condenser	Vapor	2
	Condenser to Pump	Liquid	2
Cooling Cycle	Compressor to Condenser	Vapor	2
	Condenser to Throttle Valve	Liquid	3
	Throttle Valve to Chiller	Two-Phase	2
	Chiller to Compressor	Vapor	3

3.5. Economic Modeling

The economic model used the outputs from the thermodynamic and heat exchanger model to estimate costs and cost savings of the liquid coupled turbo-compression cooling system. Cost models were used for all the major components of the system: heat exchangers, piping, power cycle pump, turbocompressor, and working fluid. The cost models were modified by the Chemical Engineering Plant Cost Index (CEPCI) for 2016 to accurately represent present-day cost [113]. The final block of the cost model calculated the fuel savings onboard large cargo ships by implementing a turbo-compression cooling system. The turbo-compression cooling system would provide supplemental cooling, which removes load from the vapor compression chillers. Since the vapor compression chillers are typically powered by the onboard diesel generators, this translates to cost savings from reduced fuel consumption. The following sections will present how the cost of the components in the system were calculated and how the payback period was determined.

3.5.1. Component Cost Models

The cost models for the heat exchangers were based on the total heat exchange area. From Brown, the cost of a plate frame heat exchanger is defined in Equation (3.53) [114]:

$$cost_{\mathrm{HX}} = 1713.8\left(A_{\mathrm{total}}\right)^{0.54} F_{\mathrm{mat}} F_{\mathrm{pressure}} F_{\mathrm{gasket}} \frac{CEPCI_{2016}}{CEPCI_{2005}} \tag{3.53}$$

where $cost_{\mathrm{HX}}$ is in dollars, A is the area of the heat exchanger in m^2, F_{mat} is a material cost multiplier, F_{pressure} is a pressure cost multiplier, F_{gasket} is a gasket cost multiplier and CEPCI is the Chemical Engineering Plant Cost Index value for the designated year. CEPCI_{2016} is equal to 541.7 and CEPCI_{2005} is equal to 468 [115,116]. F_{mat} modifies the cost of the heat exchanger based on the plate material. The cost model assumes that stainless steel plates have a material factor equal to one (baseline), while titanium plates have a material factor equal to 1.6. In this application, the seawater condensers on both the power and cooling cycles were assumed to have titanium plates to prevent material degradation due to aqueous corrosion from seawater. The boiler and chiller plates were assumed to be constructed of stainless steel. F_{pressure} is a cost modifier that accounts for a plate and frame heat exchanger operating at elevated pressures. F_{pressure} is set to 1.23 for operating pressures above 1620 kPa and is equal to 1.35 for operating pressures above 2551 kPa. F_{gasket} is a cost multiplier based on the gasket material used in the plate frame heat exchanger. Nitrile gaskets impose a cost factor of one, Ethylene propylene diene monomer (EPDM) gaskets have a cost multiplier equal to 1.4, and Viton gaskets have a cost multiplier of 2.6. The choice of gasket will depend on the working fluid due to material compatibility. In this work, Nitrile gaskets were compatible with all working fluids.

The cost model for the steel system piping from Brown is defined in Equation (3.54) [114]:

$$cost_{\text{pipe}} = 10\left(0.1N_{\text{fittings}} + 0.924\right)D_{\text{pipe}}^{0.83}L_{\text{pipe}}\frac{CEPCI_{2016}}{CEPCI_{2005}} \tag{3.54}$$

where $cost_{\text{pipe}}$ is in thousands of dollars, N_{fittings} is the number of fittings per 30 meters of pipe (equal to 16.67 in this work), D_{pipe} is the diameter of the pipe run, and L_{pipe} is the length of pipe run. Guidance from physical construction of the air coupled turbo-compression cooling system assisted in the estimation of one fitting per six feet of pipe. The diameter of the pipe was calculated from the heat transfer modeling section by setting a pressure drop and pipe length to solve relevant equations. The piping of the external streams (engine coolant, seawater, and chilled water) was not accounted for in this work because they are not considered to be intrinsic costs of the turbo-compression cooling system. On average, the piping and fittings accounted for 2% of the total system cost.

The power cycle pump cost model was adopted from Couper et. al. and is defined in Equation (3.55) [117]:

$$cost_{\text{pump}} = F_{\text{type}} cost_{\text{base}} \frac{CEPCI_{2016}}{CEPCI_{1985}} \tag{3.55}$$

where $cost_{\text{pump}}$ is the pump cost in dollars, F_{type} is a pump type cost multiplier, and $cost_{\text{base}}$ is the base cost of the machine. $CEPCI_{1985}$ is equal to 325. F_{type} is defined in Equation (3.56):

$$F_{\text{type}} = \exp\left(b_1 + b_2 \ln\left(\dot{V}\sqrt{H}\right) - b_3 \left(\ln\left(\dot{V}\sqrt{H}\right)\right)^2 \right) \tag{3.56}$$

where b_1, b_2, and b_3 are constants that depend on the type of pump, $\dot{V}$ is in gallons per minute and H is head delivered by the pump in feet. In this analysis, the pump was a single stage centrifugal machine rotating at 3550 RPM which defines b_1, b_2, and b_3 to be 0.0632, 0.2744, and -0.0253, respectively. The term $cost_{\text{base}}$ is the base cost, in dollars, of a centrifugal pump constructed of cast iron as defined in Equation (3.57):

$$cost_{\text{base}} = 3.00 \exp\left(8.883 - 0.6019\left(\ln \dot{V}\sqrt{H}\right) + 0.0519\left(\ln \dot{V}\sqrt{H}\right)^2 \right) \tag{3.57}$$

The cost model for the turbocompressor was developed by Barber-Nichols, Inc. as a logarithmic fit of two different design points, 6 kW and 10 kW, of a high efficiency centrifugal turbocompressor [96,118]. The cost model is a function of turbine power and is defined in Equation (3.58):

$$cost_{\text{TC}} = cost_{6kW} \left(\frac{\dot{W}_{\text{actual}}}{6kW} \right)^{\frac{\log\left(\frac{Cost10kW}{Cost6kW}\right)}{\log\left(\frac{10kW}{6kW}\right)}} \tag{3.58}$$

where $cost_{6\text{kW}}$ and $cost_{10\text{kW}}$ are the cost for a 6 and 10 kW turbomachine, and $\dot{W}_{\text{actual}}$ is the turbine work of the device to be priced.

3.5.2. System Refrigerant Charge

The refrigerant charge was estimated by calculating the volume of the heat exchangers and piping and multiplying by an average density across each section to determine the mass. The volume of the plate frame heat exchangers is the sum of the header volume and the volume of the working fluid channels, as shown in Equation (3.59):

$$m_{\text{HX}} = m_{\text{header,i}} + m_{\text{header,o}} + m_{\text{channel}} \tag{3.59}$$

where $m_{\text{header,i}}$ and $m_{\text{header,o}}$ are the mass of refrigerant in the inlet and outlet headers, respectively, and m_{channel} is the refrigerant mass in the working fluid channels. The refrigerant charge in the header is defined in Equation (3.60):

$$m_{\text{header}} = \rho_{\text{header}}\left(\frac{\pi D^2}{4}\right)\cdot L_{\text{header}} \tag{3.60}$$

where ρ_{header} is the density of the working fluid in the header, D is the header diameter and L_{header} is the length of the header. The header diameter was set to 0.350 m, as shown in Table 3-4. The length of the header is given as Equation (3.61):

$$L_{\text{header}} = \left(N_{\text{plates}}\cdot t_{\text{plate}}\right) + s_{\text{plate}}\left(N_{\text{plates}} - 2\right) \tag{3.61}$$

Equation (3.61) is a reasonable approximation of the length of the header, taking into account the thickness of the plates and the spacing between each plate. The number of plates in the spacing term is subtracted by two to account for the two endplates of the heat exchanger. The volume of the working fluid channels was calculated for each region of each heat exchanger, as defined in Equation (3.62):

$$V_{\text{channel}} = V_{\text{ch,sc}} + V_{\text{ch,tp}} + V_{\text{ch,sh}} \tag{3.62}$$

Equation (3.63) represents the volume in the channels in each region of the heat exchanger:

$$V_{\text{ch,region}} = A_{\text{region}}\left(s_{\text{plate}}\right) \tag{3.63}$$

where A_{region} is the total area calculated from the heat exchanger modeling for the subcooled, two-phase, or superheated regions. The density of the working fluid will change significantly during phase change. It was important to account for the density while calculating the refrigerant charge in the heat exchangers, as shown in Equation (3.64):

$$m_{\mathrm{ch,region}} = \rho_{\mathrm{region}} \left(V_{\mathrm{ch,region}} \right) \tag{3.64}$$

where $m_{\mathrm{ch,region}}$ is the mass of working fluid in the specified region and ρ_{region} is the density of the refrigerant in that region. For the two-phase regions, an average density was calculated using the saturated liquid and saturated vapor densities, as shown in Equation (3.65):

$$\rho_{\mathrm{tp}} = 0.5\left(\rho_{\mathrm{l}} + \rho_{\mathrm{v}} \right) \tag{3.65}$$

The sum of the refrigerant mass in each region was taken to calculate the total charge in the plate heat exchanger channels.

The refrigerant charge in the piping was calculated according to Equation (3.66):

$$V_{\mathrm{piping}} = \left(\frac{\pi D^2}{4} \right) \times L_{\mathrm{pipe}} \tag{3.66}$$

where D is the diameter of the pipe and L_{pipe} is the length of pipe run. The volume was multiplied by an average density through each section to determine the total mass. Once the total charge in the system was determined, the cost of the refrigerant was calculated with Equation (3.67):

$$cost_{\mathrm{ref,total}} = m_{\mathrm{ref,total}} cost_{\mathrm{ref,specific}} \tag{3.67}$$

where $m_{\mathrm{ref,total}}$ is the total charge of the system and the $cost_{\mathrm{ref,specific}}$ is the specific cost of the refrigerant on a per mass basis.

3.5.3. Simple Payback Period

The cost savings associated with the implementation of a turbo-compression cooling system are a result of displacing load from the vapor compression chillers. The cooling capacity of the turbo-compression cooling system is divided by the typical COP of the vapor compression system to determine how much electrical energy a typical vapor compression chiller would use to provide the same cooling capacity. The power cycle pump work is subtracted from that term to accurately represent the energy required by the vapor compression system. The equation used to calculate the power displaced by the turbo-compression cooling system is defined in Equation (3.68):

$$\dot{W}_{\text{displaced}} = 0.85\left(\frac{\dot{Q}_{\text{chiller}}}{COP_{\text{refrigeration}}} - \dot{W}_{pump} \right) \tag{3.68}$$

The term on the right hand side of Equation (3.68) is multiplied by 0.85 to represent a cargo ship that is cold ironing 15% of the time. When a large cargo ship is cold ironing, the ship is docked and receiving power from the shore. The vessel can turn off its engines to reduce fuel consumption and emissions. The power displaced is divided by the efficiency of the diesel engine-generator interface to determine the required power output from the engine, shown in Equation (3.69):

$$\dot{W}_{\text{engine}} = \frac{\dot{W}_{\text{displaced}}}{\eta_{\text{generator}}} \tag{3.69}$$

where $\dot{W}_{\text{engine}}$ is the power output of the engine and $\eta_{\text{generator}}$ is the mechanical efficiency of the engine-generator interface. Then, the heat input to the engine is calculated by dividing the engine power output by the thermal efficiency of the diesel engine, as defined in Equation (3.70):

$$\dot{Q}_{\text{in}} = \frac{\dot{W}_{\text{engine}}}{\eta_{\text{thermal}}} \tag{3.70}$$

The diesel engines onboard cargo ships for this application can be run with Heavy Fuel Oil (HFO), Marine Diesel Oil (MDO), or Marine Gas Oil (MGO). Due to more stringent emissions regulations imposed in 2015, Heavy Fuel Oil is being phased out of use [119]. As such, this analysis assumes Marine Gas Oil to be the fuel for the onboard diesel engines. The fuel input to the engine is calculated according to Equation (3.71):

$$\dot{m}_{\text{fuel}} = \frac{\dot{Q}_{\text{in}}}{Q_{\text{MGO,ave}}} \tag{3.71}$$

where $Q_{\text{MGO,ave}}$ is the lower heating value for Marine Gas Oil, equal to 42.8 MJ kg^{-1} [120]. The amount of fuel saved is calculated on an annual basis and multiplied by the cost per unit mass of MGO, \$0.534 per kg, to determine annual cost saving [121]. The simple payback period is the total cost of the turbo-compression cooling system divided by the annual cost savings, as shown in Equation (3.72):

$$\text{Payback Period} = \frac{cost_{\text{HX}} + cost_{\text{pipe}} + cost_{\text{pump}} + cost_{\text{TC}} + cost_{\text{ref,total}}}{\dot{m}_{\text{fuel,annual}} cost_{\text{MGO,specific}}} \tag{3.72}$$

In addition to the payback period, the reduction of CO_2 emissions was calculated using the reduction in fuel saving. Marine Gas Oil emits 3.179 kg of CO_2 per kg of MGO burned [122]. Thus, the CO_2 reduction is defined in Equation (3.73):

$$m_{\text{CO}_2} = 3.179 \cdot \dot{m}_{\text{MGO,annual}} \tag{3.73}$$

The amount of savings from reducing emissions and improving fuel economy are not accounted for in this work.

3.5.4. Discounted Cash Flow Rate of Return

In addition to the simple payback period, the discounted cash flow rate of return (DCFROR) was examined. The DCFROR analyzes cash flows throughout the life time of the turbo-compression cooling system, taking into account the time value of money, along with operating costs throughout the lifetime of the equipment. The turbo-compression cooling system and a traditional vapor compression system were compared using the DCFROR for use onboard a marine vessel. In this analysis, it was assumed the turbo-compression cooling system was retrofitted on the marine vessel, while the vapor compression system was on the ship as a new build. The analysis was performed in this way because the vapor compression system is the standard method of providing refrigeration and space cooling to all large marine vessels. The goal of the DCFROR is to calculate the minimum cost of the cooling energy provided by each system to yield a net present value (*NPV*) of $0, which represents the breakeven point with the specified internal rate of return. The cost per kWh of cooling was compared between the two cooling technologies.

The cost of the vapor compression system was $120 per kW_{th} of cooling capacity. $120 per kW_{th} for a large vapor compression system such as this a conservative estimate. It would likely cost significantly more than this due to limited vendors for a machine at this size. A conservative estimate was chosen to compare the economic performance of the TCCS and an extremely cheap vapor compression chiller. The cooling capacity of the vapor compression system was set to the average of the cooling capacities of the five different turbo-compression cooling systems, 680 kW_{th}. Since the vapor compression system requires electricity input, the cost of a diesel generator was also incorporated into the capital cost. The cost of the diesel generator was $350 per kW_e of generation capacity, where the generation capacity was 170 kW_e. 170 kW_e is the marginal engine size required to produce about 680 kW_{th} of cooling with state-of-the-art vapor compression chillers. Even though the turbo-compression cooling system requires the waste heat from the diesel generators, the cost of the diesel generator was not incorporated into the turbo-compression cooling system DCFROR analysis. Since the turbo-compression cooling system is a retrofit, the onboard diesel generators are already purchased and are considered a sunk cost. In addition, the DCFROR was conducted for a standard vapor compression system of this size without including the cost of the diesel genset in an effort to strictly compare the costs between the cooling technologies. This ‘apples to apples’ comparison will be helpful to an end user trying to decide whether to implement a relatively new/risky technology in the turbo-compression cooling system or to install a standard vapor compression system, where the costs of operation are higher but the potential risk is lower.

The constant inputs for the DCFROR are shown in Table 3-6, which were chosen in accordance with the 'nth' plant design considerations [123]. The lifetime of the systems was 30 years. The internal rate of return was chosen to be 10% for the turbo-compression cooling system, since it is a relatively new technology representing some risk. The internal rate of the return for the vapor compression and diesel generator was chosen to be 2% because the technology is well understood and the risk is lower. Both systems were assumed to be built over a 3-year period with a startup time of 6 months. The startup time implies that the system only provides 50% of the total cooling capacity for the first 6 months of operation as the system is commissioned and troubleshooting is performed. The maintenance cost of each system was chosen to be 3% of the total capital cost for each year of operation. The systems operated for 7884 hours, representing 90% of one full year. The loan period for each system was 10 years and the loan interest rate was 8.0%, where payments were made yearly. The loan principal was 40% of the total equipment and facilities capital cost. The depreciation schedule was over 7 years in a modified accelerated cost recovery system, which is the current tax depreciation schedule in the United States.

The governing equation for the DCFROR analysis is given in Equation (3.74):

$$NPV = NPB - NPC \tag{3.74}$$

where *NPV* is the net present value, *NPB* defines the net present benefits, and *NPC* defines the net present costs. *NPB* and *NPC* are defined according to Equations (3.75) and (3.76):

$$NPB = \frac{1}{\left(1+IRR\right)^{y}} \cdot \sum_{y=1}^{30} \left(\text{Annual Benefit}\right) \tag{3.75}$$

$$NPC = \frac{1}{\left(1+IRR\right)^{y}} \cdot \sum_{y=1}^{30} \left(\text{Annual Cost}\right) \tag{3.76}$$

Table 3-6: Fixed inputs for the discounted cash flow rate of return study.

Fixed Inputs	Value
Cost of VCC	\$120 per $\mathrm{kW_{th}}$
Cost of Diesel Generator Set	\$350 per $\mathrm{kW_e}$
Internal Rate of Return	10%
Construction Period	3 Years
Startup Time	0.5 Years
Maintenance Cost	3% of Capex (yearly)
Operating Time	7884 hours (yearly)
Loan Period	10 Years
Loan Interest Rate	8%
Depreciation Schedule	MACRS (7 Year)

where $1 / (1+IRR)^y$ is the discount factor and y is the year of operation. The terms *NPB* and *NPC* bring future benefits and costs into the present using the discount factor. For example, with an internal rate of return of 10%, in year two of operation the discount factor is 0.93, compared to the discount factor of 0.39 in year ten, showing that the same absolute cash flow is worth less in the future. Money in the present is inherently more valuable because it can be invested, beginning to accrue interest and increase in value. Money that will be acquired ten years in the future cannot be invested right now, which means that it has an intrinsically lower value. Annual Benefit is defined in Equation (3.77):

$$\text{Annual Benefit} = \dot{Q}_{\text{chill}} \cdot t \cdot x_{\text{chill}} \tag{3.77}$$

where $\dot{Q}_{\text{chill}}$ is the amount of cooling capacity the system can provide, t is the number of hours in a year the system operates, and x_{cool} is the minimum selling price of cooling capacity, in dollars per kWh. Again, the analysis calculates the minimum x_{chill} to yield a *NPV* of \$0. Annual Cost is calculated according to Equation (3.78):

$$\text{Annual Cost} = \text{Capex} + \text{Opex} + \text{Loan} \tag{3.78}$$

In addition, a sensitivity analysis was conducted to better understand the impact each input has on the cost of cooling energy provided by the turbo-compression cooling system. The results of the DCFROR comparison for each system and the sensitivity analysis will be provided in Chapter 4. The following section will detail how the turbo-compression cooling system was optimized to minimize the simple payback period.

3.6. Technoeconomic Optimization

The coupled thermodynamic, heat transfer, and economic models as presented in the preceding sections were optimized to minimize the simple payback period of the turbo-compression cooling system applied to a large cargo ship. The optimization routine is a manual search and find method to find the payback period is minimized. There are a number of parameters that could be used to optimize the system: closest approach temperatures, saturation pressures, or heat exchanger effectiveness values. In the present study, the minimum simple payback period was calculated by finding the optimum combination of heat exchanger effectiveness values. The effectiveness of the heat exchanger is directly related to the total heat exchange area. Since heat exchangers are often 75% of the total cost of thermal energy systems, the effectiveness of the heat exchangers was an ideal choice for an optimization parameter. Finding the optimum heat exchanger area is the most important factor in payback period minimization. The effectiveness of each region in the heat exchangers (subcooled, two-phase, and superheated) has a profound effect on the overall system cost.

The first step in the optimization routine is to set the Reynolds number in the superheated regions of the boiler, chiller, and condensers to 15,000. If this Reynolds number is not set, the optimization procedure results in a Reynolds number greater than 15,000, which is out of range for the Thonon correlation. When the Reynolds number is higher than 15,000, the heat transfer coefficients in those regions are artificially high. As a result, the calculated heat exchange area was low which translated into an unrealistic number of plates and unrealistic heat exchanger size. This effect was further compounded because a small number of plates at a fixed mass flow rate translates to a very high Reynolds number and thus a recursive problem is developed. A search was conducted through available literature to better understand Reynolds number ranges for heat transfer coefficient correlations in plate heat exchangers. The Reynolds number rarely surpasses 20,000 for refrigerants flowing through plate heat exchangers [124–128]. It is not immediately clear why this phenomenon occurs, but the flow in plate heat exchangers is highly turbulent even at low Reynolds number. Higher Reynolds numbers could lead to large pressure drops through the plate heat exchangers or could cause erosion of the plates and gaskets.

When the Reynolds numbers in the superheated regions of the plate heat exchangers are set, the model only requires three effectiveness inputs. The effectiveness values that are still input after setting the Reynolds number are: effectiveness of the subcooled region in the power cycle condenser, or PC C_{sc}, the effectiveness of the subcooled region in the cooling cycle condenser, or CC C_{sc}, and finally the effectiveness in the superheated region of the cooling cycle evaporator, or CC E_{sh}. These effectiveness values are varied to determine the optimized solution.

The optimization begins by altering the effectiveness of the subcooled region in the power cycle condenser. The value is altered while noting the effect on the simple payback period. Once an increase or decrease of the subcooled power cycle condenser effectiveness causes an increase in the payback period, then the process is repeated with the final two effectiveness inputs, subcooled cooling cycle condenser and finally superheated cooling cycle evaporator. After all inputs are optimized, then the method is repeated in the same order to ensure that the model converged to the most optimized solution. It was noted that after three iterations of the optimization procedure, changing the effectiveness values did not decrease the payback period and the model was fully optimized to minimize the simple payback period. Other optimization routines are possible, but the manual search and find method was ideal because the model was very sensitive to small changes in effectiveness values. The optimal system results were found with this method.

After the optimization routine, it was important to determine if the turbocompressor still was in the 80% efficiency island. As detailed in Section 3.2.4, the specific speed of the turbine was chosen and then the specific diameter was calculated. From these, the compressor specific speed and diameter were calculated. The specific speed of the turbine must be chosen so that both sides of the machine have high efficiency. If this result is unachievable based on the limits from the Cordier diagram, then different fluids should be used on the power and cooling cycle to simultaneously maximize the efficiency of the turbine and compressor.

A sensitivity study was also performed to determine which effectiveness values had the greatest effect on the payback period. For this portion of the study, the Reynolds numbers in the superheated regions were not set. This allowed more effectiveness inputs to be examined. Each effectiveness was changed by 0.1 and the percent change on payback period was noted.

The turbo-compression cooling system was simulated with five different working fluids to better understand the effect of working fluid on thermodynamic, heat transfer, and economic performance. The methods described in Sections 3.2 to 3.5 were completed for every working fluid. In this analysis, the same working fluid was used on both the cooling and power cycle. Using the same working fluid on both sides reduces the overall complexity of the turbocompressor because the two sides do not require a hermetic seal. The hermetic seal is complex and will decrease the torque transfer efficiency between turbine and compressor. Using the same fluid on both sides is also advantageous because it will decrease the overall system footprint—only one type of working fluid storage cylinder is required. Reducing the overall system size is important as there is a limited amount of available space onboard large cargo ships.

The modeling section of this work is now complete. The technoeconomic modeling of the turbo-compression cooling system was performed for five different working fluids. A representative calculation that steps through each block of the model using R134a is given in Appendix A.

CHAPTER 4. Results of Technoeconomic Optimization and Working Fluid Selection

The optimization method described in detail in Section 3.5 found the minimum simple payback period for five different turbo-compression cooling systems that used different working fluids. Most studies on waste heat recovery systems focus on the energetic or exergetic performance as indicators of value. This work sought to characterize how thermodynamic performance and economic performance are related. In many real world cases, the primary indicator of value of waste heat recovery is the economic performance.

4.1. Thermodynamic Performance

Table 4-1 presents a comparison of the thermodynamic results for all five simulations as a function of the working fluid. Each system shown in Table 4-1 was optimized using the heat exchanger effectivenesses to find a minimum payback period. The state points for each simulation are provided in Appendix B.

The TCCS that used the low GWP refrigerant R1234ze(E) had the highest overall system COP of 0.415. The R1234ze(E) system had the second highest thermal efficiency of the ORC (7.9%) and highest COP of the cooling cycle (5.58) which combined to have the highest overall system COP. The R1234ze(e) system provided 837 kW of cooling capacity with a compressor power of 150 kW. The R134a system had the highest organic Rankine cycle thermal efficiency of 8.1%, with a turbine power output of 161 kW. Using two different working fluids on the power and cooling cycles could simultaneously maximize their efficiency and further improve the overall system COP. For example, using R134a on the power cycle (highest thermal efficiency) and R1234ze(E) on the cooling cycle (highest vapor compression COP) could yield a higher system

Table 4-1: Comparison of each TCCS with different working fluids.

Working Fluid	**System *COP***	$\dot{Q}_{\mathrm{chill}}$	$\dot{W}_{\mathrm{turb}}$	$\dot{W}_{\mathrm{comp}}$	η_{ORC}	COP_{VC}	***TC speed***	D_{turb}	D_{comp}
		[kW]	**[kW]**	**[kW]**	**-**	**-**	**[rpm]**	**[m]**	**[m]**
R134a	0.384	775	161	153	0.081	5.06	27887	0.125	0.164
R152a	0.311	626	133	127	0.066	4.93	33803	0.121	0.149
R245fa	0.269	539	133	126	0.066	4.27	16288	0.212	0.302
R1234ze(E)	0.415	837	158	150	0.079	5.58	23658	0.144	0.194
R600a	0.305	613	129	123	0.064	5.00	30959	0.147	0.185

COP. The speed and size of the turbine and compressor must match when using two different working fluids, which is a consideration that must not be overlooked.

In these simulations, the specific speed of the turbine was set to 115 to compare the size and speed of the turbocompressor for the five working fluids, which are shown in Table 4-1. The R245fa TCCS had the largest turbine and compressor diameter and the slowest rotational speed. The density of R245fa at the turbine and compressor inlets were much lower than the other fluids examined in this study. The low density and high mass flow rate of R245fa drives the volumetric flow rate of the turbocompressor higher. The high volumetric flow rate will increase the diameter of the turbomachine while decreasing the speed, in accordance with the specific speed and diameter equations used in this work, Equations (3.10) and (3.11). Each compressor in this work landed in the island for 80% efficiency in Figure 3-6. As discussed in Chapter 3, larger turbomachinery is advantageous because manufacturing the blades, inlet guide vanes, and housing is easier. In addition, it is easier to reach higher efficiency targets with larger turbines and compressors ($\eta_s > 80\%$). The large size of the turbine could be a factor for the widespread use of R245fa in commercial organic Rankine cycles. In addition, the highly positive slope of the saturated vapor line on the T-s diagram of R245fa is advantageous for ORC operation because an isentropic and adiabatic expansion won't drive the working fluid into the two-phase region. Although the real expansion is non-isentropic, that simply drives the end point of the expansion process further to the right on a T-s diagram, pushing it farther away from the two-phase region. The only time liquid droplets could form during the expansion process is if heat was removed from the working fluid during expansion. As long as the turbine is well-insulated, this will never occur.

The system with R245fa had the worst performance on the cooling cycle in terms of COP and chilling duty. The R245fa power cycle had comparable performance to R152a and slightly better performance than the R600a power cycle. Of the fluids in this study, R245fa had the lowest saturation temperature and pressure which caused the operating pressures throughout both the power and cooling cycle to be the lowest, as shown in Appendix B. Since the operating pressures were so low, the pressure drop through the heat exchangers had a large detrimental effect on the system performance, which will be explained further in Section 4.2. In the R245fa system, the pressure ratio of the compressor was the highest of the fluids examined. As the compression ratio increases in the cooling cycle, the compressor requires more work to appropriately pressurize the working fluid. In addition, it drives the two-phase line of the evaporator on the P-h diagram down towards the x-axis which could decrease the total cooling capacity for a dry working fluid, as

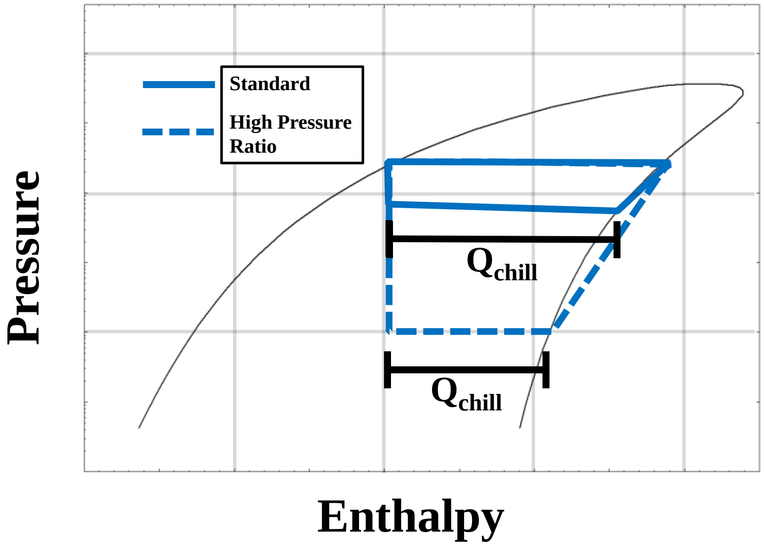

Figure 4-1: Pressure-enthalpy diagrams of a standard vapor compression system with R245fa.

shown in Figure 4-1. For example, the compression ratio on the R245fa system was 5.3 which yielded a vapor compression cycle COP of 4.27 compared to the R1234ze(E) compression ratio of 2.9 and the vapor compression COP of 5.58. These factors contribute to the poor COP of the cooling cycle with R245fa.

The performance turbo-compression cooling system is dependent on the enthalpy of vaporization (i_{fg}) of the fluids. A comparison of the P-h curves of every fluid used in this study is provided in Figure 4-2. The power cycle has the best performance with the fluids that have a low i_{fg} at the boiler saturation pressure. Since the heat input was set in the boiler to 2 MW, a lower enthalpy of vaporization will yield a higher mass flow rate in the power cycle. For example, R134a had an i_{fg} of 104.0 kJ kg^{-1} at the boiler saturation pressure (2700 kPa) and a power cycle mass flow rate of 11.47 kg s^{-1}, which yielded a turbine power of 161 kW. In comparison, the i_{fg} of R600a was

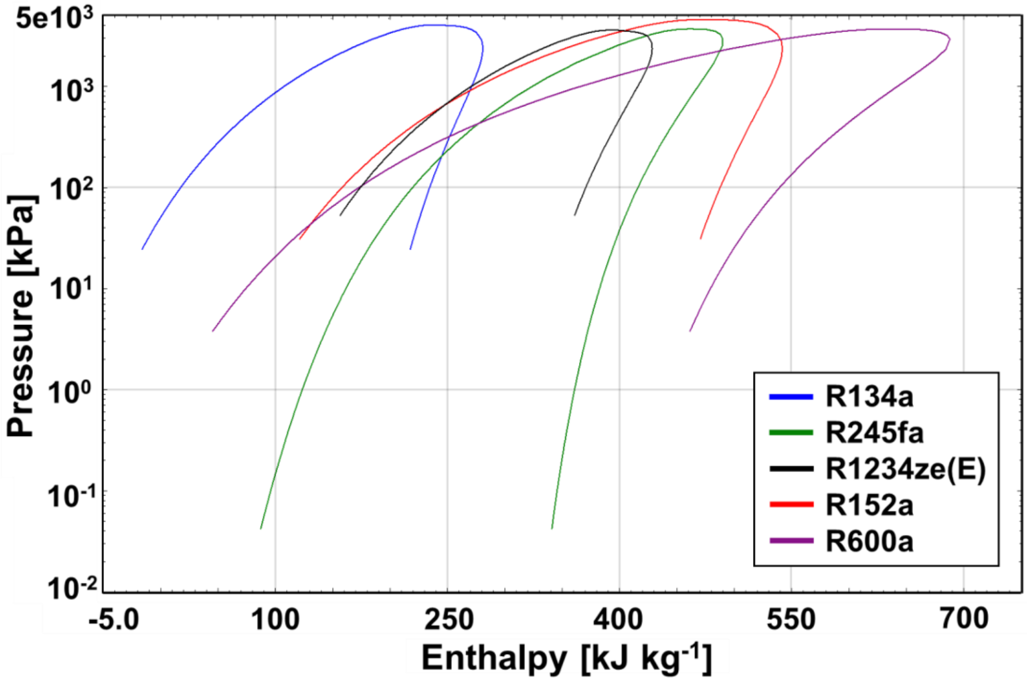

Figure 4-2: Pressure-enthalpy diagrams for all of the working fluids examined in this study.

259.8 kJ kg^{-1} at the boiler saturation pressure (1225 kPa) and a mass flow rate of 5.43 kg s^{-1} to result in a turbine power output of 129 kW. It is interesting to note that although R134a had a lower enthalpy drop across the turbine than R600a (14.1 kJ kg^{-1} compared to 23.8 kJ kg^{-1}), the power output was higher as a result of the higher mass flow rate. The mass flow rate of the refrigerant in the power cycle has a larger impact on the turbine power output than the enthalpy drop.

4.2. Heat Exchanger Design

The simulations were optimized by varying the heat exchanger effectiveness values in the subcooled region of the power and cooling cycle condensers and the superheated region of the cooling cycle evaporator (chiller). With these three inputs and the Reynolds number inputs, the simulation solved for the other effectiveness values in the heat exchanger regions. The optimized values for every plate and frame heat exchanger and working fluid are provided in Tables 4-2 to 4-5, including the effectiveness values, the number of plates, the pressure drop, the thermal conductance (UA), and the cost based on total heat exchange area.

Table 4-2: Characteristics of the boiler (power cycle evaporator) for each working fluid.

Boiler	R134a	R1234ze(E)	R152a	R245fa	R600a
ε: subcooled	0.703	0.772	0.660	0.792	0.718
ε: two-phase	0.420	0.454	0.280	0.389	0.307
ε: superheated	0.406	0.007	0.843	0.345	0.744
# of Plates	162	168	123	178	127
ΔP (kPa)	0.8	0.9	0.8	2.7	1.2
UA (kW K^{-1})	216	231	149	189	158
P_{in} (kPa)	2701	2073	2074	756	1226
T_{sat} (°C)	81	82	74	78	76
CAT (°C)	5	5	11	7	10
Cost	$53,527	$54,623	$34,053	$41,760	$34,720

The optimization routine aimed to increase the amount of superheat at the boiler outlet. Increasing the amount of working fluid superheat will increase the enthalpy at the turbine inlet and yield a higher turbine power output, as shown in Table 4-2. Raising the turbine power output will also increase the input work to the cooling cycle which will increase the cooling duty of the system. Table 4-4 shows that the method also sought to reduce the amount of superheat leaving the chiller to reduce the amount of heat the cooling cycle condensers need to reject to the seawater, reducing their heat exchange area. A majority of the heat duty in the chillers occurs in the two-phase regions, which is why those effectiveness are high. In addition, the amount of subcooling leaving the power cycle condenser was minimized, as seen in Table 4-3, because extra subcooling would eventually have to be overcome in the boiler. Since the heat input was fixed, extra subcooling would reduce the inlet enthalpy to the turbine and decrease power output of the ORC. The lower limit of effectiveness in this study was chosen to be 0.001. In general, the optimization sought to keep the effectiveness values through the condensers low because they were the most expensive components due to their titanium material requirements.

Table 4-3: Characteristics of the power cycle condenser for each working fluid.

PC Condenser	**R134a**	**R1234ze(E)**	**R152a**	**R245fa**	**R600a**
ε: subcooled	0.001	0.001	0.001	0.001	0.001
ε: two-phase	0.174	0.165	0.139	0.122	0.125
ε: superheated	0.104	0.330	0.482	0.525	0.642
# of Plates	205	204	141	202	148
ΔP (kPa)	4.3	4.5	4.3	11.9	5.1
UA (kW K^{-1})	202	193	164	144	151
P_{in} (kPa)	1076	820	1016	300	599
T_{sat} (°C)	43	43	44	45	45
***CAT* (°C)**	10	12	11	14	13
Cost	$72,058	$71,790	$58,737	$71,446	$60,261

The pressure drop in all of the heat exchangers was small enough that it did not have a significant impact on the modeling results, except for the R245fa system. The R245fa heat exchangers had a pressure drop that was almost three times as large as the other working fluids. This could have been due in part to the pressure drop correlations being inaccurate for R245fa because the Hsieh and Kuo correlations were originally designed for R410a. Further, the operating pressures throughout the R245fa cycles were considerably lower than the other systems so the pressure drops were a larger fraction of the total operating pressure compared to the other systems, as seen in Tables 4-2 to 4-5. For example, Table 4-4 shows the inlet pressure to the chiller on the R245fa cycle was 68 kPa and the pressure drop through the chiller was 14.87 kPa, which amounts to an approximately 21% loss of inlet pressure. Comparatively, the R600a system had a chiller inlet pressure of 189 kPa with a pressure drop of 6.86 kPa which amounts to a 4% loss of pressure. The high pressure drop in the R245fa system had a large impact on the results. When the pressure drop is ignored in the heat exchangers of the R245fa system, the overall system COP increases from 0.269 to 0.320. The COP of the vapor compression system shows a large increase from 4.27 to 5.01 while the thermal efficiency of the ORC has a small improvement from 6.6% to 6.7%. The

Table 4-4: Characteristics of the chiller (cooling cycle evaporator) for each working fluid.

Chiller	R134a	R1234ze(E)	R152a	R245fa	R600a
ε: two-phase	0.802	0.803	0.743	0.798	0.765
ε: superheated	0.001	0.085	0.001	0.001	0.001
# of Plates	108	125	63	133	74
ΔP (kPa)	5.7	6.6	5.4	14.9	6.6
UA (kW K^{-1})	251	272	170	172	178
P_{in} (kPa)	359	268	318	68	189
T_{sat} (°C)	6	6	5	3	5
CAT (°C)	2	2	2	6	3
Cost	$31,668	$34,412	$23,511	$35,514	$25,842

vapor compression cycle shows a larger improvement because the pressure drop was a larger fraction of the total operating pressure, as explained above. The payback period of this system decreased by 14% when the pressure drop was ignored. The system with R600a saw minimal improvements when the pressure drop was ignored through the heat exchangers: overall COP increased from 0.305 to 0.317, payback period decreased 3%, the COP of the vapor compression cycle increased from 5.00 to 5.17, and the thermal efficiency of the power cycle increased by 0.4%.

In general, the power cycle heat exchangers were considerably larger than the cooling cycle heat exchangers. From the data presented in Tables 4-2 to 4-5, the average power cycle condenser had 180 plates, while the next largest heat exchanger, the power cycle boiler, had 152 plates. The boiler had a smaller number of plates and heat transfer area than the power condenser in all simulations. The average closest approach temperature (CAT) in the boiler was 7.5°C, while the average closest approach temperature in the power cycle condenser was 11.8°C. The boiler also had a larger heat duty than the condenser (2 MW vs ~1.8 MW). Intuitively, a lower closest approach temperature and larger heat duty would imply a larger heat exchanger, although this was not the case found in this work. The power condenser is always larger than the boiler because the

Table 4-5: Characteristics of the cooling cycle condenser for each working fluid.

CC Condenser	**R134a**	**R1234ze(E)**	**R152a**	**R245fa**	**R600a**
ε: subcooled	0.485	0.560	0.460	0.177	0.426
ε: two-phase	0.074	0.086	0.053	0.053	0.064
ε: superheated	0.467	0.140	0.576	0.267	0.141
# of Plates	90	104	49	74	63
ΔP (kPa)	3.5	4.4	4.0	13.1	5.7
UA (kW K^{-1})	89	103	62	59	73
P_{in} (kPa)	1126	754	1012	281	567
T_{sat} (°C)	43	41	44	43	42
***CAT* (°C)**	11	10	12	12	11
Cost	$45,902	$49,847	$33,013	$41,352	$37,724

two-phase refrigerant heat transfer coefficients were significantly smaller in the condenser compared to the boiler. For example, the condensing heat transfer coefficient for R134a was calculated to be 857 W m^{-2} K^{-1}, while the boiling heat transfer coefficient of R134a was 4561 W m^{-2} K^{-1}. Thus, the overall heat transfer coefficient in the two-phase region of the condenser was 650 W m^{-2} K^{-1} compared 1266 W m^{-2} K^{-1} for the boiler. This was the driving force behind the size differences between the condenser and the boiler on the power cycle.

For the cooling cycle heat exchangers, the chiller was larger than the condenser in all simulations. The results here are consistent with the discussion above. The chiller had a much lower CAT, on average, than the condenser (2.9°C and 11°C, respectively). Although the heat transfer coefficients of the cooling cycle heat exchangers had a similar trend to the power cycle, the end results were different. Similar to the power cycle heat transfer, the two-phase region in the chiller had a refrigerant side heat transfer coefficient of 3336 W m^{-2} K^{-1} and the two-phase region of the condenser had a heat transfer coefficient of 891 W m^{-2} K^{-1}. This drove the overall heat transfer coefficient of the two-phase region in the chiller higher than the two-phase region in the condenser, 1531 W m^{-2} K^{-1} compared to 752 W m^{-2} K^{-1}. Although the chiller heat duty was smaller and the heat transfer coefficient was larger than those of the condenser, the disparity in approach temperature caused the chiller be a larger heat exchanger. The accuracy of these heat transfer coefficient correlations should be considered in future studies. Perhaps correlations designed specifically for each working fluid would yield different results.

The *UA* of the heat exchangers does not always follow the pattern of number of plates. This is due to differences in overall heat transfer coefficients. For example, R245fa boiler had a total *UA* of 189 kW K^{-1}, while requiring 178 plates, as shown in Table 4-2. The R1234ze(E) boiler had a *UA* of 231 kW K^{-1}, but required only 168 plates. Thus, the R1234ze(E) boiler had a higher overall heat transfer coefficient than the R245fa boiler.

The heat exchangers on the R1234ze(E) system were the most expensive, costing a total of \$210,673 while the R152a heat exchangers were the cheapest at \$149,315. The condensers were the most expensive heat exchangers on their respective cycles due to the titanium material requirements to prevent corrosion from the seawater. The cost multiplier from Thane Brown's Engineering Economics increased the cost of titanium plate and frame heat exchangers by a factor of 1.6. If this additional material cost multiplier was removed, the cost of the system is going to decrease, which would allow higher heat exchanger effectivenesses to be tolerated throughout the cycles. The COP would likely increase as a result of more effective heat exchangers. The effects of this cost multiplier will be left to future works. The R245fa boiler was the largest boiler throughout these simulations but it was not the most expensive because the operating pressures were low. When the operating pressure is above 1600 kPa or 2500 kPa, the cost of the plate heat exchanger is increased by 1.23 times or 1.35 times, respectively, according to the Thane Brown cost models.

Table 4-6: Parametric study of each effectiveness input for R134a. The optimized values are highlighted in green.

R134a							
$\varepsilon_{PC,C3}$	**Payback Period**		$\varepsilon_{CC,C3}$	**Payback Period**		$\varepsilon_{CC,E2}$	**Payback Period**
-	[years]		-	[years]		-	[years]
0.001	**1.68**		0.001	1.708		**0.001**	**1.68**
0.219	1.704		0.219	1.691		0.219	1.684
0.485	1.747		**0.485**	**1.68**		0.485	1.693
0.673	1.799		0.673	1.685		0.673	1.705
0.9	2.009		0.9	1.771		0.9	1.755

To confirm the optimized results were found, a parametric study of the effectiveness inputs for R134a is shown in Table 4-6. The optimized effectiveness values are highlighted in green. The minimum effectiveness in this study was 0.001 and the maximum was 0.9, to help ground the system in reality. For the subcooled region of the power cycle condenser, any increase in the effectiveness value from 0.001 increased the payback period. Any change from 0.485 for the subcooled region of the cooling cycle condenser increased the payback period. Finally, any increase from 0.001 for the superheated region of the chiller resulted in a payback period increase.

To understand the footprint impact of implementing a TCCS to recover engine coolant waste heat, the size of an equivalent shell and tube heat exchanger to reject engine coolant heat was determined. The results of this comparison are shown in Figure 4-3. Using the Kern method, the length of the shell and tube heat exchanger was calculated to be 5.03 m with a shell diameter of 2.5 m. Thus, the footprint of this heat exchanger was 12.6 m^2. The footprint of the R134a power cycle boiler and condenser combined was 5.7 m^2, about half that of the shell and tube which demonstrates the advantages of the plate and frame heat exchangers. Removing the shell and tube

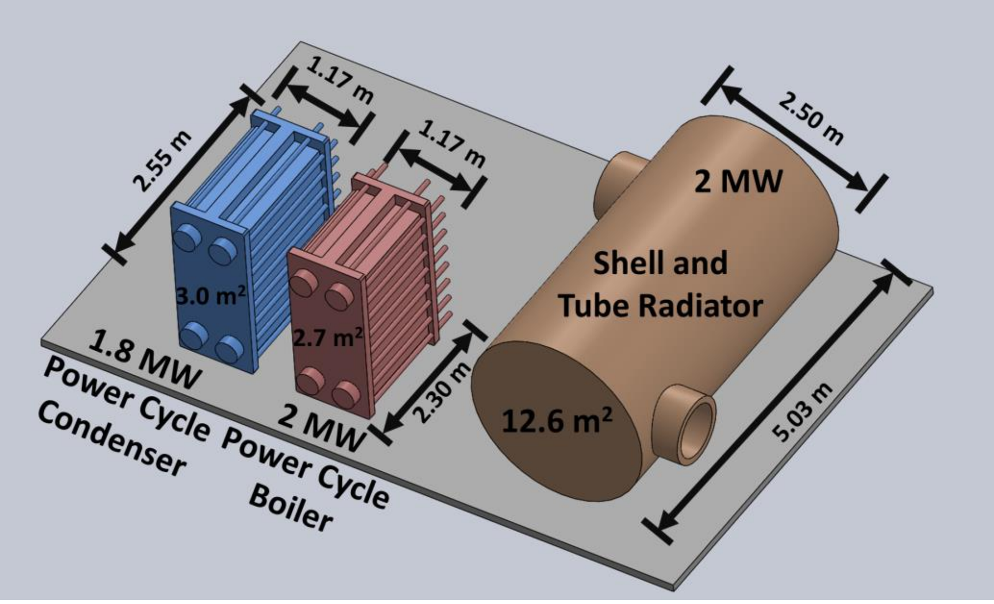

Figure 4-3: Footprint comparison of power cycle heat exchangers and shell and tube radiator.

radiator and replacing it with the TCCS will reduce the overall heat rejection system footprint. A representative calculation confirming the results of this analysis is provided in Appendix A.4.

4.3. Economic Performance

The breakdown of the total system cost is provided for each working fluid in Figure 4-4. The payback period for each system is denoted in Figure 4-4 as “PP”. On average, the heat exchangers make up 74% of the total system cost. The refrigerant charge was the second most expensive piece of equipment in the simulations, accounting for about 19% of the average cost. The turbo-compression cooling system with R152a had the lowest total system cost of $181,846. The heat exchangers on the R152a system were the smallest which has a twofold benefit: the heat exchangers are cheaper and the internal volume of the heat exchangers is lower, resulting in a lower refrigerant charge. The highest system cost was found to be $310,137 with R245fa. Along with the lowest initial investment, the R152a TCCS had the lowest simple payback period of 1.46 years. The R245fa had the longest simple payback period of 2.78 years. Figure 4-5 shows a simple cash flow diagram for the systems examined in this study. The simple cash flow diagram starts in

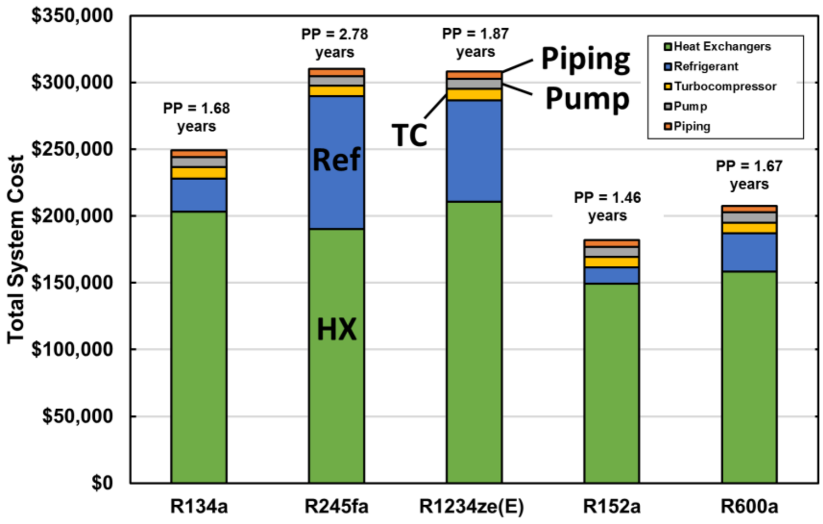

Figure 4-4: Breakdown of system cost for each working fluid. Payback period is denoted as “PP”.

the negative region of the plot due to the initial capital investment of the turbo-compression cooling system. Since the turbo-compression cooling system saves fuel expenditures each year, the total cash saved rises each year and eventually reaches the red dotted line, representing the payback period. Over a period of 10 years, the system with R1234ze(E) saves the most money at $1,339,666 while the R245fa system saves the least amount of money at $805,683. The R1234ze(E) system saved the most money over 10 years because it had the highest overall system COP at 0.415, saving $164,775 per year. Although the payback period of the R1234ze(E) system was the second highest, the high COP more than makes up for the high initial investment over a 10 year period. The R134a system saved $1,234,886 over 10 year, which was the second best performance found amongst these fluids. The R1234ze(E) system provided the greatest reduction in carbon dioxide emissions at 981,856 kg per year, while R245fa provide the lowest reduction in carbon dioxide emissions of 664,889 kg per year.

Figure 4-5: Simple cash flow after implementation of the TCCS over a 10 year period.

Figure 4-6 shows the results from the DCFROR analysis. The payback period optimized R152a TCCS had the lowest cost per kWh of cooling capacity at \$0.0060 per kWh, while the optimized R245fa system had the highest cost at \$0.0118 per kWh of cooling. The vapor compression system and diesel genset had a cost of \$0.030 per kWh of cooling, about 4 times the average cost of cooling for the payback period optimized turbo-compression cooling systems. The turbo-compression cooling system with R134a optimized to have the maximum thermodynamic COP provided cooling at \$0.029 per kWh. When the cost of the diesel generator was not included with the vapor compression chiller, the system could provide cooling at a rate of \$0.028 per kWh. On the vapor compression systems, the operating costs account for 96% of the cost of cooling energy because fuel cost is very high compared to the equipment cost. As presented above, the results of the simple payback period study and the discounted cash flow rate of return analysis

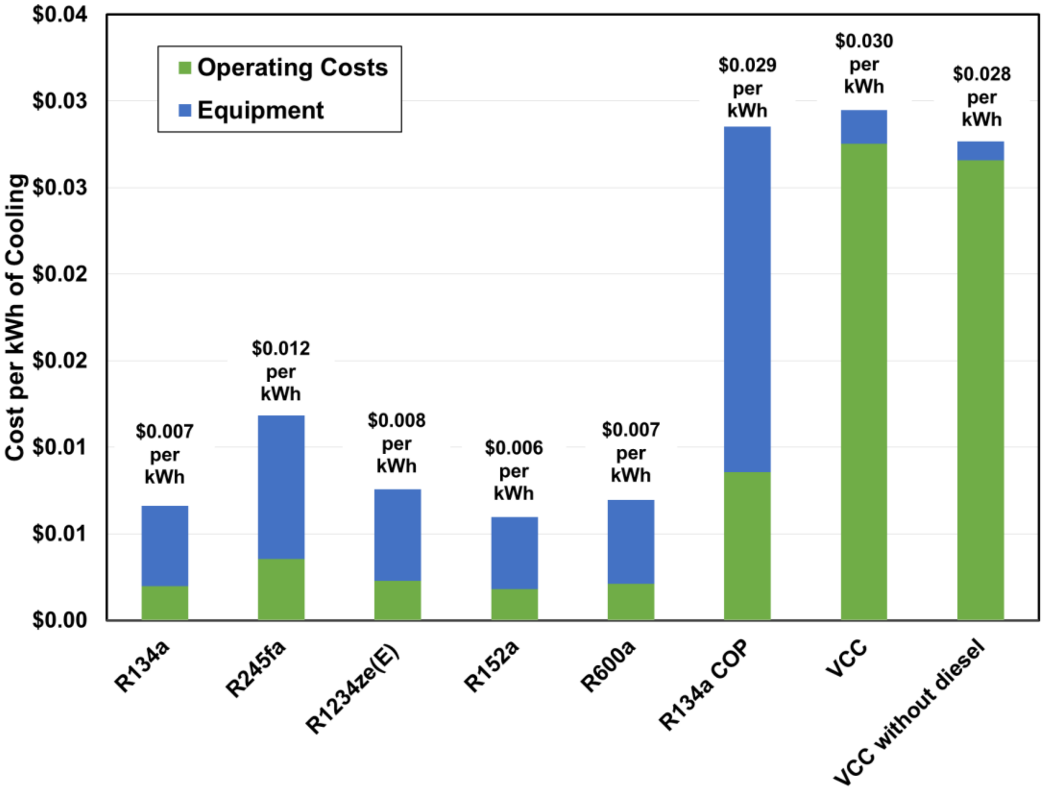

Figure 4-6: The cost per kWh of cooling capacity calculated from the discounted cash flow rate of return study.

were consistent. The R152a system had the lowest simple payback period and the lowest cost per kWh of cooling energy.

In addition, a sensitivity study was performed to determine which inputs had the greatest impact on the minimum selling price of cooling energy. The results of the sensitivity analysis are shown in Figure 4-7. Each input was changed by ±10% and the change in cooling energy cost was noted. Changes in the cooling capacity had the largest impact on the cost of cooling energy: reducing the cooling capacity by 10% increased the cost of cooling energy by 11%, while increasing the cooling capacity reduced the cost of cooling energy by 9%. The cooling capacity had a different trend when compared to the other inputs. When all other variables are unchanged, reducing he cooling capacity by 10% will increase the cost per kWh of cooling provided. In contrast, reducing the capex by 10% and leaving other variables unchanged, results in a lower cost

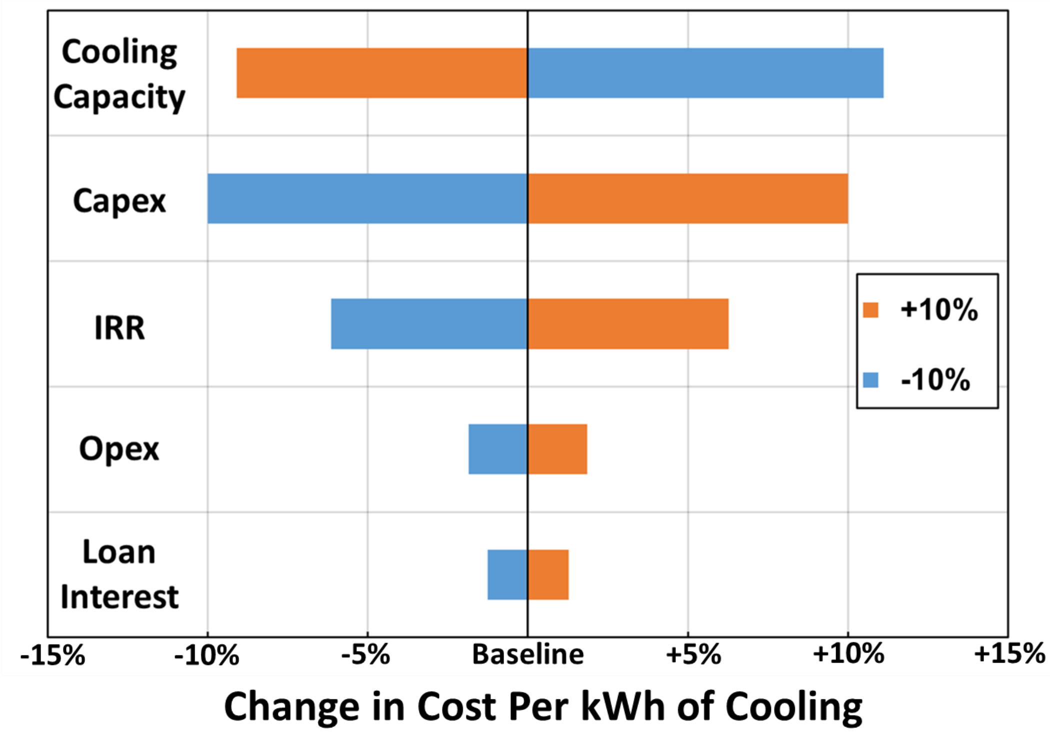

Figure 4-7: Sensitivity analysis on the minimum cost per kWh of cooling from the discounted cash flow rate of return study.

per kWh of cooling. Changing the initial equipment cost (capex) had the second greatest impact on the minimum cost of cooling.

The R152a TCCS had the lowest cost per kWh of cooling because it had the lowest initial capital investment ($181,846) and comparable performance to other systems (COP of 0.31 compared to average COP of 0.34). Since the operating expenses of the TCCS were set to be 3% of the initial capital expenditure, the operating costs of the R152a TCCS were also the lowest among all fluids. Another benefit of a smaller capital investment is that the R152a system required the smallest loan ($72,738, compared to the average of $100,558) and paid the least amount of interest on that loan compared to the other systems. The low initial investment provides three distinct benefits based on the inputs to this analysis. Although the R1234ze(E) had the best thermodynamic performance (and saved the most money in a 10 year, simplified cash flow analysis), the initial capital investment of $384,084 was too high for the thermodynamic performance to overcome.

In general, the COPs found in this work were lower than most other thermally activated cooling systems, as shown in the literature review of this document. The two primary causes for the low COPs found in this work are the heat sink temperatures and the goal of the optimization routine. The medium temperature heat sink in this modeling was 32°C seawater pumped from the ocean through condensing plate frame heat exchangers. The temperature of the seawater was a conservative choice based on typical operating locations for marine cargo vessels to demonstrate the viability of this heat activated cooling system in the most extreme locations. Typical vessels spend 97% of their operating lifetime in waters colder than 32°C. The COP of the TCCS will improve when the ships are operating in regions with cooler water, as evidenced from the literature review.

The goal of the optimization in this work was to find the point where the TCCS would have the minimum payback period. The minimum payback period doesn't necessarily equate to the system with the highest COP. There are significant costs associated with improving the COP of the system. As a representative example, a simulation of a turbo-compression cooling system with R134a aimed to optimize the coefficient of performance will be compared to the payback period optimized system with R134a. The T-s diagrams for the performance optimized system are provided in Figure 4-8. As shown in Figure 4-8a, the high COP optimization routine increased the refrigerant superheat at the boiler outlet, increasing the inlet enthalpy to the turbine. In addition, the effectiveness of the two-phase and superheated regions of the power cycle condenser increased the pressure ratio of the turbine. These two factors increased the amount of power output from the turbine which increased the thermal efficiency of the ORC. On the cooling cycle (4-8b), the high COP system had a lower compression ratio which decreased the compressor work input to the

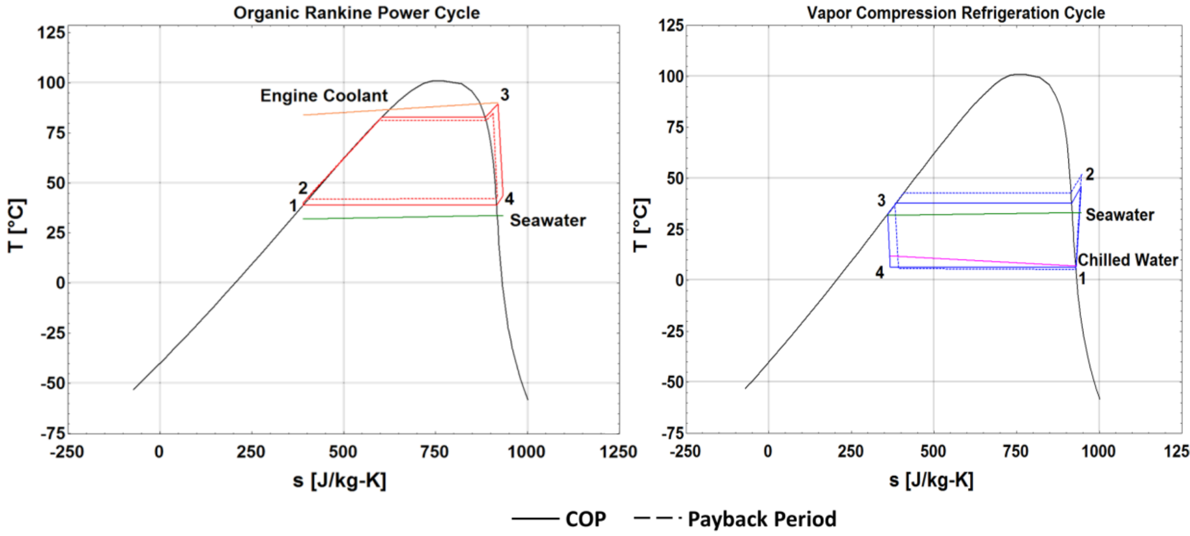

(a) (b)

Figure 4-8: Temperature-entropy diagrams for the (a) power cycle and (b) cooling cycle of a turbo-compression cooling system with working fluid R134a optimized to have a higher COP and optimized for payback period. The payback period optimized system is denoted as a dashed line.

system. In addition, the amount of subcooled at the condenser outlet was increased to shift the isenthalpic expansion further to the left on the T-s diagram. Shifting the isenthalpic expansion decreased the vapor quality at the chiller inlet, which increases the available enthalpy of vaporization that can be used for chilling the water stream. The decrease in compression ratio and decrease of inlet vapor quality improved the COP of the vapor compression cycle. Increasing the ORC thermal efficiency and cooling cycle COP improved the overall system COP.

The COP of the high efficiency case was 0.528 while the COP for the economic system was 0.384. Increasing the COP from 0.384 to 0.528 increased the annual savings by $61,931 per year. The total cost of the performance optimized system was $1.48 million compared to $249,254 for the payback period optimized system, equating to a 5.9 times increase in initial capital expenditures. The total costs for each system are compared in Figure 4-9. Over a period of 10 years, the payback period optimized system saved $610,320 more than the performance optimized

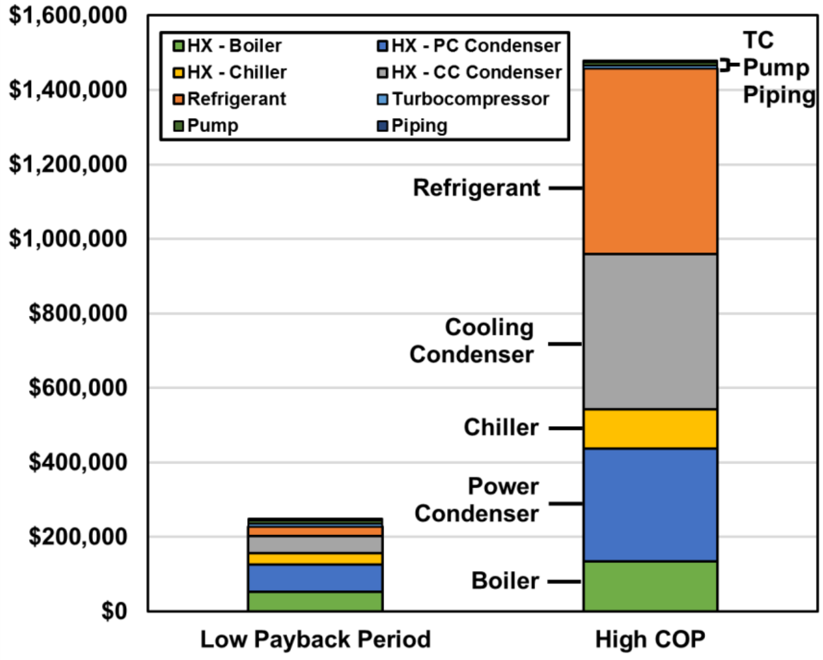

Figure 4-9: Comparison of total system cost for the TCCS with R134a designed for energy efficiency and the system designed to have a minimum payback period. The high COP TCCS is 4.4 times more expensive than the low payback period system.

system. The high efficiency system is obviously not the most economically efficient choice from the data presented here, emphasizing the point that the work in the literature is insufficient because it is too focused on the technical performance of these waste heat recovery systems.

The refrigerant charge had the most dramatic increase in cost when optimizing for COP instead of payback period, from \$24,787 (10% of total system cost) to \$497,286 (34% of total system cost). The refrigerant charge increased so dramatically because the total area of the heat exchangers increased from 863 m^2 to 15494 m^2. As the heat exchanger area increases, the amount of refrigerant to fill those heat exchangers also increases. The accuracy of the heat exchanger charge calculations were accurate to within 3% compared to quotes received from manufacturers. The total cost of the heat exchangers increased from \$203,155 (82% of total system cost) to \$959,952 (65% of the total system cost). The heat exchangers accounted for a smaller fraction of the total system cost because the refrigerant charge became a larger portion of the cost. The performance optimized condenser was 9.1 times more expensive on the cooling cycle and 4.2 times more expensive on the power cycle. A comparison of the heat exchangers is provided in Table 4-7. To achieve a higher COP, the input effectiveness values were changed until the COP reached the maximum value. The effectiveness in superheated region of the chiller had the highest change from the payback period to the performance optimized system, from 0.001 to 0.75. The increase in superheated chiller effectiveness increases the cooling duty of the cycle from 775 kW to 1067 kW. The COP of the cooling cycle increased from 5.06 to 6.29. In addition, the effectiveness of the superheated region of the boiler increased from 0.406 to 0.9173 which increased the temperature at the turbine inlet. Higher turbine inlet temperature increased the power output of the turbine and improved the thermal efficiency of the ORC from 8.1% to 8.9%.

The number of plates for each heat exchanger greatly increased due to the large increase in heat transfer area. It is unrealistic to have more than 400 plates on a plate and frame heat exchanger. Instead of adding more plates, a larger plate would be used to keep the total number of plates a realistic number. In this work, the same plate size was used for all heat exchangers for simplicity. This caused the pressure drops through the larger heat exchangers to be unreasonably small. Assuming the flow is well distributed through the plates, having more plates will decrease the amount of mass flow in each plate. Since the two-phase region on each plate dominates the pressure drop through the heat exchangers, decreasing mass flow rate per plate will significantly lower pressure drop through the heat exchangers. A large number of plates will also decrease the

Table 4-7: Comparison of the heat exchangers on a turbo-compression cooling system designed to have a minimum payback period and a high COP. R134a was the working fluid for both cases.

	Boiler			**Chiller**	
	R134a - PP	**R134a - COP**		**R134a - PP**	**R134a - COP**
ε: subcooled	0.703	0.7091		-	-
ε: two-phase	0.42	0.485		0.8016	0.92
ε: superheated	0.406	0.9173		0.001	0.75
# of Plates	162	888		108	996
ΔP (kPa)	0.77	0.16		5.66	3
UA (kW K^{-1})	216	296		251	549
Inlet Pressure (kPa)	2701	2791		359	370
Cost	$53,527	$134,579		$31,668	$106,078
	PC Condenser			**CC Condenser**	
	R134a - PP	**R134a - COP**		**R134a - PP**	**R134a - COP**
ε: subcooled	0.001	0.001		0.485	0.9
ε: two-phase	0.174	0.25		0.07398	0.19
ε: superheated	0.104	0.4845		0.4672	0.6348
# of Plates	205	2901		90	5264
ΔP (kPa)	4.26	0.857		3.5	0.183
UA (kW K^{-1})	202	309		89	203
Inlet Pressure (kPa)	1076	985		1126	956
Cost	$72,058	$302,442		$45,902	$416,854

heat transfer coefficient for the same reason: lowering the mass flow rate will hinder heat transfer performance. A more realistic estimate of heat exchanger size and total system cost can be found if larger plates were used on the boiler and condenser. Larger plates will also affect the pressure drop and heat transfer coefficients.

4.4. Sensitivity Analysis

A sensitivity analysis was performed in conjunction with the payback period optimization of the five different turbo-compression cooling systems. The sensitivity analysis determined which heat exchanger effectiveness had the largest impact on the payback period. For this analysis, the Reynolds number in the superheated regions of the heat exchangers was not set so the sensitivity of more heat exchanger effectivenesses could be examined. Three effectiveness values on the power cycle were studied: the two-phase region of the boiler, the two-phase region of the

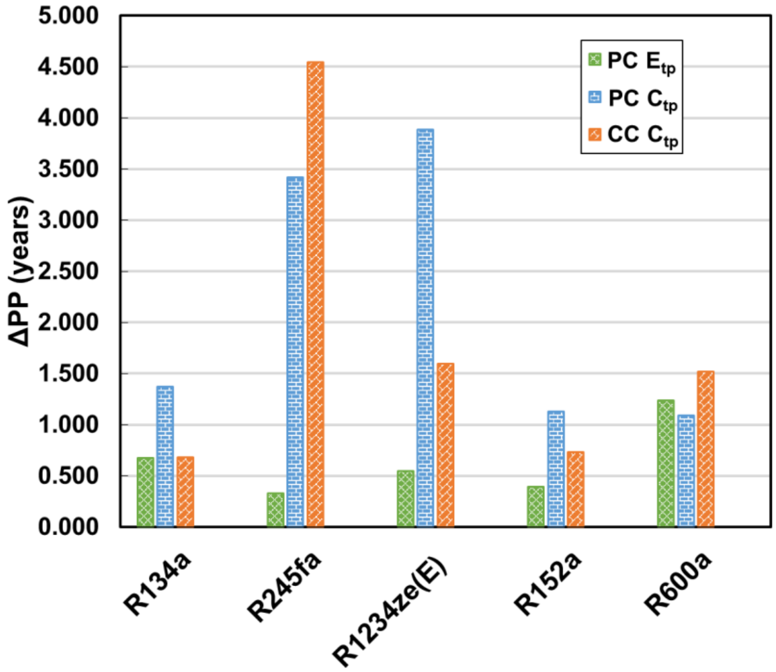

Figure 4-10: Change in payback period as a function of changing heat exchanger effectiveness in the designated regions by 0.1. The three effectiveness regions with the greatest impact on payback period are shown.

condenser, and the subcooled region of the condenser. On the cooling cycle, four effectiveness values were examined: the two-phase region of the chiller, the superheated region of the chiller, the subcooled region of the condenser, and the two-phase region of the condenser. The effectiveness values were changed one at a time by 0.1 and the change in payback period was noted for each working fluid.

The results of the sensitivity study are shown in Figure 4-10 where the three most impactful heat exchanger effectiveness values are shown for each working fluid. “CC” and “PC” represent cooling cycle and power cycle, respectively. “E” and “C” represent the evaporator or condenser while “tp”, “sc”, or “sh” represent the two-phase region, the subcooled region, or the superheated region in the heat exchangers. As an example, CC E_{tp} represents the effectiveness value in the two-phase region of the cooling cycle evaporator. In all simulations except for R600a, the two-phase region of the condensers on the power and cooling cycles had the largest impact on payback period. The average change in payback period was 2.18 years for the power cycle condenser and 1.82 years for the cooling cycle condenser when the effectiveness values in the two-phase regions were changed by 0.1. This result makes sense because the condensers were the largest and most expensive heat exchangers due to the titanium material requirements, heat duties, and approach temperatures. The two-phase region was the most impactful of the regions in the condenser because most of the heat is exchanged in this region. Since the condenser saturation pressure is set by the effectiveness value, changes in effectiveness of the condensers will impact the pressure ratio of the power and cooling cycles. As shown previously, the pressure ratio of each cycle has a large impact on the performance, which is why the systems were so sensitive to condenser effectiveness. The working fluids with the lowest enthalpies of vaporization at the boiler saturation pressure, R134a and R1234ze(E), were most sensitive to the power cycle condenser effectiveness.

Since these fluids had a lower i_{fg}, they were more sensitive than the other fluids to changes in the power cycle pressure ratio.

The R600a system was more sensitive to the two-phase region of the boiler than the power cycle condenser because of the shape of the saturated liquid and vapor line on the P-h diagram at high pressures. As shown in purple on Figure 4-2, the slope of the saturated liquid for R600a above 10^3 kPa is very low. Small changes in the effectiveness of the two-phase region of the boiler will greatly change the enthalpy of vaporization for the R600a system. As shown previously, the enthalpy of vaporization has a large impact on the power output of the turbine and thus the overall system performance.

The two-phase region of the chiller had an extremely small impact on the payback period of the system. Averaged over the five working fluids, changing the effectiveness of the chiller two-phase region changed the payback period by 0.052 years. The model was even less sensitive to the superheated region of the chiller: an average change of 0.01 years was found for a change of 0.1. Changes to the chiller did not have as large of an impact on the payback period because the chiller was the least costly heat exchanger in the system. If the cost of the condensers was not multiplied by 1.6 for using titanium plates, the model may be more sensitive to changes in the chiller effectiveness values because their costs would be more comparable.

The results of the sensitivity analysis were relatively consistent across the working fluids, except the R245fa system. Throughout all of the simulations, the R245fa condensers had the largest impact on the payback period. The resulting change in payback period from altering the power and cooling cycle condenser effectiveness values was 3.42 years and 4.54 years (compared to the averages of 2.18 and 1.82), respectively. The working fluid R245fa has a low slope of the saturated liquid line on the P-h diagram above 10^2 kPa, which means that very slight increases in condenser pressure can greatly increase the quality at the inlet of the chiller (shifting the vertical line of throttling to the right on a T-s diagram). Shifting the throttling line to the right will decrease the cooling capacity of the evaporating heat exchanger on the cooling cycle, lowering the cooling cycle COP and overall system COP. The R245fa system was also the most sensitive of the fluids to changes in the subcooled effectiveness of the power condenser. The change in payback period was 0.313 years, where the average change for the other four fluids was 0.064 years. This comes about for similar reasons to the cooling condenser. Small changes in the effectiveness will have change the saturation pressure which will have a significant impact due to the slope of the saturated liquid line of R245fa. As a result, the turbine pressure ratio will change which has a strong impact on the thermal efficiency of the power cycle. In addition, the R245fa system was very sensitive the pressure drop of the heat exchangers, as explained in the pressure drop discussion in Section 4.2. Thus, very small changes in the effectiveness of the condenser will affect the saturation pressure in the condenser and have a profound impact of the cooling capacity and COP of the R245fa turbo-compression cooling system.

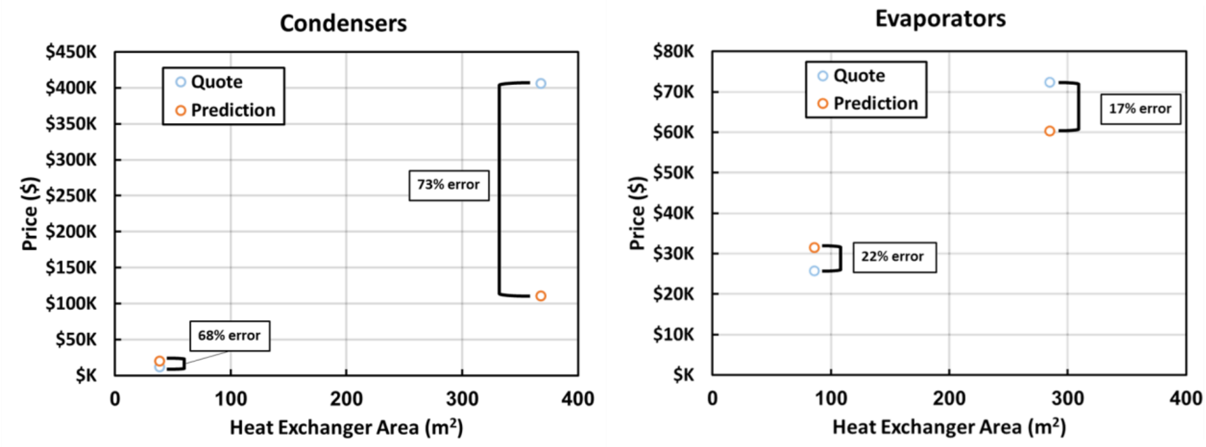

Figure 4-11: Comparison of actual plate heat exchanger costs with the cost model from Brown.

4.5. Model Validation

Model validation was performed using quotes received from distributors of plate heat exchangers at this scale. Quotes were acquired for a 1630 kW condenser with titanium plates, a 415 kW condenser with stainless steel plates, and two evaporators with stainless steel plates with capacities of 400 kW and 228 kW. As shown in Figure 4-11, the cost model from Brown underpredicted the cost of the 1.63 MW titanium plate condensing heat exchanger by 73% while overpredicting the cost of the 415 kW stainless steel condenser by 68%. The Brown cost model predicted cost within 22% for both quotes of the stainless steel evaporating heat exchangers.

To account for the inaccuracy of the cost model, the cost of the titanium heat exchangers was increased to match the quote and the minimum cost of cooling energy was calculated for the R134a payback period optimized system. The results of the updated discounted cash flow rate of

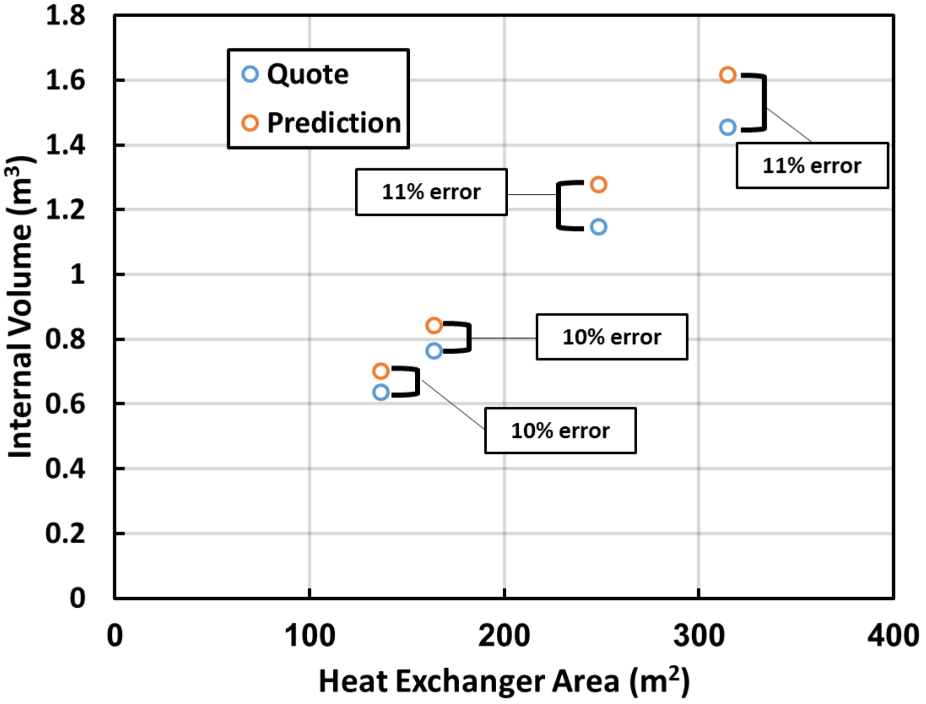

Figure 4-12: Comparison of the internal volume calculations in this work and the internal volume provided from distributor quotes.

return study are shown in Figure 4-12. The cost of the titanium heat exchangers was multiplied by 3.66 times to match the quote received from the distributors. After increasing the cost, the cost per kWh of cooling for the R134a system increased from \$0.0066 per kWh to \$0.015 per kWh. Despite the cost increase, the price of cooling energy from the TCCS was still 2 times cheaper than cooling energy from the vapor compression chiller. In addition, the internal charge calculations from this work were validated against the plate heat exchanger quotes received from distributors as shown in Figure 4-13. From the distributor quote, the internal volume of one side of the titanium condensing heat exchanger was given as 1.689 m^3 with 238 plates. Thus, the volume of each channel of the quoted heat exchanger was 0.014 m^3. The volume per channel from the quote was multiplied by the number of channels for the heat exchangers simulated in this work. This value is assumed to be the 'true' or actual value of the heat exchanger volume. The present work overpredicted the internal volume of the heat exchangers by about 10%. Since the error was

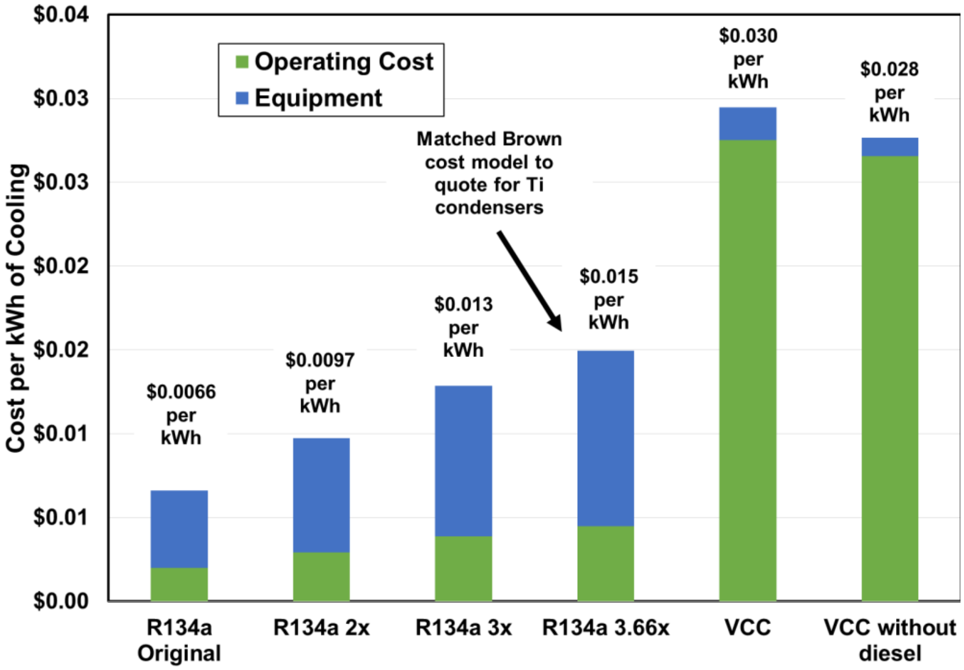

Figure 4-13: Cost of cooling energy for TCCS with more accurate titanium plate heat exchanger cost model.

constant across the simulations, the 10% error is likely a systematic error where a small change in the geometry inputs that were estimated would likely reduce the over prediction.

CHAPTER 5. Conclusions and Recommendation for Further Work

The current study sought to understand the technoeconomic performance of a thermally activated cooling system designed to recover waste heat in a large marine diesel engine-generator set (genset). Large refrigerated cargo ships use a significant part of the genset power output to provide cooling for cargo. Utilizing the waste heat from the gensets to produce cooling can improve the efficiency of their power generating systems beyond 40% thermal efficiency, which is considered state of the art, and reduce fuel consumption to save money and reduce emissions. Waste heat is available in the engine coolant and the exhaust gas. This work focused on the recovery of waste heat in the engine coolant due to favorable heat transfer characteristics and ease of implementation.

The thermally activated cooling system used for this study was a turbo-compression cooling system which is an organic Rankine cycle directly coupled to a vapor compression refrigeration cycle. The turbine on the ORC and the compressor on the vapor compression cycle were both centrifugal machines which shared the same shaft to directly couple the power transfer. A detailed thermodynamic, heat exchanger, and economic model was developed to study the technical and economic performance of the system for five different working fluids. In the thermodynamic analysis, the heat exchangers were divided into regions based on the working fluid phase (subcooled, two-phase, or superheated) while a Cordier analysis was performed on the turbomachinery to calculate size and speed of the device. Heat transfer and pressure drop correlations from the literature were used to calculate the size and pressure loss through the heat exchangers on the power and cooling cycles. All of the major components were accounted for in the economic modeling: heat exchangers, turbomachine, refrigerant charge, power cycle pump, and piping. The simple payback period of the system was calculated based on the initial capital expenditures and the fuel savings per year. In addition, a discounted cash flow rate of return analysis was performed to find the cost per kWh of cooling provided by the turbo-compression cooling system. Then, the system was optimized by varying the effectiveness values in the heat exchangers until the minimum payback period was found. This procedure was completed for all five working fluids: R134a, R1234ze(E), R152a, R245fa, and R600a.

The turbo-compression cooling system with working fluid R152a had the lowest simple payback period of 1.46 years. This system had a cooling capacity of 626 kW with a COP of 0.31 and saved $181,846 per year by reducing fuel consumption. The R245fa had the longest payback period at 2.78 years with the lowest cooling capacity and COP at 539 kW and 0.27, respectively. The system with R152a provided cooling at $0.006 per kWh of capacity, which was the lowest in this study and 4 times less than the cost of providing cooling with a vapor compression system. The system with R1234ze(E) saved the most money over a 10 year operational lifetime at $1,329,666 while the R245fa system saved the least money over 10 years at $805,683. R1234ze(E) system reduced the emission of CO2 by 981,856 kg per year. Due to the flammable nature of R152a and R600a, the best fluid to use in this shipboard application would be R1234ze(E) or R134a. R134a has slightly better technoeconomic performance than R1234ze(E), but R1234ze(E) has a 100 year global warming potential of 6 compared to 1430 with R134a. The system with R1234ze(E) will pay out the most money over a 10 year period while eliminating concerns of flammability and environmental hazards. In addition, R1234ze(E) has a turbo-compressor size and speed that is well within realistic limits of manufacturing and design to achieve 80% isentropic efficiency.

5.1. Recommendations for Future Work

There are a few items should be investigated further. The key parts of the future work for this study are as follows:

- Different working fluids should be studied on each side of the cycle. In this work, it was assumed the power and cooling cycles used the same working fluid for simplicity. In future work, different fluids should be used on each cycle to simultaneously maximize the thermal efficiency of the ORC and the COP of the vapor compression refrigeration cycle. The size and speed of the turbocompressor must match on the power and cooling cycles when using different fluids. For example, if R600a was used on the cooling cycle and R134a was used on the power cycle, the overall COP of the system could improve.
- More advanced configurations of the power and cooling cycles should be investigated. State of the art organic Rankine cycles have an internal recuperator to transfer heat from the turbine outlet to the pump outlet. This pre-heats the fluid before it enters the boiler which will improve the performance of the cycle. In addition, a suction line heat exchanger should be implemented on the cooling cycle to transfer heat from the condenser outlet to the evaporator outlet. This will improve the performance of the cooling cycle and lower the risk of forming liquid in the compressor. In some special cases, a cross cycle heat exchanger may be warranted to heat the fluid leaving the recuperator (before the boiler inlet) using the fluid that is exiting the compressor on the cooling cycle. This could further improve performance of the turbo-compression cooling system.

- Investigating different waste heat scenarios and ambient conditions will be important to confirm the performance of this system. Different waste heat scenarios could include gas turbine or diesel engine exhaust which would quantify the importance of waste heat temperature, phase, and flow rate. In addition, examining different ambient conditions is critical to better understand how the condensing temperature will affect the performance of the turbo-compression cooling system. This is an essential step towards commercialization of the turbo-compression cooling system.
- Predicting the off-design performance of a specific design point turbo-compression cooling system will provide valuable knowledge that will assist in bringing this technology to the market. Detailed performance maps of the turbine and compressor would have to be generated. In addition, the heat exchanger geometry and number of plates would be a fixed input.

REFERENCES

[1] United Nations, 2017, “World Population Prospects: The 2010 Revision” [Online]. Available: https://esa.un.org/unpd/wpp/DataQuery/.

[2] Energy Information Agministration, 2017, “Annual Energy Outlook 2017,” **0383**(January), p. 1.

[3] Enerdata, “Total Energy Consumption” [Online]. Available: https://yearbook.enerdata.net/total-energy/world-consumption-statistics.html.

[4] Little, A. B., and Garimella, S., 2011, “Comparative Assessment of Alternative Cycles for Waste Heat Recovery and Upgrade,” Energy, **36**(7), pp. 4492–4504.

[5] Lawrence Livermore National Laboratory, “Estimated U.S. Energy Consumption in 2016: 97.3 Quads.”

[6] NASA JPL, 2018, “Climate Change: How Do We Know?” [Online]. Available: https://climate.nasa.gov/evidence/.

[7] Carbon Tax Center, “What’s a Carbon Tax?” [Online]. Available: https://www.carbontax.org/whats-a-carbon-tax/.

[8] The World Bank, 2013, *Putting a Price on Carbon with a Tax Carbon Tax at a Glance*.

[9] US Department of Energy, 2015, “Chapter 6: Innovating Clean Energy Technologies in Advanced Manufacturing | Waste Heat Recovery Technology Assessment,” Quadrenn. Technol. Rev.

[10] Little, A. B., and Garimella, S., 2011, “Comparative Assessment of Alternative Cycles for Waste Heat Recovery and Upgrade,” Energy, **36**(7), pp. 4492–4504.

[11] Rattner, A. S., and Garimella, S., 2011, “Energy Harvesting, Reuse and Upgrade to Reduce Primary Energy Usage in the USA,” Energy, **36**(10), pp. 6172–6183.

[12] Sunden, B., 2005, “High Temperature Heat Exchangers (HTHE),” (September), pp. 226–238.

[13] Minerals, Metals, M. S., “Linking Transformational Materials and Processing for an Energy-Efficient and Low-Carbon Economy.”

[14] Min, J. K., Jeong, J. H., Ha, M. Y., and Kim, K. S., 2009, “High Temperature Heat Exchanger Studies for Applications to Gas Turbines,” (January 2015).

[15] Angelino, G., and Invernizzi, C., 2003, “Experimental Investigation on the Thermal Stability of Some New Zero ODP Refrigerants,” Int. J. Refrig., **26**(1), pp. 51–58.

[16] Ito, M., Dang, C., and Hihara, E., 2014, “Thermal Decomposition of Lower-GWP Refrigerants,” Int. Refrig. Air Cond. Conf., p. 1538.

[17] Exergy, “Current ORC Installations” [Online]. Available: http://exergy-orc.com/references/installations.

[18] World Cement, “Q&A: ORC and Kalina.”

[19] Zhang, X., Wu, L., Wang, X., and Ju, G., 2016, “Comparative Study of Waste Heat Steam SRC, ORC and S-ORC Power Generation Systems in Medium-Low Temperature,” Appl. Therm. Eng., **106**, pp. 1427–1439.

[20] Rochau, G. E., *Commercializing the SCO 2 Recompression Closed Brayton Cycle Pathway to “ Technology Commercialization .”*

[21] Matsuda, K., and Kurosaki, D., 2012, “Low Heat Power Generation System,” 3rd ASCON-IEEChE 2012, **35**, pp. 147–150.

[22] Shmroukh, A. N., Ali, A. H. H., and Ookawara, S., 2015, “Adsorption Working Pairs for Adsorption Cooling Chillers: A Review Based on Adsorption Capacity and Environmental Impact,” Renew. Sustain. Energy Rev., **50**, pp. 445–456.

[23] Kubota, M., Ueda, T., Fujisawa, R., Kobayashi, J., Watanabe, F., Kobayashi, N., and Hasatani, M., 2008, “Cooling Output Performance of a Prototype Adsorption Heat Pump with Fin-Type Silica Gel Tube Module,” Appl. Therm. Eng., **28**(2–3), pp. 87–93.

[24] Jiangzhou, S., Wang, R. Z., Lu, Y. Z., Xu, Y. X., and Wu, J. Y., 2005, “Experimental Study on Locomotive Driver Cabin Adsorption Air Conditioning Prototype Machine,” Energy Convers. Manag., **46**(9–10), pp. 1655–1665.

[25] Chua, H. T., Ng, K. C., Wang, W., Yap, C., and Wang, X. L., 2004, “Transient Modeling of a Two-Bed Silica Gel-Water Adsorption Chiller,” Int. J. Heat Mass Transf., **47**(4), pp. 659–669.

[26] Zhang, L. Z., 2000, “Design and Testing of an Automobile Waste Heat Adsorption Cooling System,” Appl. Therm. Eng., **20**(1), pp. 103–114.

[27] Wang, R. Z., 2008, “Efficient Adsorption Refrigerators Integrated with Heat Pipes,” Appl. Therm. Eng., **28**(4), pp. 317–326.

[28] Wang, K., and Vineyard, E. A., 2011, “New Opportunities for Solar Adsorption Refrigeration,” ASHRAE J., **September**, pp. 14–24.

[29] Gong, L. X., Wang, R. Z., Xia, Z. Z., and Chen, C. J., 2011, “Design and Performance Prediction of a New Generation Adsorption Chiller Using Composite Adsorbent,” Energy Convers. Manag., **52**(6), pp. 2345–2350.

[30] Mahdavikhah, M., and Niazmand, H., 2013, “Effects of Plate Finned Heat Exchanger Parameters on the Adsorption Chiller Performance,” Appl. Therm. Eng., **50**(1), pp. 939–949.

[31] Wang, D. C., Shi, Z. X., Yang, Q. R., Tian, X. L., Zhang, J. C., and Wu, J. Y., 2007, “Experimental Research on Novel Adsorption Chiller Driven by Low Grade Heat Source,” Energy Convers. Manag., **48**(8), pp. 2375–2381.

[32] Chorowski, M., and Pyrka, P., 2015, “Modelling and Experimental Investigation of an Adsorption Chiller Using Low-Temperature Heat from Cogeneration,” Energy, **92**, pp. 221–229.

[33] Ali, S. M., and Chakraborty, A., 2015, “Thermodynamic Modelling and Performance Study of an Engine Waste Heat Driven Adsorption Cooling for Automotive Air-Conditioning,” Appl. Therm. Eng., **90**(X), pp. 54–63.

[34] Verde, M., Harby, K., de Boer, R., and Corberán, J. M., 2016, “Performance Evaluation of a Waste-Heat Driven Adsorption System for Automotive Air-Conditioning: Part II - Performance Optimization under Different Real Driving Conditions,” Energy, **115**, pp. 996–1009.

[35] Alahmer, A., Wang, X., Al-Rbaihat, R., Amanul Alam, K. C., and Saha, B. B., 2016, “Performance Evaluation of a Solar Adsorption Chiller under Different Climatic Conditions,” Appl. Energy, **175**, pp. 293–304.

[36] Calise, F., Dentice d’Accadia, M., Figaj, R. D., and Vanoli, L., 2016, “A Novel Solar-Assisted Heat Pump Driven by Photovoltaic/Thermal Collectors: Dynamic Simulation and Thermoeconomic Optimization,” Energy, **95**, pp. 346–366.

[37] Stanek, W., and Gazda, W., 2014, “Exergo-Ecological Evaluation of Adsorption Chiller System,” Energy, **76**, pp. 42–48.

[38] Huang, B. J., Chang, J. M., Petrenko, V. A., and Zhuk, K. B., 1998, “A Solar Ejector

Cooling System Using Refrigerant R141b," Sol. Energy, **64**(4–6), pp. 223–226.

[39] Ma, X., Zhang, W., Omer, S. A., and Riffat, S. B., 2010, "Experimental Investigation of a Novel Steam Ejector Refrigerator Suitable for Solar Energy Applications," Appl. Therm. Eng., **30**(11–12), pp. 1320–1325.

[40] Murthy, S. S., Balasubramanian, R., and Murthy, M. V. K., 1991, "Experiments on Vapour Jet Refrigeration System Suitable for Solar Energy Applications," Renew. Energy, **1**(5–6), pp. 757–768.

[41] Yapici, R., Ersoy, H. K., Aktoprakoğlu, A., Halkaci, H. S., and Yiğit, O., 2008, "Experimental Determination of the Optimum Performance of Ejector Refrigeration System Depending on Ejector Area Ratio," Int. J. Refrig., **31**(7), pp. 1183–1189.

[42] Shestopalov, K. O., Huang, B. J., Petrenko, V. O., and Volovyk, O. S., 2015, "Investigation of an Experimental Ejector Refrigeration Machine Operating with Refrigerant R245fa at Design and Off-Design Working Conditions. Part 1. Theoretical Analysis," Int. J. Refrig., **55**, pp. 201–211.

[43] Mazzelli, F., and Milazzo, A., 2015, "Performance Analysis of a Supersonic Ejector Cycle Working with R245fa," Int. J. Refrig., **49**(0), pp. 79–92.

[44] Milazzo, A., and Rocchetti, A., 2015, "Modelling of Ejector Chillers with Steam and Other Working Fluids," Int. J. Refrig., **57**, pp. 277–287.

[45] Roman, R., and Hernandez, J. I., 2011, "Performance of Ejector Cooling Systems Using Low Ecological Impact Refrigerants," Int. J. Refrig., **34**(7), pp. 1707–1716.

[46] Chen, J., Havtun, H., and Palm, B., 2014, "Screening of Working Fluids for the Ejector Refrigeration System," Int. J. Refrig., **47**(0), pp. 1–14.

[47] Besagni, G., Mereu, R., Di Leo, G., and Inzoli, F., 2015, "A Study of Working Fluids for Heat Driven Ejector Refrigeration Using Lumped Parameter Models," Int. J. Refrig., **58**, pp. 154–171.

[48] Petrenko, V. O., and Volovyk, O. S., 2011, "Theoretical Study and Design of a Low-Grade Heat-Driven Pilot Ejector Refrigeration Machine Operating with Butane and Isobutane and Intended for Cooling of Gas Transported in a Gas-Main Pipeline," Int. J. Refrig., **34**(7), pp. 1699–1706.

[49] Dai, Y., Wang, J., and Gao, L., 2009, "Exergy Analysis, Parametric Analysis and Optimization for a Novel Combined Power and Ejector Refrigeration Cycle," Appl. Therm. Eng., **29**(10), pp. 1983–1990.

[50] Xia, J., Wang, J., Lou, J., Zhao, P., and Dai, Y., 2016, "Thermo-Economic Analysis and Optimization of a Combined Cooling and Power (CCP) System for Engine Waste Heat Recovery," Energy Convers. Manag., **128**, pp. 303–316.

[51] Sadeghi, M., Mahmoudi, S. M. S., and Khoshbakhti Saray, R., 2015, "Exergoeconomic Analysis and Multi-Objective Optimization of an Ejector Refrigeration Cycle Powered by an Internal Combustion (HCCI) Engine," Energy Convers. Manag., **96**, pp. 403–417.

[52] MARPOL, "EEDI and SEEMP" [Online]. Available: https://www.marpol-annex-vi.com/eedi-seemp/.

[53] Paanu, T., Aho, P., Ekman, J. K., Saveljeff, H., and Niemi, S., "Effect of the Exhaust Gas Side Fouling on the Performance of a Plate and Shell Type Heat Exchanger."

[54] Lance, M. J., Sluder, C. ., Wang, H., and Storey, J. M. E., "Direct Measurement of EGR Cooler Deposit Thermal Properties for Improved Understanding of Cooler Foulding."

[55] Cao, T., Lee, H., Hwang, Y., Radermacher, R., and Chun, H. H., 2016, "Modeling of Waste Heat Powered Energy System for Container Ships," Energy, **106**, pp. 408–421.

[56] Kizilkan, Ö., Şencan, A., and Kalogirou, S. A., 2007, “Thermoeconomic Optimization of a LiBr Absorption Refrigeration System,” Chem. Eng. Process. Process Intensif., **46**(12), pp. 1376–1384.

[57] Trane, “Steam Driven Absorption Chillers” [Online]. Available: https://www.trane.com/content/dam/Trane/Commercial/global/products-systems/equipment/chillers/absorption-liquid/steam_drivenabsorptionchillers.pdf.

[58] Al-Tahaineh, H., Frihat, M., and Al-Rashdan, M., 2013, “Exergy Analysis of a Single-Effect Water-Lithium Bromide Absorption Chiller Power by Waste Energy Source for Different Cooling Capacities,” Energy and Power, **3**(6), pp. 106–118.

[59] Manu, S., and Chandrashekar, T. K., 2016, “A Simulation Study on Performance Evaluation of Single-Stage LiBr–H2O Vapor Absorption Heat Pump for Chip Cooling,” Int. J. Sustain. Built Environ., **5**(2), pp. 370–386.

[60] de Vega, M., Almendros-Ibañez, J. A., and Ruiz, G., 2006, “Performance of a LiBr-Water Absorption Chiller Operating with Plate Heat Exchangers,” Energy Convers. Manag., **47**(18–19), pp. 3393–3407.

[61] Jakob, U., Eicker, U., Schneider, D., Taki, A. H., and Cook, M. J., 2008, “Simulation and Experimental Investigation into Diffusion Absorption Cooling Machines for Air-Conditioning Applications,” Appl. Therm. Eng., **28**(10), pp. 1138–1150.

[62] González-Gil, A., Izquierdo, M., Marcos, J. D., and Palacios, E., 2011, “Experimental Evaluation of a Direct Air-Cooled Lithium Bromide-Water Absorption Prototype for Solar Air Conditioning,” Appl. Therm. Eng., **31**(16), pp. 3358–3368.

[63] Ge, Y. T., Tassou, S. A., and Chaer, I., 2009, “Modelling and Performance Evaluation of a Low-Temperature Ammonia-Water Absorption Refrigeration System,” Int. J. Low-Carbon Technol., **4**(2), pp. 68–77.

[64] Le Lostec, B., Galanis, N., and Millette, J., 2012, “Experimental Study of an Ammonia-Water Absorption Chiller,” Int. J. Refrig., **35**(8), pp. 2275–2286.

[65] Ouadha, A., and El-Gotni, Y., 2013, “Integration of an Ammonia-Water Absorption Refrigeration System with a Marine Diesel Engine: A Thermodynamic Study,” Procedia Comput. Sci., **19**(Seit), pp. 754–761.

[66] Chua, H. T., Ng, K. C., Malek, A., Kashiwagi, T., Akisawa, A., and Saha, B. B., 2001, “Multi-Bed Regenerative Adsorption Chiller - Improving the Utilization of Waste Heat and Reducing the Chilled Water Outlet Temperature Fluctuation,” Int. J. Refrig., **24**(2), pp. 124–136.

[67] Douss, N., and Meunier, F., 1989, “Experimental Study of Cascading Adsorption Cycles,” Chem. Eng. Sci., **44**(2), pp. 225–235.

[68] de Vega, M., Almendros-Ibañez, J. A., and Ruiz, G., 2006, “Performance of a LiBr-Water Absorption Chiller Operating with Plate Heat Exchangers,” Energy Convers. Manag., **47**(18–19), pp. 3393–3407.

[69] Le Lostec, B., Galanis, N., and Millette, J., 2013, “Simulation of an Ammonia-Water Absorption Chiller,” Renew. Energy, **60**, pp. 269–283.

[70] Manzela, A. A., Hanriot, S. M., Cabezas-Gómez, L., and Sodré, J. R., 2010, “Using Engine Exhaust Gas as Energy Source for an Absorption Refrigeration System,” Appl. Energy, **87**(4), pp. 1141–1148.

[71] Keinath, C. M., Delahanty, J. C., and Garrabrant, M. a, 2012, “Diesel Engine Waste-Heat Driven Ammonia-Water Absorption System for Space-Conditioning Applications,” Int. Refrig. Air Cond. Conf., p. 2493 (1-10).

[72] Longo, G. A., Gasparella, A., and Zilio, C., 2002, "Simulation of an Absorption Chiller Driven by the Heat Recovery of an Internal Combustion Engine, Purdue Conference."

[73] Palomba, V., Aprile, M., Vasta, S., Gullì, G., Freni, A., and Motta, M., 2016, "Study and Evaluation of Two Innovative Waste-Heat Driven Refrigeration Systems for Fishing Vessels Applications," Energy Procedia, **101**(September), pp. 838–845.

[74] Cao, T., Lee, H., Hwang, Y., Radermacher, R., and Chun, H. H., 2015, "Performance Investigation of Engine Waste Heat Powered Absorption Cycle Cooling System for Shipboard Applications," Appl. Therm. Eng., **90**, pp. 820–830.

[75] Bereche, R. P., Palomino, R. G., and Nebra, S. a, 2009, "Thermoeconomic Analysis of a Single and Double-Effect LiBr / H 2 O Absorption Refrigeration System *," Control, **12**(2), pp. 89–96.

[76] Misra, R. D., Sahoo, P. K., and Gupta, A., 2005, "Thermoeconomic Optimization of a LiBr/H2O Absorption Chiller Using Structural Method," J. Energy Resour. Technol., **127**(2), pp. 119–124.

[77] Misra, R. D., Sahoo, P. K., and Gupta, A., 2006, "Thermoeconomic Evaluation and Optimization of an Aqua-Ammonia Vapour-Absorption Refrigeration System," Int. J. Refrig., **29**(1), pp. 47–59.

[78] Thermax, and BROAD, 2018, "Quotes for Absorption Chiller."

[79] Abbaspour, M., and Saraei, A. R., 2015, "Thermoeconomic Analysis and Multi-Objective Optimization of a LiBr-Water Absorption Refrigeration System," Int. J. Environ. Res., **9**(1), pp. 61–68.

[80] Boer, D., Medrano, M., and Nogu??s, M., 2005, "Exergy and Structural Analysis of an Absorption Cooling Cycle and the Effect of Efficiency Parameters," Int. J. Thermodyn., **8**(4), pp. 191–198.

[81] Lu, Y., Roskilly, A. P., and Ma, C., 2017, "A Techno-Economic Case Study Using Heat Driven Absorption Refrigeration Technology in UK Industry," Energy Procedia, **123**, pp. 173–179.

[82] Farshi, L. G., Mahmoudi, S. S., Rosen, M. A., and Yari, M., 2012, "Use of Low Grade Heat Sources in Combined Ejector–double Effect Absorption Refrigeration Systems," Proc. Inst. Mech. Eng. Part A J. Power Energy, **226**(5), pp. 607–622.

[83] Garousi Farshi, L., Mahmoudi, S. M. S., and Rosen, M. A., 2013, "Exergoeconomic Comparison of Double Effect and Combined Ejector-Double Effect Absorption Refrigeration Systems," Appl. Energy, **103**, pp. 700–711.

[84] Kim, K. H., and Perez-Blanco, H., 2015, "Performance Analysis of a Combined Organic Rankine Cycle and Vapor Compression Cycle for Power and Refrigeration Cogeneration," Appl. Therm. Eng., **91**, pp. 964–974.

[85] Li, H., Bu, X., Wang, L., Long, Z., and Lian, Y., 2013, "Hydrocarbon Working Fluids for a Rankine Cycle Powered Vapor Compression Refrigeration System Using Low-Grade Thermal Energy," Energy Build., **65**, pp. 167–172.

[86] Bu, X. B., Li, H. S., and Wang, L. B., 2013, "Performance Analysis and Working Fluids Selection of Solar Powered Organic Rankine-Vapor Compression Ice Maker," Sol. Energy, **95**, pp. 271–278.

[87] Li, Y. R., Wang, X. Q., Li, X. P., and Wang, J. N., 2014, "Performance Analysis of a Novel Power/Refrigerating Combined-System Driven by the Low-Grade Waste Heat Using Different Refrigerants," Energy, **73**, pp. 543–553.

[88] Wang, H., Peterson, R., Harada, K., Miller, E., Ingram-Goble, R., Fisher, L., Yih, J., and

Ward, C., 2011, “Performance of a Combined Organic Rankine Cycle and Vapor Compression Cycle for Heat Activated Cooling,” Energy, **36**(1), pp. 447–458.

[89] Wang, H., Peterson, R., and Herron, T., 2011, “Design Study of Configurations on System COP for a Combined ORC (Organic Rankine Cycle) and VCC (Vapor Compression Cycle),” Energy, **36**(8), pp. 4809–4820.

[90] Aphornratana, S., and Sriveerakul, T., 2010, “Analysis of a Combined Rankine-Vapour-Compression Refrigeration Cycle,” Energy Convers. Manag., **51**(12), pp. 2557–2564.

[91] Yue, C., You, F., and Huang, Y., 2016, “Thermal and Economic Analysis of an Energy System of an ORC Coupled with Vehicle Air Conditioning,” Int. J. Refrig., **64**, pp. 152–167.

[92] Molés, F., Navarro-Esbrí, J., Peris, B., Mota-Babiloni, A., and Kontomaris, K., 2015, “Thermodynamic Analysis of a Combined Organic Rankine Cycle and Vapor Compression Cycle System Activated with Low Temperature Heat Sources Using Low GWP Fluids,” Appl. Therm. Eng., **87**, pp. 444–453.

[93] Wang, X. Q., Li, X. P., Li, Y. R., and Wu, C. M., 2015, “Payback Period Estimation and Parameter Optimization of Subcritical Organic Rankine Cycle System for Waste Heat Recovery,” Energy, **88**, pp. 734–745.

[94] Yang, M.-H., and Yeh, R.-H., 2015, “Thermo-Economic Optimization of an Organic Rankine Cycle System for Large Marine Diesel Engine Waste Heat Recovery,” Energy, **82**, pp. 256–268.

[95] Yang, M. H., and Yeh, R. H., 2015, “Thermodynamic and Economic Performances Optimization of an Organic Rankine Cycle System Utilizing Exhaust Gas of a Large Marine Diesel Engine,” Appl. Energy, **149**, pp. 1–12.

[96] Garland, S. D., Bandhauer, T. M., Grauberger, A., Simon, J., Young, D., Fuller, R., Noall, J., Shull, J., Sami, R. V, Reinke, M. J., and Larry, W., 2018, “Experimental Investigation of a Waste Heat Driven Turbo-Compression Chiller,” *3rd Thermal and Fluids Engineering Conference*, Fort Lauderdale.

[97] Bandhauer, T. M., and Garland, S. D., 2016, “Dry Air Turbo-Compression Cooling,” *ASME Power*, Charlotte, p. V001T04A003.

[98] Klein, S. A., 2016, “Engineering Equation Solver (EES).”

[99] Borgnakke, C., and Sonntag, R. E., 2013, *Fundamentals of Thermodynamics*.

[100] Carrier, 2018, “Air-Cooled Chillers” [Online]. Available: https://www.carrier.com/commercial/en/us/products/chillers-components/air-cooled-chillers/.

[101] Airedale, 2018, “Air Condition Chillers” [Online]. Available: http://airedale.com/web/Products/Chillers.htm.

[102] Carrier, 2018, “Water-Cooled Chillers” [Online]. Available: https://www.carrier.com/commercial/en/us/products/chillers-components/water-cooled-chillers/.

[103] Honeywell Refrigerants, 2010, “Working Fluid Developments for HT Heat Pumps and ORC Systems,” *Chillventa*, pp. 1–9.

[104] Dairy Processing Handbook, “Heat Exchangers: The Purposes of Heat Treatment” [Online]. Available: http://dairyprocessinghandbook.com/chapter/heat-exchangers.

[105] Sinnott, R. K., 2005, “Chemical Engineering Design,” Coulson Richardson’s Chem. Eng., **6**, pp. 756–764.

[106] Hewitt, G. F., Shires, G. L., and Bott, T. R., 1994, *Process Heat Transfer*.

[107] Kuo, W. S., Lie, Y. M., Hsieh, Y. Y., and Lin, T. F., 2005, "Condensation Heat Transfer and Pressure Drop of Refrigerant R-410A Flow in a Vertical Plate Heat Exchanger," Int. J. Heat Mass Transf., **48**(25–26), pp. 5205–5220.

[108] Thonon, B., Vidil, R., and Marvillet, C., 1995, *Recent Research and Developments in Plate Heat Exchangers*.

[109] Hsieh, Y. Y., and Lin, T. F., 2002, "Saturated Flow Boiling Heat Transfer and Pressure Drop of Refrigerant R-410A in a Vertical Plate Heat Exchanger," Int. J. Heat Mass Transf., **45**(5), pp. 1033–1044.

[110] Bergman, T. L., Lavine, A. S., Incropera, F. P., and Dewitt, D. P., 2011, *Fundamentals of Heat and Mass Transfer*, John Wiley and Sons, Danvers, MA.

[111] "Minor Loss Coefficients in Pipe and Tube Components" [Online]. Available: http://www.engineeringtoolbox.com/minor-loss-coefficients-pipes-d_626.html.

[112] Perry, R. H., 1997, *Chemical Engineers' Handbook*, McGraw-Hill.

[113] Vatavuk, W. M., 2002, "Updating the CE Plant Cost Index," Chem. Eng. - Eng. Pract.

[114] Brown, T., 2007, *Engineering Economics and Economic Design for Process Engineers*, CRC Press, Boca Raton, FL.

[115] Rieckmann, T., 2009, "German and International Cost Indices."

[116] Chemical Engineering Online, 2017, "CEPCI June 2017 Issue" [Online]. Available: https://www.scribd.com/document/352561651/CEPCI-June-2017-Issue.

[117] Couper, J., Penney, R., Fair, J., and Walas, S., 1990, *Chemical Process Equipment*, Butterworth-Heinemann, Newton, MA.

[118] Gibson, S. C., Young, D., and Bandhauer, T. M., 2017, "Technoeconomic Optimization of Turbocompression Cooling Systems," *International Mechanical Engineering Congress and Exposition*, Tampa Bay, FL.

[119] Dewane, M., 2016, "MEPC 70: IMO Moves Towards Arctic Phase Out of World's Dirtiest Fuel."

[120] Engineering Toolbox, "Fuels - Higher and Lower Calorific Values" [Online]. Available: https://www.engineeringtoolbox.com/fuels-higher-calorific-values-d_169.html.

[121] Ship and Bunker, "World Bunker Prices" [Online]. Available: https://shipandbunker.com/prices#MGO.

[122] Moldanova, J., 2010, *Transport Releated Air Pollution and Health Impacts - Integrated Methodologies for Assessing Particulate Matter*.

[123] Jones, S., Meyer, P., Snowden-Swan, L., Susanne, K. J., Pimphan, M., Snowden-SwanLesley, Asanga, P., Eric, T., Abhijit, D., Jacob, J., Cafferty, Jones, S., Meyer, P., and Snowden-Swan, L., 2013, "Process Design and Economics for the Conversion of Lignocellulosic Biomass to Hydrocarbon Fuels: Fast Pyrolysis and Hydrotreating Bio-Oil Pathway," Energy, (November), p. 97.

[124] Wanniarachchi, A. S., Ratman, U., Tilton, B. E., and Dutta-Roy, K., 1995, "Aproximate Correlations for Chevron-Type Plate Heat Exchangers," *30th National Heat Transfer Conference*, pp. 145–151.

[125] Rosenblad, G., and Kullendorff, A., 1975, "Estimating Heat Transfer Rates from Mass Transfer Studies on Plate Heat Exchanger Surfaces," Wärme - und Stoffübertragung, **8**(3), pp. 187–191.

[126] Heavner, H., Kumar, L., and Wanniarachchci, A. S., 1993, "Performance of an Industrial Plate Heat Exchanger: Effect of Chevron Angle," *AIChE Symposium Ser. Heat Transfer*.

[127] Khan, T. S., Khan, M. S., Chyu, M.-C., and Ayub, Z. H., 2010, "Experimental Investigation

of Single Phase Convective Heat Transfer Coefficient in a Corrugated Plate Heat Exchanger for Multiple Plate Configurations," Appl. Therm. Eng., **30**(8), pp. 1058–1065.

[128] Rajasekaran, S., and Raj, W. C., "Comparative Study of Nusselt Number for a Single Phase Fluid Flow Using Plate Heat Exchanger," Therm. Sci., **20**(A00101s1), pp. 929–935.

APPENDIX A. Representative Calculation for TCCS with R134a

A representative calculation of the power cycle will be given below to verify the accuracy of the solver. Engineering Equation Solver iterates to find the solution to the set of coupled thermodynamic, heat transfer, and economic equations detailed in the above sections. The calculation represents a turbo-compression cooling system with R134a as the working fluid where the system is optimized to have the lowest possible simple payback period for use onboard a large cargo ship. Figure A-1 shows the turbo-compression cooling system with the state points for the power and cooling cycles labeled, while Table A-1 provides the optimized heat exchanger effectiveness values. Table A-2 shows the values for temperature, enthalpy, pressure, and entropy at each state point.

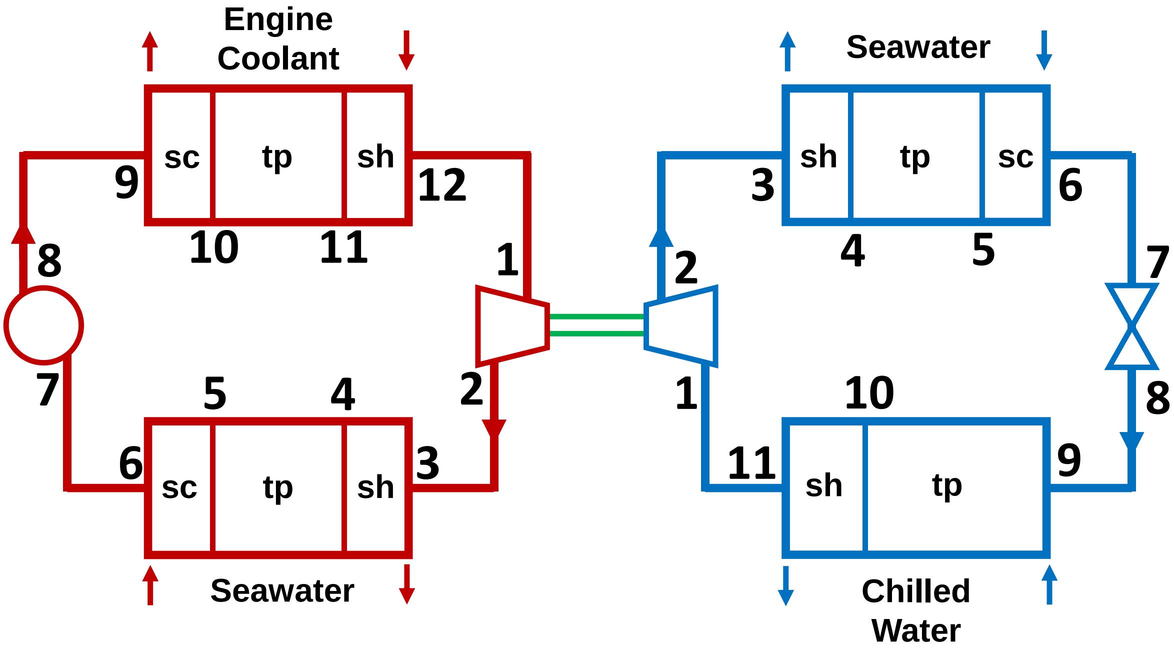

Figure A-1: Process flow diagram of the turbo-compression cooling system with state points designated.

Table A-1: The optimized effectiveness values for each heat exchanger region for the R134a design point.

Cycle	Heat Exchanger	Effectiveness
Power Cycle	Boiler: Subcooled	0.703
	Boiler: Two-phase	0.420
	Boiler: Superheated	0.406
	Condenser: Superheated	0.104
	Condenser: Two-phase	0.174
	Condenser: Subcooled	0.001
Cooling Cycle	Chiller: Two-phase	0.802
	Chiller: Superheated	0.001
	Condenser: Superheated	0.467
	Condenser: Two-phase	0.074
	Condenser: Subcooled	0.485

Table A-2: State points for payback period optimized turbo-compression cooling system with R134a.

R134a	**Cooling Cycle**				**Power Cycle**			
	Temperature	**Enthalpy**	**Pressure**	**Entropy**	**Temperature**	**Enthalpy**	**Pressure**	**Entropy**
	°C	**kJ kg^{-1}**	**kPa**	**kJ kg^{-1} K^{-1}**	**°C**	**kJ kg^{-1}**	**kPa**	**kJ kg^{-1} K^{-1}**
1	5.3	253.5	353	0.9288	84.7	287.4	2699	0.907
2	52.1	283.0	1097	0.9471	43.1	273.3	1077	0.9181
3	52.1	283.0	1096	0.9472	43.1	273.3	1076	0.9182
4	42.8	272.5	1096	0.9143	42.1	272.2	1076	0.9146
5	42.7	112.3	1092	0.4074	42.0	111.2	1072	0.4041
6	37.4	104.4	1092	0.3824	42.0	111.2	1072	0.4041
7	37.4	104.4	1091	0.3824	41.9	111.2	1071	0.4041
8	5.8	104.4	360	0.393	43.4	113.0	2702	0.4052
9	5.8	104.4	359	0.393	43.4	113.0	2701	0.4052
10	5.3	253.5	354	0.9286	81.2	176.5	2701	0.5941
11	5.3	253.5	354	0.9286	81.2	280.4	2700	0.8875
12	-	-	-	0.9286	84.7	287.4	2700	0.907

A.1. Thermodynamic Cycle Calculation

Beginning with the turbine (state points 1 and 2), the turbine work and isentropic efficiency will be confirmed using the enthalpy difference (isentropic and actual) and the mass flow rate, as shown in Equation (A.1) and (A.2):

$$\dot{W}_{\text{turbine}} = \dot{m}_{\text{r}}\left(i_1 - i_2\right) = 11.47\left(287.4 - 273.3\right) = 161.7\ [\text{kW}] \tag{A.1}$$

$$\eta_{\text{s,turb}} = \frac{\left(i_1 - i_2\right)}{\left(i_1 - i_{2,s}\right)} = \frac{\left(287.4 - 273.3\right)}{\left(287.4 - 269.8\right)} = 0.80 \tag{A.2}$$

Moving to state points 3 and 4, the heat duty of the superheated region of the condenser will be confirmed in Equations (A.3) through (A.5):

$$\dot{Q}_{\text{pc,cond,sh}} = \dot{m}_{\text{r}}\left(i_3 - i_4\right) = 11.47\left(273.297 - 272.174\right) = 12.88\ [\text{kW}] \tag{A.3}$$

$$\dot{Q}_{\text{pc,cond,sh}} = \dot{m}_{\text{sw}} c_{\text{sw}}\left(T_{\text{sw,3}} - T_{\text{sw,4}}\right) = 250 \cdot 4.183\left(33.778 - 33.766\right) = 12.55\ [\text{kW}] \tag{A.4}$$

$$\dot{Q}_{\text{pc,cond,sh}} = \varepsilon_{\text{sh}} C_{\min}\left(T_3 - T_{\text{sw,4}}\right) = 0.1042\left(13.35108\right)\left(43.1 - 33.765\right) = 12.99\,[\text{kW}] \tag{A.5}$$

The minor differences in the results of Equations (A.3) through (A.5) result from simple rounding errors. C_{min} in Equation (A.5) was the heat capacity rate of the refrigerant side of the heat exchanger. The two-phase region of the condenser occurs from state points 4 to 5. The heat duty of the two-phase region of the condenser will be confirmed in Equations (A.6) through (A.8):

$$\dot{Q}_{\text{pc,cond,tp}} = \dot{m}_{\text{r}}\left(i_4 - i_5\right) = 11.47\left(272.2 - 111.2\right) = 1847\ [\text{kW}] \tag{A.6}$$

$$\dot{Q}_{\text{pc,cond,tp}} = \dot{m}_{\text{sw}} c_{\text{sw}}\left(T_{\text{sw,4}} - T_{\text{sw,5}}\right) = 250\left(4.183\right)\left(33.766 - 32\right) = 1847\ [\text{kW}] \tag{A.7}$$

$$\dot{Q}_{\text{pc,cond,tp}} = \varepsilon_{\text{tp}} C_{\text{sw}}\left(T_4 - T_{\text{sw,5}}\right) = 0.1744\left(1046\right)\left(42.12 - 32\right) = 1846\ [\text{kW}] \tag{A.8}$$

In Equation (A.8), the specific heat capacity rate of the seawater was taken to be the minimum because the refrigerant is two-phase through this region. When the refrigerant is two-phase, it can absorb an ‘infinite’ amount of heat without rising in temperature, meaning that the specific heat is infinite. Therefore, the seawater side must have the minimum specific heat capacity rate and the ratio of heat capacity rates, C_{ratio}, is zero. From state points 5 to 6, the working fluid is in the subcooled region of the condenser. The subcooled region of the condenser is modeled in Equations (A.9) through (A.11):

$$\dot{Q}_{\mathrm{pc,cond,sc}} = \dot{m}_{\mathrm{r}}\left(i_5 - i_6\right) = 11.47\left(111.225 - 111.210\right) = 0.172\ [\mathrm{kW}] \tag{A.9}$$

$$\dot{Q}_{\mathrm{pc,cond,sc}} = \dot{m}_{\mathrm{sw}} c_{\mathrm{sw}}\left(T_{\mathrm{sw,5}} - T_{\mathrm{sw,6}}\right) = 250\left(4.183\right)\left(32.0001652 - 32\right) = 0.173\,[\mathrm{kW}] \tag{A.10}$$

$$\dot{Q}_{\mathrm{pc,cond,sc}} = \varepsilon_{\mathrm{sc}} C_{\mathrm{min}}\left(T_5 - T_{\mathrm{sw,6}}\right) = 0.001\left(17.32\right)\left(41.98 - 32\right) = 0.173\ [\mathrm{kW}] \tag{A.11}$$

The total heat duty of the power cycle condenser is represented in Equation (A.12):

$$\dot{Q}_{\mathrm{pc,cond}} = \dot{Q}_{\mathrm{pc,cond,sc}} + \dot{Q}_{\mathrm{pc,cond,tp}} + \dot{Q}_{\mathrm{pc,cond,sh}} = 1861\ [\mathrm{kW}] \tag{A.12}$$

The next step in the cycle is pressurizing the subcooled working fluid through the pump, state points 7-8. The work and isentropic efficiency of the pump will be confirmed in Equation (A.13) and (A.14):

$$\dot{W}_{\mathrm{pump}} = \dot{m}_{\mathrm{r}}\left(i_8 - i_7\right) = 11.47\left(113.0 - 111.2\right) = 20.65\,[\mathrm{kW}] \tag{A.13}$$

$$\eta_{\mathrm{s,pump}} = \frac{i_{8,\mathrm{s}} - i_7}{i_8 - i_7} = \frac{112.637 - 111.2}{112.994 - 111.2} = 0.80 \tag{A.14}$$

After pumping, the subcooled working fluid enters the boiler and is heated up to a saturated liquid represented by state points 9 to 10. The heat duty of the subcooled region of the boiler is given in Equations (A.15) through (A.17):

$$\dot{Q}_{\mathrm{pc,boiler,sc}} = \dot{m}_{\mathrm{r}}\left(i_{10} - i_9\right) = 11.47\left(176.46 - 112.994\right) = 727.96\ [\mathrm{kW}] \tag{A.15}$$

$$\begin{aligned}\dot{Q}_{\mathrm{pc,boiler,sc}} = \dot{m}_{\mathrm{b}} c_{\mathrm{b}}\left(T_{\mathrm{b,10}} - T_{\mathrm{b,9}}\right) &= 78.50\left(4.200\right)\left(86.1456322 - 83.9377077\right) \\ &= 727.95\ [\mathrm{kW}]\end{aligned} \tag{A.16}$$

$$\dot{Q}_{\text{pc,boiler,sc}} = \varepsilon C_{\min}\left(T_{\text{b,10}} - T_9\right) = 0.7032\left(24.20\right)\left(86.1456322 - 43.369\right) \\ = 727.95 \text{ [kW]} \tag{A.17}$$

In Equation (A.17), $C_{\min}$ was the specific heat capacity rate of the refrigerant side. From state point 10 to 11, the working fluid is undergoing a phase change from saturated liquid to a saturated vapor. The heat duty in the two-phase region is defined in Equations (A.18) - (A.20):

$$\dot{Q}_{\text{pc,boiler,tp}} = \dot{m}_{\text{r}}\left(i_{11} - i_{10}\right) = 11.47\left(280.4 - 176.5\right) = 1192 \text{ [kW]} \tag{A.18}$$

$$\dot{Q}_{\text{pc,boiler,tp}} = \dot{m}_{\text{b}} c_{\text{b}}\left(T_{\text{b,11}} - T_{\text{b,10}}\right) = 78.50\left(4.204\right)\left(89.76 - 86.15\right) = 1191 \text{ [kW]} \tag{A.19}$$

$$\dot{Q}_{\text{pc,boiler,tp}} = \varepsilon C_b\left(T_{\text{b,11}} - T_{10}\right) = 0.4202\left(329.9\right)\left(89.76 - 81.16\right) = 1192 \text{ [kW]} \tag{A.20}$$

The last region of the boiler, state points 11 to 12, heats the working fluid from a saturated vapor to the superheated region of the vapor dome. The heat duty of the superheated region of the boiler is confirmed in Equations (A.21) through (A.23):

$$\dot{Q}_{\text{pc,boiler,sh}} = \dot{m}_{\text{r}}\left(i_{12} - i_{11}\right) = 11.47\left(287.359 - 280.427\right) = 79.51 \text{ [kW]} \tag{A.21}$$

$$\dot{Q}_{\text{pc,boiler,sh}} = \dot{m}_{\text{b}} c_{\text{b}}\left(T_{\text{b,12}} - T_{\text{b,11}}\right) = 78.50\left(4.204\right)\left(90 - 89.7590921\right) = 79.50 \text{ [kW]} \tag{A.22}$$

$$\dot{Q}_{\text{pc,boiler,sh}} = \varepsilon C_{\min}\left(T_{\text{b,12}} - T_{11}\right) = 0.4061\left(22.12\right)\left(90 - 81.15\right) = 79.50 \text{ [kW]} \tag{A.23}$$

The total heat duty of the boiler is then calculated in Equation (A.24):

$$Q_{\text{boiler}} = Q_{\text{pc,boiler,sc}} + Q_{\text{pc,boiler,tp}} + Q_{\text{pc,boiler,sh}} = 728 + 1192 + 79.5 = 2000 \text{ [kW]} \tag{A.24}$$

The representative calculation of the thermodynamic analysis of the organic Rankine power cycle is now complete. The thermodynamic modeling was completed in the same way for the vapor compression cycle.

The vapor compression cycle representative calculation will begin with the compression of the working fluid to a high pressure. Equations (A.25) and (A.26) will confirm the work and isentropic efficiency of the compressor:

$$\dot{W}_{\text{comp}} = \dot{m}_{\text{cc,r}}\left(i_2 - i_1\right) = 5.198\left(282.975 - 253.517\right) = 153.1\,[\text{kW}] \tag{A.25}$$

$$\eta_{\text{s,comp}} = \frac{\left(i_{2,\text{s}} - i_1\right)}{\left(i_2 - i_1\right)} = \frac{277.083 - 253.517}{282.975 - 253.517} = 0.80 \tag{A.26}$$

The high pressure refrigerant is sent to the condenser. The heat duty of the superheated region of the condenser was confirmed with Equations (A.27) through (A.29):

$$\dot{Q}_{\text{cc,cond,sh}} = \dot{m}_{\text{cc,r}}\left(i_3 - i_4\right) = 5.198\left(282.975 - 272.457\right) = 54.67\ [\text{kW}] \tag{A.27}$$

$$\begin{aligned}\dot{Q}_{\text{cc,cond,sh}} &= \dot{m}_{\text{sw}} c_{\text{sw}}\left(T_{\text{sw,3}} - T_{\text{sw,4}}\right) = 250\left(4.183\right)\left(33.8873360 - 33.8350596\right)\\ &= 54.67\ [\text{kW}]\end{aligned} \tag{A.28}$$

$$\dot{Q}_{\text{pc,cond,sh}} = \varepsilon_{\text{sh}} C_{\min}\left(T_3 - T_{\text{sw,4}}\right) = 0.46472\left(6.084\right)\left(52.07 - 32.8350596\right) = 54.38\,[\text{kW}]$$

(A.29)

The two-phase region of the condenser will be confirmed with Equations (A.30) through (A.32):

$$\dot{Q}_{\text{cc,cond,tp}} = \dot{m}_{\text{r}}\left(i_4 - i_5\right) = 5.198\left(272.457 - 112.285\right) = 832.6\ [\text{kW}] \tag{A.30}$$

$$\begin{aligned}\dot{Q}_{\text{cc,cond,tp}} &= \dot{m}_{\text{sw}} c_{\text{sw}}\left(T_{\text{sw,4}} - T_{\text{sw,5}}\right) = 250\left(4.183\right)\left(32.8350596 - 32.0389948\right)\\ &= 832.5\ [\text{kW}]\end{aligned} \tag{A.31}$$

$$\begin{aligned}\dot{Q}_{\text{cc,cond,tp}} &= \varepsilon_{\text{tp}} C_{\text{sw}}\left(T_4 - T_{\text{sw,5}}\right) = 0.07398\left(1046\right)\left(42.7995279 - 32.0389948\right)\\ &= 832.7\ [\text{kW}]\end{aligned} \tag{A.32}$$

The subcooled region of the condenser is confirmed using Equations (A.33) through (A.35):

$$\dot{Q}_{\text{cc,cond,sc}} = \dot{m}_{\text{r}}\left(i_5 - i_6\right) = 5.198\left(112.285 - 104.439\right) = 40.78\ [\text{kW}] \tag{A.33}$$

$$\begin{aligned}\dot{Q}_{\text{cc,cond,sc}} &= \dot{m}_{\text{sw}} c_{\text{sw}}\left(T_{\text{sw,5}} - T_{\text{sw,6}}\right) = 250\left(4.183\right)\left(32.0389948 - 32\right)\\ &= 40.78\,[\text{kW}]\end{aligned} \tag{A.34}$$

$$\dot{Q}_{\text{cc,cond,sc}} = \varepsilon_{\text{sc}} C_{\min}\left(T_5 - T_{\text{sw,6}}\right) = 0.485\left(7.873\right)\left(42.6802533 - 32\right) = 40.78\ [\text{kW}] \tag{A.35}$$

The cooling duty of the condenser is then confirmed in Equation (A.36):

$$\dot{Q}_{\text{cc,cond}} = \dot{Q}_{\text{cc,cond,sh}} + \dot{Q}_{\text{cc,cond,tp}} + \dot{Q}_{\text{cc,cond,sc}} = 54.67 + 832.7 + 40.78 = 928 \text{ [kW]} \tag{A.36}$$

The subcooled working fluid expands through the isenthalpic expansion valve and enters the evaporator as a two-phase mixture. The cooling duty of the two-phase region in the evaporator will be confirmed in Equations (A.37) through (A.39):

$$\dot{Q}_{\text{chiller,tp}} = \dot{m}_{\text{cc,r}} \left(i_{10} - i_9 \right) = 5.198\left(253.515 - 104.439\right) = 774.9 \text{ [kW]} \tag{A.37}$$

$$\dot{Q}_{\text{chiller,tp}} = \dot{m}_{\text{cw}} c_{\text{cw}} \left(T_{\text{cw,9}} - T_{\text{cw,10}} \right) = 37.02\left(4.186\right)\left(12 - 7.00005223\right) = 774.8 \text{ [kW]} \tag{A.38}$$

$$\dot{Q}_{\text{chiller,tp}} = \varepsilon C_{\text{cw}} \left(T_{\text{cw,9}} - T_9 \right) = 0.8016\left(154.96572\right)\left(12 - 81.16\right) = 774.8 \text{ [kW]} \tag{A.39}$$

The cooling duty of the superheated region of the chiller will be confirmed in Equations (A.40) through (A.42):

$$\dot{Q}_{\text{chiller,sh}} = \dot{m}_{\text{cc,r}} \left(i_{11} - i_{10} \right) = 5.198\left(253.517 - 253.515\right) = 0.01 \text{ [kW]} \tag{A.40}$$

$$\dot{Q}_{\text{chiller,sh}} = \dot{m}_{\text{cw}} c_{\text{cw}} \left(T_{\text{cw,10}} - T_{\text{cw,11}} \right) = 37.02\left(4.194\right)\left(7.00005223\text{-}7\right) = 0.01 \text{ [kW]} \tag{A.41}$$

$$\begin{aligned} \dot{Q}_{\text{chiller,sh}} = \varepsilon C_{\min} \left(T_{\text{b,10}} - T_{10} \right) &= 0.001\left(4.793\right)\left(7.00005223 - 5.30824592\right) \\ &= 0.01 \text{ [kW]} \end{aligned} \tag{A.42}$$

The heat duty of the chiller is then confirmed in Equation (A.43):

$$Q_{\text{chiller}} = Q_{\text{chiller,tp}} + Q_{\text{chiller,sh}} = 774.8 + 0.01 = 774.9 \text{ [kW]} \tag{A.43}$$

The confirmation of the cooling cycle calculations is now complete.

The next step of the modeling effort was to calculate the size and speed of the centrifugal turbocompressor. In this representative calculation, the first step was to set the specific speed, Ns_{turb}, of the turbine to 115 $\text{ft}^{3/4}$ $\text{lbm}^{3/4}$ min^{-1} $\text{s}^{-1/2}$ $\text{lbf}^{-3/4}$. After this, the actual speed of the turbine was calculated, as defined in Equation (A.44):

$$N = \frac{Ns_{\text{turb}} \left(H_{\text{ad,turb}}\right)^{0.75}}{\sqrt{\dot{V}_{\text{turb}}}} = \frac{115\left(5875\right)^{0.75}}{\sqrt{7.658}} = 27{,}887 \text{ [rpm]} \tag{A.44}$$

The adiabatic head, $H_{\text{ad,turb}}$ in this equation has units of ft lbf lbm^{-1}, while the volumetric flow rate, $\dot{V}_{\text{turb}}$, is in ft^3 s^{-1}. By convention, the volumetric flow rate is calculated at the outlet of the turbine where the density of the working fluid is lower than the inlet. Since the turbine and compressor are mechanically coupled, the compressor will also spin at 27,887 rpm. After this, the specific diameter of the turbine was calculated using the Cordier diagram provided by Barber-Nichols, Inc. The equation of line that borders the upper limit of the 80% efficiency island was used to relate specific speed, Ns_{turb}, and specific diameter, Ds_{turb}. The specific diameter was calculated in Equation (A.45):

$$Ds_{\text{turb}} = 2\left(\frac{Ns_{\text{turb}}}{50}\right)^{-0.515} = 2\left(\frac{115}{50}\right)^{-0.515} = 1.30 \text{ [lbf}^{1/4}\text{s}^{1/2}\text{lbm}^{-1/4}\text{ft}^{-1/4}\text{]} \tag{A.45}$$

With the specific diameter calculated, the actual diameter of the turbine was calculated according to Equation (A.46):

$$D_{\text{turb}} = \frac{Ds_{\text{turb}}\sqrt{\dot{V}_{\text{turb}}}}{\left(H_{\text{ad,turb}}\right)^{0.25}} = \frac{1.30\sqrt{7.658}}{\left(5875\right)^{0.25}} = 0.411 \text{ [ft]} = 4.93 \text{ [in]} \tag{A.46}$$

The specific speed of the compressor was calculated using the actual speed of the machine, as shown in Equation (A.47):

$$Ns_{\text{comp}} = \frac{N\sqrt{\dot{V}_{\text{comp}}}}{\left(H_{\text{ad,comp}}\right)^{0.75}} = \frac{27887\sqrt{10.63}}{\left(7883\right)^{0.75}} = 108.7 \text{ [ft}^{3/4}\text{lbm}^{3/4}\text{ min}^{-1}\text{ s}^{-1/2}\text{lbf}^{-3/4}\text{]} \tag{A.47}$$

The calculated specific speed of 108.7 ft$^{3/4}$ lbm$^{3/4}$ min^{-1} s$^{-1/2}$ lbf$^{-3/4}$ falls within the range of the 80% efficiency island. The next step is to calculate the specific diameter of the compressor from the equation of the line that defines the top of the 80% efficiency island. The specific diameter is calculated in Equation (A.48):

$$Ds_{\text{comp}} = 1.75\left(\frac{Ns_{\text{comp}}}{80}\right)^{-0.3802} = 1.75\left(\frac{108.7}{80}\right)^{-0.3802} = 1.56\ [\text{lbf}^{1/4}\text{s}^{1/2}\text{lbm}^{-1/4}\text{ft}^{-1/4}] \tag{A.48}$$

From the specific diameter, the actual diameter of the compressor can be calculated, as shown in Equation (A.49):

$$D_{\text{comp}} = \frac{Ds_{\text{comp}}\sqrt{\dot{V}_{\text{comp}}}}{\left(H_{\text{ad,comp}}\right)^{0.25}} = \frac{1.56\sqrt{10.63}}{\left(7883\right)^{0.25}} = 0.540\ [\text{ft}] = 6.48\ [\text{in}] \tag{A.49}$$

The thermodynamics block of the simulation for a liquid coupled turbo-compression cooling system is now complete. The next step was to determine the size of the plate frame heat exchangers.

A.2. Heat Exchanger Calculations

A representative calculation will be given below for the each heat exchanger to demonstrate the solving method for the heat transfer coefficients, pressure drops, and total heat exchange area. These geometry values were taken from a quote for a two megawatt plate frame heat exchanger.

The power cycle boiler is a counter flow device. In the first region of the power cycle boiler, the working fluid is a subcooled liquid. The first step is to determine the overall heat transfer coefficient of this region. The heat transfer coefficient of the working fluid, the engine coolant, and the wall resistance were determined to find the overall heat transfer coefficient. The heat transfer coefficient of the working fluid was calculated using the Thonon correlation, as shown in Equation (A.50):

$$\begin{aligned} h_{\text{r,E1}} &= 0.2998 Re_{\text{plate}}^{0.645} Pr^{1/3} \frac{k}{D_{\text{hyd}}} = 0.2998\left(1574\right)^{0.645}\left(3.171\right)^{1/3} 8.248 \\ &= 419\ [\text{W m}^{-2}\ \text{K}^{-1}] \end{aligned} \tag{A.50}$$

The heat transfer coefficient of the boiler water is calculated using the Dittus-Boelter correlation as shown in Equation (A.51):

$$h_{\mathrm{w,E1}} = 0.023 Re_{\mathrm{plate}}^{0.8} Pr^{0.3} \frac{k_{\mathrm{l}}}{D_{\mathrm{hyd}}} = 0.023\left(4893\right)^{0.8}\left(2.154\right)^{0.3}\left(73.43\right) \\ = 1902\ [\mathrm{W\,m^{-2}\ K^{-1}}] \tag{A.51}$$

The wall resistance of the plates is calculated according to Equation (A.52):

$$R_{\mathrm{wall}} = \frac{t_{\mathrm{plate}}}{k_{\mathrm{plate,stainless}}} = \frac{0.0007}{13.32} = 5.25 \times 10^{-5}\ [\mathrm{W^{-1}\ m^{2}\ K}] \tag{A.52}$$

Thus, the overall heat transfer coefficient is calculated in Equation (A.53):

$$\frac{1}{U_{\mathrm{E1}}} = \frac{1}{h_{\mathrm{r,E1}}} + R_{\mathrm{wall}} + \frac{1}{h_{\mathrm{w,E1}}} = \frac{1}{417.4} + 5.25\times10^{-5} + \frac{1}{1902} = 336.2\ [\mathrm{W\,m^{-2}\ K^{-1}}] \tag{A.53}$$

The next step is to calculate the number of transfer units (*NTU*) for the subcooled region which depends on the effectiveness of the device and the ratio of heat capacity rates as shown in Equation (A.54):

$$NTU_{\mathrm{pc,E1}} = \frac{1}{C_{\mathrm{r}}-1}\ln\left(\frac{\varepsilon-1}{\varepsilon C_{\mathrm{r}}-1}\right) = \frac{1}{0.05872-1}\ln\left(\frac{0.703-1}{\left(0.703\right)0.05872-1}\right) = 1.243 \tag{A.54}$$

The total area of the subcooled region of the boiler can be found using Equation (A.55), which relates area to heat transfer coefficient and number of transfer units:

$$A_{\mathrm{E1}} = \frac{NTU_{\mathrm{E1}}\left(C_{\mathrm{min,E1}}\right)}{U_{\mathrm{E1}}} = \frac{1.243\left(19350\right)}{336.2} = 71.5\ [\mathrm{m^{2}}] \tag{A.55}$$

The pressure drop of the subcooled region of the boiler was the sum of the inlet header pressure drop, the pressure drop from the fluid traveling from inlet header to channels, and the pressure drop through the channels. The inlet header pressure drop was calculated as follows in Equation (A.56):

$$\begin{aligned}\Delta P_{\text{header}} &= \rho u_{\text{header}}^2\left(\frac{K_{\text{tee,line}}}{2}+2f_{\text{sp}}\frac{L_{\text{header}}}{D_{\text{header}}}\right)\\ &=3.865\left(\frac{0.9}{2}+\left(0.00824\right)\frac{\left(0.8334\right)}{0.35}\right)=1.815\text{ [Pa]}\end{aligned} \tag{A.56}$$

The pressure drop from the header to the working fluid channels was calculated according to Equation (A.57):

$$\Delta P_{\text{tee,in}} = \frac{\left(K_{\text{tee,branch}}+K_{\text{con/exp}}\right)\rho u_{\text{channel}}^2}{2}=\frac{\left(2+0.4726\right)0.7989}{2}=0.9878\text{ [Pa]} \tag{A.57}$$

The length of each region on the plates was calculated with Equation (A.58):

$$L_{\text{sc}} = \frac{A_{\text{sc}}}{\left(N_{\text{plates, boiler}}-1\right)w_{\text{plate}}}=\frac{71.5}{\left(162\right)1.17}=0.377\text{ [m]} \tag{A.58}$$

The pressure drop of the subcooled working fluid flowing through the plates was calculated with Equation (A.59):

$$\Delta P_{\text{plate}} = \frac{2f_{\text{Fanning}}\rho u_{\text{channel}}^2 L_{\text{sc}}}{D_{\text{h,channel}}}=2\left(0.193\right)\frac{919.3\left(0.02948\right)^2 0.3798}{0.008966}=13.1\text{ [Pa]} \tag{A.59}$$

The total pressure drop in the subcooled region of the boiler is then calculated in Equation (A.60):

$$\Delta P_{\text{E1}} = \Delta P_{\text{header}}+\Delta P_{\text{tee,in}}+\Delta P_{\text{channel}}=1.815+0.9878+13.1=15.9\text{ [Pa]} \tag{A.60}$$

In the second region of the boiler, the working fluid is changing phase from a saturated liquid to a saturated vapor. Similar to the subcooled region, the first step was to calculate the overall heat transfer coefficient. After that, the number of transfer units was calculated. Finally, the overall heat transfer coefficient and number of transfer units are related to the total heat transfer area. The Hsieh correlation was used to determine the heat transfer coefficient of the boiling refrigerant, as shown in Equation (A.61):

$$h_{\mathrm{r,E2}} = h_{\mathrm{r,l}}\left(88Bo^{0.5}\right) = 887.7\left(88 \cdot \left(0.003409\right)^{0.5}\right) = 4561\ [\mathrm{W\,m^{-2}\,K^{-1}}] \tag{A.61}$$

To calculate the engine coolant heat transfer coefficient, the Dittus-Boelter correlation was used as shown in Equation (A.62):

$$\begin{aligned} h_{\mathrm{w,E2}} &= 0.023Re_{\mathrm{plate}}^{0.8}Pr^{0.3}\frac{k_{\mathrm{l}}}{D_{\mathrm{hyd}}} \\ &= 0.023\left(5024\right)^{0.8}\left(2.095\right)^{0.3}\left(73.56\right) \\ &= 1930\ [\mathrm{W\,m^{-2}\,K^{-1}}] \end{aligned} \tag{A.62}$$

The wall resistance was found to be the same value as Equation (A.52). Thus, the overall heat transfer coefficient of the two-phase region of the boiler was calculated in Equation (A.63):

$$\frac{1}{U_{\mathrm{E2}}} = \frac{1}{h_{\mathrm{r,E2}}} + R_{\mathrm{wall}} + \frac{1}{h_{\mathrm{w,E2}}} = \frac{1}{4561} + 5.250\times10^{-5} + \frac{1}{1930} = 1266\ [\mathrm{W\,m^{-2}\,K^{-1}}] \tag{A.63}$$

After this, the number of transfer units required for the two-phase region of the boiler was calculated according to Equation (A.64):

$$NTU_{\mathrm{pc,E2}} = -\ln\left(1-\varepsilon\right) = -\ln\left(1-0.4202\right) = 0.5451 \tag{A.64}$$

The area of the two-phase region of the boiler was calculated using Equation (A.65):

$$A_{\mathrm{E2}} = \frac{NTU_{\mathrm{E2}}\left(C_{\mathrm{min,E2}}\right)}{U_{\mathrm{E2}}} = \frac{0.5451\left(330014\right)}{1266} = 142.1\ [\mathrm{m^2}] \tag{A.65}$$

The pressure drop in the two-phase region was calculated using the Hsieh friction factor. The Hsieh friction factor was determined in Equation (A.66):

$$f_{\mathrm{tp,boil}} = 61000Re_{\mathrm{eq}}^{-1.25} = 61000\left(4680\right)^{-1.25} = 1.576 \tag{A.66}$$

The length of the two-phase region of the boiler plates was calculated with Equation (A.67):

$$L_{\mathrm{tp}} = \frac{A_{\mathrm{tp}}}{\left(N_{\mathrm{plates}}-1\right)w_{\mathrm{plate}}} = \frac{142.1}{(162)1.17} = 0.750\ [\mathrm{m}] \tag{A.67}$$

The pressure drop in the two-phase region was calculated with Equation (A.68):

$$\Delta P_{\mathrm{boil}} = \frac{2 f_{\mathrm{tp}} G^2}{\rho_{\mathrm{mean}}} \frac{L_{\mathrm{tp}}}{D_{\mathrm{h,channel}}} = \frac{2\left(1.576\right)27.1^2}{274.123} \frac{\left(0.754\right)}{0.008966} = 710.2 \text{ [Pa]} \qquad \text{(A.68)}$$

In the third region of the heat exchanger, the working fluid is a superheated vapor. To calculate the area required in this region, the overall heat transfer and the number of transfer units were calculated. The heat transfer coefficient of the superheated vapor was calculated using the Thonon Correlation, as shown in Equation (A.69):

$$h_{\mathrm{r,E3}} = 0.2998 Re_{\mathrm{plate}}^{0.645} Pr^{1/3} \frac{k}{D_{\mathrm{hyd}}} = 0.7206\left(15000\right)^{0.645}\left(1.572\right)^{1/3} = 413.8 \text{ [W m}^{-2}\text{ K}^{-1}\text{]} \qquad \text{(A.69)}$$

As discussed in the heat exchanger modeling section, the Reynolds number in this region was set to 15,000 which is the upper limit of the Thonon correlation. If the Reynolds number was not set, it often exceeded 15,000 which was unrealistic based on the other heat exchanger calculations and a survey of available literature. The heat transfer coefficient of the boiler water in this region was determined by the Dittus-Boelter correlation, shown in Equation (A.70):

$$h_{\mathrm{w,E3}} = 0.023 Re_{\mathrm{plate}}^{0.8} Pr^{0.3} \frac{k_{\mathrm{l}}}{D_{\mathrm{hyd}}} = 0.023\left(5254\right)^{0.8}\left(2.000\right)^{0.3}\left(73.76\right) = 1978 \text{ [W m}^{-2}\text{ K}^{-1}\text{]}$$

(A.70)

The wall resistance was calculated to be the same as Equation (A.52). Thus, the overall heat transfer coefficient in the superheated region of the boiler was calculated in Equation (A.71):

$$\frac{1}{U_{\mathrm{E3}}} = \frac{1}{h_{\mathrm{r,E3}}} + R_{\mathrm{wall}} + \frac{1}{h_{\mathrm{w,E3}}} = \frac{1}{413.8} + 5.250\times10^{-5} + \frac{1}{1978} = 336.2 \text{ [W m}^{-2}\text{ K}^{-1}\text{]} \qquad \text{(A.71)}$$

The number of transfer units for the superheated region of the boiler was calculated according to Equation (A.72):

$$NTU_{\mathrm{pc,E3}} = \frac{1}{C_{\mathrm{r}} - 1} \ln\left(\frac{\varepsilon - 1}{\varepsilon C_{\mathrm{r}} - 1}\right) = \frac{1}{0.07614 - 1} \ln\left(\frac{0.4061 - 1}{\left(0.4061\right)0.07614 - 1}\right) = 0.5300 \qquad \text{(A.72)}$$

Thus, the area of the superheated region was calculated in Equation (A.73):

$$A_{\text{E3}} = \frac{NTU_{\text{E3}}\left(C_{\text{min,E3}}\right)}{U_{\text{E3}}} = \frac{0.5300\left(22120\right)}{336.2} = 34.9\ [\text{m}^2] \tag{A.73}$$

The pressure drop in the superheated region of the boiler was modeled as the sum of the outlet header pressure drop, the pressure drop from the channels to the header, and the pressure drop of the superheated vapor flowing through the plate channels. The pressure drop of the outlet header was calculated using Equation (A.74):

$$\begin{aligned} \Delta P_{\text{header}} &= \rho u_{\text{header}}^2 \left(\frac{K_{\text{tee,line}}}{2} + 2 f_{\text{sp}} \frac{L_{\text{header}}}{D_{\text{header}}} \right) \\ &= 22.06 \left(\frac{0.9}{2} + \left(0.00469\right) \frac{\left(0.8334\right)}{0.35} \right) = 10.17\ [\text{Pa}] \end{aligned} \tag{A.74}$$

The pressure drop from the working fluid leaving the channels and entering the header is calculated with Equation (A.75):

$$\Delta P_{\text{tee,out}} = \frac{\left(K_{\text{tee,branch}} + K_{\text{exp}}\right) \rho u_{\text{channel}}^2}{2} = \left(2 + 0.8935\right)\left(\frac{4.56}{2}\right) = 6.598\ [\text{Pa}] \tag{A.75}$$

The length of the superheated region in the boiler is calculated with Equation (A.76):

$$L_{\text{sh}} = \frac{A_{\text{sh}}}{\left(N_{\text{plates}} - 1\right) w_{\text{plate}}} = \frac{34.9}{\left(162\right)1.17} = 0.184\ [\text{m}] \tag{A.76}$$

The pressure drop of the superheated vapor flowing through the plate channels was calculated with Equation (A.77):

$$\Delta P_{\text{channel}} = \frac{2 f_{\text{Fanning}} \rho u_{\text{channel}}^2 L_{\text{sp}}}{D_{\text{h,channel}}} = 2\left(0.1312\right) \frac{161\left(0.1683\right)^2 \left(0.185\right)}{0.008966} = 24.7\ [\text{Pa}] \tag{A.77}$$

The total pressure drop in the superheated vapor region is then calculated in Equation (A.78):

$$\Delta P_{\text{E3}} = \Delta P_{\text{header}} + \Delta P_{\text{tee,out}} + \Delta P_{\text{channel}} = 10.17 + 6.598 + 24.7 = 41.4\ [\text{Pa}] \tag{A.78}$$

The overall pressure drop through the power cycle boiler is calculated with Equation (A.79):

$$\Delta P_{\mathrm{E}} = \Delta P_{\mathrm{E1}} + \Delta P_{\mathrm{E2}} + \Delta P_{\mathrm{E3}} = 15.9 + 710.2 + 41.4 = 768\ [\mathrm{Pa}] = 0.768\ [\mathrm{kPa}] \tag{A.79}$$

The total area of the power cycle boiler is then calculated with Equation (A.80):

$$A_{\mathrm{total,boiler}} = A_{\mathrm{sc}} + A_{\mathrm{tp}} + A_{\mathrm{sh}} = 71.5 + 142.1 + 34.9 = 248.5\ [\mathrm{m}^2] \tag{A.80}$$

The number of plates for the power cycle boiler is calculated with Equation (A.81):

$$N_{\mathrm{plates}} - 1 = \frac{A_{\mathrm{total,HX}}}{A_{\mathrm{plate}}} = 1 + \frac{245.8}{1.544} = 161.8 = 162\ \text{Plates} \tag{A.81}$$

The power cycle condenser representative calculation will be demonstrated next. The heat transfer coefficient of the superheated refrigerant in the power cycle condenser is calculated in Equation (A.82):

$$\begin{aligned} h_{\mathrm{pc,r,C1}} &= 0.2998 Re_{\mathrm{plate}}^{0.645} Pr^{1/3} \frac{k}{D_{\mathrm{hyd}}} = 0.2998(15000)^{0.645}(0.9121)^{1/3}(1.821) \\ &= 261.5\ [\mathrm{W\ m^{-2}\ K^{-1}}] \end{aligned} \tag{A.82}$$

The water side heat transfer coefficient was calculated with Equation (A.83):

$$h_{\mathrm{w,C1}} = 0.023 Re_{\mathrm{plate}}^{0.8} Pr^{0.4} \frac{k_{\mathrm{l}}}{D_{\mathrm{hyd}}} = 0.023(5643)^{0.8}(5.068)^{0.4}(67.90) = 2997\ [\mathrm{W\,m^{-2}\ K^{-1}}] \tag{A.83}$$

Thus, the overall heat transfer coefficient is determined in Equation (A.84):

$$\frac{1}{U_{\mathrm{pc,C1}}} = \frac{1}{h_{\mathrm{pc,r,C1}}} + R_{\mathrm{wall}} + \frac{1}{h_{\mathrm{pc,w,C1}}} = \frac{1}{261.5} + 3.17\times10^{-5} + \frac{1}{2997} = 238.7\ [\mathrm{W\ m^{-2}\ K^{-1}}] \tag{A.84}$$

Then, the number of transfer units for this region was calculated using Equation (A.85):

$$NTU_{\mathrm{pc,C1}} = \frac{1}{C_{\mathrm{r}} - 1}\ln\left(\frac{\varepsilon - 1}{\varepsilon C_{\mathrm{r}} - 1}\right) = \frac{1}{0.01277 - 1}\ln\left(\frac{0.1035 - 1}{(0.1035)0.01277 - 1}\right) = 0.1093 \tag{A.85}$$

The total area of the superheated region of the condenser is calculated with Equation (A.86):

$$A_{\text{pc,C1}} = \frac{\left(NTU_{\text{pc,C1}}\right)C_{\min}}{U_{\text{pc,C1}}} = \frac{\left(0.1093\right)13354}{238.7} = 6.11\,[\text{m}^2] \tag{A.86}$$

The pressure drop in the superheated region of the condenser was the sum of the inlet header pressure drop, the pressure drop from the channels to the header, and the pressure drop of the superheated vapor flowing through the plate channels. The pressure drop of the outlet header was calculated using Equation (A.74):

$$\begin{aligned}\Delta P_{\text{header}} &= \rho u_{\text{header}}^2\left(\frac{K_{\text{tee,line}}}{2} + 2\,f_{\text{sp}}\,\frac{L_{\text{header}}}{D_{\text{header}}}\right)\\ &= 66.8\left(\frac{0.9}{2} + \left(0.00221\right)\frac{\left(1.057\right)}{0.35}\right) = 30.5\,[\text{Pa}]\end{aligned} \tag{A.87}$$

The pressure drop from the working fluid leaving header and entering the channels is calculated with Equation (A.75):

$$\Delta P_{\text{tee,out}} = \frac{\left(K_{\text{tee,branch}} + K_{\text{con}}\right)\rho u_{\text{channel}}^2}{2} = \left(2 + 0.4726\right)\left(\frac{8.61}{2}\right) = 10.64\,[\text{Pa}] \tag{A.88}$$

The length of the superheated region in the condenser is calculated with Equation (A.76):

$$L_{\text{sh}} = \frac{A_{\text{sh}}}{\left(N_{\text{plates}} - 1\right)w_{\text{plate}}} = \frac{6.11}{\left(205\right)1.17} = 0.025\,[\text{m}] \tag{A.89}$$

The pressure drop of the superheated vapor flowing through the plate channels was calculated with Equation (A.77):

$$\Delta P_{\text{channel}} = \frac{2\,f_{\text{Fanning}}\,\rho u_{\text{channel}}^2 L_{\text{sp}}}{D_{\text{h,channel}}} = 2\left(0.1312\right)\frac{53.22\left(0.402\right)^2\left(0.025\right)}{0.008966} = 6.4\,[\text{Pa}] \tag{A.90}$$

The total pressure drop in the superheated vapor region of the power cycle condenser is then calculated in Equation (A.78):

$$\Delta P_{\text{C1}} = \Delta P_{\text{header}} + \Delta P_{\text{tee,out}} + \Delta P_{\text{channel}} = 30.5 + 10.64 + 6.4 = 47.54\,[\text{Pa}] = 0.048\,[\text{kPa}] \tag{A.91}$$

In the next region of the condenser, the working fluid is a two-phase mixture. The heat transfer coefficient was calculated using the Kuo correlation for condensing refrigerants in plate heat exchangers, as shown in Equation (A.92):

$$\begin{aligned} h_{\text{r,cond}} &= h_{\text{r,l}}\left[0.25Co^{-0.45}Fr_{\text{l}}^{0.25}+75Bo^{0.75}\right]=655\left[0.24981+1.06\right] \\ &= 857.9\text{ [W m}^{-2}\text{ K}^{-1}\text{]} \end{aligned} \tag{A.92}$$

The water side heat transfer coefficient was calculated with Equation (A.93):

$$h_{\text{w,C2}} = 0.023Re_{\text{plate}}^{0.8}Pr^{0.4}\frac{k_{\text{l}}}{D_{\text{hyd}}} = 0.023\left(5442\right)^{0.8}\left(5.28\right)^{0.4}\left(67.60\right) = 2946.7\text{ [W m}^{-2}\text{ K}^{-1}\text{]}$$

(A.93)

The overall heat transfer coefficient in this region is then calculated with Equation (A.94):

$$\frac{1}{U_{\text{pc,C2}}} = \frac{1}{h_{\text{r,cond}}} + R_{\text{wall}} + \frac{1}{h_{\text{pc,w,C2}}} = \frac{1}{857.9} + 3.17\times10^{-5} + \frac{1}{2946.7} = 650.8\text{ [W m}^{-2}\text{ K}^{-1}\text{]} \tag{A.94}$$

The NTU of the two-phase region is then defined in Equation (A.95):

$$NTU_{\text{pc,C2}} = -\ln\left(1-\varepsilon\right) = -\ln\left(1-0.1744\right) = 0.1916 \tag{A.95}$$

The area of the two-phase condenser heat region is calculated with Equation (A.96):

$$A_{\text{pc,C2}} = \frac{NTU_{\text{pc,C2}}\left(C_{\text{water}}\right)}{U_{\text{pc,C2}}} = \frac{0.1916\left(1.046\times10^{6}\right)}{650.8} = 308\text{ [m}^{2}\text{]} \tag{A.96}$$

The pressure drop of this region will be calculated next. The Kuo Friction factor for this region is calculated with Equation (A.97):

$$f_{\text{tp,cond}} = 21500Re_{eq}^{-1.14}Bo^{-0.085} = 21500\left(9.30\times10^{-5}\right)\left(1.621\right) = 3.24 \tag{A.97}$$

The length of the two-phase region was calculated with Equation (A.98):

$$L_{\text{tp}} = \frac{A_{\text{tp}}}{\left(N_{\text{plates}}-1\right)w_{\text{plate}}} = \frac{308}{\left(205\right)1.17} = 1.28\text{ [m]} \tag{A.98}$$

Then, the two-phase pressure drop is calculated with Equation (A.99):

$$\Delta P_{\text{tp}} = \frac{2 f_{\text{tp}} G^2}{\rho} \frac{L_{\text{tp}}}{D_{\text{h,channel}}} = 2\left(3.24\right)\frac{458.3881}{101.6880212}\left(\frac{1.28}{0.008966}\right) \tag{A.99}$$
$$= 4183 \text{ [Pa]} = 4.183 \text{ [kPa]}$$

In the third region of the condenser, the working fluid is a subcooled liquid. The heat transfer coefficient of the working fluid is calculated with Equation (A.100):

$$h_{\text{pc,r,C3}} = 0.2998 Re_{\text{plate}}^{0.645} Pr^{1/3} \frac{k}{D_{\text{hyd}}} = 0.2998\left(1221\right)^{0.645}\left(3.178\right)^{1/3}\left(8.3304\right) \tag{A.100}$$
$$= 353.4 \text{ [W m}^{-2}\text{ K}^{-1}\text{]}$$

The water side heat transfer coefficient was calculated with Equation(A.101):

$$h_{\text{w,C3}} = 0.023 Re_{\text{plate}}^{0.8} Pr^{0.4} \frac{k_{\text{l}}}{D_{\text{hyd}}} = 0.023\left(5442\right)^{0.8}\left(5.28\right)^{0.4}\left(67.60\right) = 2947 \text{ [W m}^{-2}\text{ K}^{-1}\text{]}$$

(A.101)

Thus, the overall heat transfer coefficient is determined in Equation (A.102):

$$\frac{1}{U_{\text{pc,C3}}} = \frac{1}{h_{\text{pc,r,C3}}} + R_{\text{wall}} + \frac{1}{h_{\text{pc,w,C3}}} = \frac{1}{353.4} + 3.17\times10^{-5} + \frac{1}{2947} = 312.4 \text{ [W m}^{-2}\text{ K}^{-1}\text{]} \tag{A.102}$$

Then, the number of transfer units for the subcooled region is calculated in Equation (A.103):

$$NTU_{\text{pc,C3}} = \frac{1}{C_{\text{r}} - 1}\ln\left(\frac{\varepsilon - 1}{\varepsilon C_{\text{r}} - 1}\right) = \frac{1}{0.01657 - 1}\ln\left(\frac{0.001 - 1}{\left(0.001\right)0.01657 - 1}\right) = 0.001 \tag{A.103}$$

The area of this region is computed in Equation (A.104):

$$A_{\text{pc,C3}} = \frac{NTU_{\text{pc,C3}}\left(C_{\text{ref}}\right)}{U_{\text{pc,C3}}} = \frac{0.001\left(17324\right)}{312} = 0.055 \text{ [m}^2\text{]} \tag{A.104}$$

The pressure drop in the subcooled region of the condenser was modeled as the sum of the outlet header pressure drop, the pressure drop from the channels to the header, and the pressure drop of the subcooled vapor flowing through the plate channels. The pressure drop of the outlet header was calculated using Equation (A.74):

$$\Delta P_{\text{header}} = \rho u_{\text{header}}^2 \left(\frac{K_{\text{tee,line}}}{2} + 2 f_{\text{sp}} \frac{L_{\text{header}}}{D_{\text{header}}} \right) = 3.12\left(\frac{0.9}{2} + \left(0.008278\right)\frac{\left(1.057\right)}{0.35} \right) = 1.48\ [\text{Pa}] \tag{A.105}$$

The pressure drop from the working fluid leaving the channels and entering the header is calculated with Equation (A.75):

$$\Delta P_{\text{tee}} = \frac{\left(K_{\text{tee,branch}} + \text{K}_{\text{exp}}\right)\rho u_{\text{channel}}^2}{2} = \left(2 + 0.8935\right)\left(\frac{0.4026}{2}\right) = 0.583\ [\text{Pa}] \tag{A.106}$$

The length of the subcooled region in the condenser is calculated with Equation (A.76):

$$L_{\text{sc}} = \frac{A_{\text{sc}}}{\left(N_{\text{plates}} - 1\right) w_{\text{plate}}} = \frac{0.05463}{\left(205\right)1.17} = 2.28\times10^{-4}\ [\text{m}] \tag{A.107}$$

The pressure drop of the subcooled liquid flowing through the plate channels was calculated with Equation (A.77):

$$\Delta P_{\text{channel}} = \frac{2 f_{\text{Fanning}} \rho u_{\text{channel}}^2 L_{\text{sp}}}{D_{\text{h,channel}}} = 2\left(0.2019\right)\frac{1138\left(0.402\right)^2\left(2.28\times10^{-4}\right)}{0.008966} = 0.004\ [\text{Pa}] \tag{A.108}$$

The total pressure drop in the subcooled region of the power cycle condenser is then calculated in Equation (A.78):

$$\Delta P_{\text{C3}} = \Delta P_{\text{header}} + \Delta P_{\text{tee,out}} + \Delta P_{\text{channel}} = 1.48 + 0.583 + 0.004 = 2.1\ [\text{Pa}] = 0.0021\ [\text{kPa}] \tag{A.109}$$

The overall pressure drop through the power cycle condenser is calculated with Equation (A.79):

$$\Delta P_{\text{C}} = \Delta P_{\text{C1}} + \Delta P_{\text{C2}} + \Delta P_{\text{C3}} = 48.04 + 4183 + 2.1 = 4233\ [\text{Pa}] = 4.23\ [\text{kPa}] \tag{A.110}$$

The total area of the power cycle condenser is then calculated with Equation (A.80):

$$A_{\text{total,C}} = A_{\text{sh}} + A_{\text{tp}} + A_{\text{sc}} = 6.15 + 308 + 0.055 = 314.2\ [\text{m}^2] \tag{A.111}$$

The number of plates for the power cycle condenser is calculated with Equation (A.81):

$$N_{\text{plates}} - 1 = \frac{A_{\text{total,C}}}{A_{\text{plate}}} = 1 + \frac{314.2}{1.544} = 204.5 = 205 \text{ Plates} \tag{A.112}$$

The cooling cycle evaporating heat exchanger will be presented next. The working fluid enters the chiller as a two-phase mixture. The heat transfer coefficient of the refrigerant side is calculated with the Hsieh boiling heat transfer correlation, as shown in Equation (A.113):

$$h_{\text{cc,r,E1}} = h_{\text{r,l}}\left(88Bo^{0.5}\right) = 649.3\left(88 \cdot \left(0.003409\right)^{0.5}\right) = 3336\ [\text{W m}^{-2}\ \text{K}^{-1}] \tag{A.113}$$

The heat transfer coefficient of the water was calculated with the Thonon correlation because the Reynolds number was less than 1000, defined in Equation (A.114):

$$\begin{aligned} h_{\text{cc,w,E1}} &= 0.2998 Re_{\text{plate}}^{0.645} Pr^{1/3} \frac{k}{D_{\text{hyd}}} = 0.2998\left(954\right)^{0.645}\left(9.048\right)^{1/3}\left(63.71\right) \\ &= 3324\ [\text{W m}^{-2}\ \text{K}^{-1}] \end{aligned} \tag{A.114}$$

Then, the overall heat transfer coefficient was calculated using Equation (A.115):

$$\frac{1}{U_{\text{cc,E1}}} = \frac{1}{h_{\text{cc,r,E1}}} + R_{\text{wall}} + \frac{1}{h_{\text{cc,w,E1}}} = \frac{1}{3336} + 5.25\times10^{-5} + \frac{1}{3324} = 1531\ [\text{W m}^{-2}\ \text{K}^{-1}] \tag{A.115}$$

The number of transfer units for the two-phase region of the chiller was then calculated with Equation (A.116):

$$NTU_{\text{cc,E1}} = -\ln\left(1-\varepsilon\right) = -\ln\left(1-0.8016\right) = 1.617 \tag{A.116}$$

The total area of the two-phase chiller is calculated in Equation (A.117):

$$A_{\text{cc,E1}} = \frac{NTU_{\text{cc,E1}}\left(C_{\text{water}}\right)}{U_{\text{cc,E1}}} = \frac{1.617\left(154969\right)}{1531} = 163.7\ [\text{m}^2] \tag{A.117}$$

The pressure drop of the two-phase region in the chiller was modeled as the sum of the inlet header pressure drop, the pressure drop from the header to the channels, and the pressure drop from the two-phase mixture flowing through the plate channels. The homogeneous method was used to calculate the density and viscosity, as shown in Equation (A.118) and (A.119):

$$\rho_{\text{hom}} = x\rho_{\text{v}} + (1-x)\rho_{\text{l}} = 0.2307(17.59) + 0.7693(1275) = 985 \text{ [kg m}^{-3}\text{]} \tag{A.118}$$

$$\begin{aligned}\mu_{\text{hom}} &= x\mu_{\text{v}} + (1-x)\mu_{\text{l}} = 0.2307\left(1.12\times10^{-5}\right) + 0.7693\left(2.47\times10^{-4}\right)\\ &= 1.93\times10^{-4} \text{ [kg m}^{-1}\text{ s}^{-1}\text{]}\end{aligned} \tag{A.119}$$

The pressure drop in the header was calculated with Equation (A.120):

$$\begin{aligned}\Delta P_{\text{header}} &= \frac{K_{\text{tee,line}}}{2}\rho_{\text{hom}}u_{\text{header}}^{2} + 2f_{\text{sp}}\frac{G^{2}}{\rho_{\text{hom}}}\frac{L_{\text{header}}}{D_{\text{header}}}\\ &= \frac{0.9}{2}(985.2)0.05483^{2} + 2(0.004462)\frac{\left(54.02^{2}\right)}{985.2}\frac{0.5526}{0.350}\\ &= 1.375 \text{ [Pa]}\end{aligned} \tag{A.120}$$

The pressure drop from the flow branching into the channels from the inlet header is calculated in Equation (A.121):

$$\begin{aligned}\Delta P_{\text{tee}} &= \frac{\left(K_{\text{tee,branch}} + \text{K}_{\text{con}}\right)\rho_{\text{hom}}u_{\text{channel}}^{2}}{2} = (2+0.4726)\left(\frac{989.14}{2}\right)\\ &= 1223 \text{ [Pa]} = 1.223 \text{ [kPa]}\end{aligned} \tag{A.121}$$

The Hsieh friction factor was calculated with Equation (A.122), the length of the two-phase region was calculated with Equation (A.123), and then the pressure drop from the two-phase mixture flowing through the plates was calculated with Equation (A.124):

$$f_{\text{tp,boil}} = 61000Re_{\text{eq}}^{-1.25} = 61000(4918)^{-1.25} = 1.481 \tag{A.122}$$

$$L_{\text{tp}} = \frac{A_{\text{tp}}}{\left(N_{\text{plates}}-1\right)w_{\text{plate}}} = \frac{163.7}{(107)1.17} = 1.308 \text{ [m]} \tag{A.123}$$

$$\begin{aligned}\Delta P_{\text{boil}} &= \frac{2f_{\text{tp}}G^{2}}{\rho_{\text{mean}}}\frac{L_{\text{tp}}}{D_{\text{h,channel}}} = \frac{2(1.481)18.62^{2}}{34.2}\frac{(1.308)}{0.008966}\\ &= 4381 \text{ [Pa]} = 4.38 \text{ [kPa]}\end{aligned} \tag{A.124}$$

The total pressure drop of the two-phase region is then calculated in Equation (A.125):

$$\begin{aligned}\Delta P_{\text{CC,E1}} &= \Delta P_{\text{header}} + \Delta P_{\text{tee}} + \Delta P_{\text{channel}} = 1.375 + 1223 + 4381\\ &= 5605 \text{ [Pa]} = 5.605 \text{ [kPa]}\end{aligned} \tag{A.125}$$

The heat transfer coefficient of the refrigerant side of the superheated region of the chiller is calculated with Equation (A.126):

$$h_{\mathrm{cc,r,E2}} = 0.2998 Re_{\mathrm{plate}}^{0.645} Pr^{1/3} \frac{k}{D_{\mathrm{hyd}}} = 0.2998\left(15000\right)^{0.645}\left(0.8135\right)^{1/3}\left(1.40754\right) \\ = 194.5 \text{ [W m}^{-2}\text{ K}^{-1}\text{]} \tag{A.126}$$

The heat transfer coefficient of the water side was calculated with Equation (A.127):

$$h_{\mathrm{cc,w,E2}} = 0.2998 Re_{\mathrm{plate}}^{0.645} Pr^{1/3} \frac{k}{D_{\mathrm{hyd}}} = 0.2998\left(825\right)^{0.645}\left(10.66\right)^{1/3}\left(62.6\right) \\ = 3141 \text{ [W m}^{-2}\text{ K}^{-1}\text{]} \tag{A.127}$$

The overall heat transfer coefficient is calculated in Equation (A.128):

$$\frac{1}{U_{\mathrm{cc,E2}}} = \frac{1}{h_{\mathrm{cc,r,E2}}} + R_{\mathrm{wall}} + \frac{1}{h_{\mathrm{cc,w,E2}}} = \frac{1}{194.5} + 5.25\times10^{-5} + \frac{1}{3141} = 181.4 \text{ [W m}^{-2}\text{ K}^{-1}\text{]} \tag{A.128}$$

The number of transfer units for the superheated region of the chiller is calculated with Equation (A.129):

$$NTU_{\mathrm{cc,E2}} = -\frac{\ln\left[1-\varepsilon\left(1+Cr\right)\right]}{1+Cr} = -\frac{\ln[1-0.001(1.004572)]}{1.004572} = 0.001 \text{ [m}^2\text{]} \tag{A.129}$$

Then, the area of the superheated chiller region was calculated using Equation (A.130):

$$A_{\mathrm{cc,E2}} = \frac{NTU_{\mathrm{cc,E2}}\left(C_{\mathrm{ref}}\right)}{U_{\mathrm{cc,E2}}} = \frac{0.001(4793)}{181.4} = 0.0264 \text{ [m}^2\text{]} \tag{A.130}$$

The pressure drop through the superheated region of the chiller is the sum of the outlet header pressure drop, the pressure drop from the flow leaving the plate channels and entering the outlet header, and the pressure drop from the flow through the plates. The outlet header pressure drop is calculated in Equation (A.131):

$$\begin{aligned}\Delta P_{\text{header}} &= \rho u_{\text{header}}^2\left(\frac{K_{\text{tee,line}}}{2}+2f_{\text{sp}}\frac{L_{\text{header}}}{D_{\text{header}}}\right)\\ &= 41.5\left(\frac{0.9}{2}+\left(0.008758\right)\frac{\left(0.5526\right)}{0.35}\right)=19.3\ [\text{Pa}]\end{aligned} \tag{A.131}$$

The pressure drop from the flow entering the outlet header is calculated with Equation (A.132):

$$\Delta P_{\text{tee}} = \frac{\left(K_{\text{tee,branch}}+\text{K}_{\text{exp}}\right)\rho u_{\text{channel}}^2}{2} = \left(2+0.8935\right)\left(\frac{19.7}{2}\right) = 28.54\ [\text{Pa}] \tag{A.132}$$

The length of the superheated region is calculated in Equation (A.133) and the pressure drop from the flow through the channels is calculated in Equation (A.134):

$$L_{\text{sh}} = \frac{A_{\text{sh}}}{\left(N_{\text{plates}}-1\right)w_{\text{plate}}} = \frac{0.02643}{\left(107\right)1.17} = 2.11\times10^{-4}\ [\text{m}] \tag{A.133}$$

$$\begin{aligned}\Delta P_{\text{channel}} &= \frac{2f_{\text{Fanning}}\rho u_{\text{channel}}^2 L_{\text{sh}}}{D_{\text{h,channel}}} = 2\left(0.1312\right)\frac{17.59\left(1.059\right)^2\left(2.11\times10^{-4}\right)}{0.008966}\\ &= 0.122\ [\text{Pa}]\end{aligned} \tag{A.134}$$

The total pressure drop for the superheated region is calculated in Equation (A.135)

$$\Delta P_{\text{CC,E2}} = \Delta P_{\text{header}}+\Delta P_{\text{tee}}+\Delta P_{\text{channel}} = 19.3+28.54+0.122 = 48\ [\text{Pa}] = 0.048\ [\text{kPa}] \tag{A.135}$$

Thus, the total pressure drop, area, and number of plates for the chiller are calculated in Equations (A.136) through (A.138):

$$\Delta P_{\text{CC,E}} = \Delta P_{\text{CC,E1}}+\Delta P_{\text{CC,E2}} = 5.605+0.048 = 5.65\ [\text{kPa}] \tag{A.136}$$

$$A_{\text{CC,E}} = A_{\text{CC,E1}}+A_{\text{CC,E2}} = 163.7+0.0264 = 163.73\ [\text{m}^2] \tag{A.137}$$

$$N_{\text{plates}}-1 = \frac{A_{\text{total,E}}}{A_{\text{plate}}} = 1+\frac{163.7}{1.544} = 107.04 = 108\ \text{Plates} \tag{A.138}$$

The calculations for the cooling cycle condenser will be presented next. The working fluid enters as a superheated vapor, becomes two-phase as it rejects heat to the seawater, and exits as a subcooled liquid.

The heat transfer coefficient of superheated working fluid is calculated in Equation (A.139):

$$h_{\text{cc,r,C1}} = 0.2998 Re_{\text{plate}}^{0.645} Pr^{1/3} \frac{k}{D_{\text{hyd}}} = 0.2998(15000)^{0.645}(0.9749)^{1/3}(1.944) = 285.4 \text{ [W m}^{-2}\text{ K}^{-1}\text{]} \quad \text{(A.139)}$$

The seawater side heat transfer coefficient was calculated with Equation (A.140):

$$h_{\text{w,C1}} = 0.023 Re_{\text{plate}}^{0.8} Pr^{0.4} \frac{k_{\text{l}}}{D_{\text{hyd}}} = 0.023(12475)^{0.8}(5.275)^{0.4}(67.6) = 5720 \text{ [W m}^{-2}\text{ K}^{-1}\text{]} \quad \text{(A.140)}$$

Thus, the overall heat transfer coefficient is determined in Equation (A.141):

$$\frac{1}{U_{\text{cc,C1}}} = \frac{1}{h_{\text{cc,r,C1}}} + R_{\text{wall}} + \frac{1}{h_{\text{cc,w,C1}}} = \frac{1}{285.4} + 3.17\times10^{-5} + \frac{1}{5720} = 269.5 \text{ [W m}^{-2}\text{ K}^{-1}\text{]} \quad \text{(A.141)}$$

Then, the number of transfer units for this region was calculated using Equation (A.142):

$$NTU_{\text{cc,C1}} = \frac{1}{C_{\text{r}}-1}\ln\left(\frac{\varepsilon-1}{\varepsilon C_{\text{r}}-1}\right) = \frac{1}{0.005818-1}\ln\left(\frac{0.4672-1}{(0.4672)0.005818-1}\right) = 0.631 \quad \text{(A.142)}$$

The total area of the superheated region of the condenser is calculated with Equation (A.143):

$$A_{\text{cc,C1}} = \frac{(NTU_{\text{cc,C1}})C_{\min}}{U_{\text{cc,C1}}} = \frac{(0.631)6084}{269.5} = 14.24 \text{ [m}^2\text{]} \quad \text{(A.143)}$$

The pressure drop in the superheated region of the condenser was modeled as the sum of the inlet header pressure drop, the pressure drop from the channels to the header, and the pressure drop of the superheated vapor flowing through the plate channels. The pressure drop of the outlet header was calculated using Equation (A.144):

$$\Delta P_{\text{header}} = \rho u_{\text{header}}^2 \left(\frac{K_{\text{tee,line}}}{2} + 2 f_{\text{sp}} \frac{L_{\text{header}}}{D_{\text{header}}}\right) = 13.45\left(\frac{0.9}{2} + (0.00544)\frac{(0.459)}{0.35}\right) = 6.15 \text{ [Pa]} \quad \text{(A.144)}$$

The pressure drop from the working fluid leaving the header and entering the channels is calculated with Equation (A.145):

$$\Delta P_{\text{tee,out}} = \frac{\left(K_{\text{tee,branch}} + K_{\text{con}}\right)\rho u_{\text{channel}}^{2}}{2} = \left(2 + 0.4726\right)\left(\frac{9.22}{2}\right) = 11.4 \text{ [Pa]} \tag{A.145}$$

The length of the superheated region in the condenser is calculated with Equation (A.146):

$$L_{\text{sh}} = \frac{A_{\text{sh}}}{\left(N_{\text{plates}} - 1\right) w_{\text{plate}}} = \frac{14.24}{(89)1.17} = 0.137 \text{ [m]} \tag{A.146}$$

The pressure drop of the superheated vapor flowing through the plate channels was calculated with Equation (A.147):

$$\Delta P_{\text{channel}} = \frac{2 f_{\text{Fanning}} \rho u_{\text{channel}}^{2} L_{\text{sp}}}{D_{\text{h,channel}}} = 2\left(0.1312\right)\frac{54.25\left(0.412\right)^{2}\left(0.137\right)}{0.008966} = 36.92 \text{ [Pa]} \tag{A.147}$$

The total pressure drop in the superheated vapor region of the cooling cycle condenser is then calculated in Equation (A.148):

$$\Delta P_{\text{C1}} = \Delta P_{\text{header}} + \Delta P_{\text{tee,out}} + \Delta P_{\text{channel}} = 6.15 + 11.4 + 36.92 = 54.5 \text{ [Pa]} = 0.0545 \text{ [kPa]} \tag{A.148}$$

In the next region of the condenser, the working fluid is a two-phase mixture. The heat transfer coefficient was calculated using the Kuo correlation for condensing refrigerants in plate heat exchangers, as shown in Equation (A.149):

$$h_{\text{r,cond}} = h_{\text{r,l}}\left[0.25 Co^{-0.45} Fr_{\text{l}}^{0.25} + 75 Bo^{0.75}\right] = 679\left[0.2532 + 1.058\right] = 890.4 \text{ [W m}^{-2}\text{ K}^{-1}\text{]} \tag{A.149}$$

The water side heat transfer coefficient was calculated with Equation (A.150):

$$h_{\text{w,C2}} = 0.023 Re_{\text{plate}}^{0.8} Pr^{0.4} \frac{k_{\text{l}}}{D_{\text{hyd}}} = 0.023\left(12475\right)^{0.8}\left(5.275\right)^{0.4}\left(67.60\right) = 5720 \text{ [W m}^{-2}\text{ K}^{-1}\text{]} \tag{A.150}$$

The overall heat transfer coefficient in this region is then calculated with Equation (A.151):

$$\frac{1}{U_{\text{cc,C2}}}=\frac{1}{h_{\text{r,cond}}}+R_{\text{wall}}+\frac{1}{h_{\text{cc,w,C2}}}=\frac{1}{890.4}+3.17\times10^{-5}+\frac{1}{5720}=752.1\,[\text{W m}^{-2}\ \text{K}^{-1}] \quad \text{(A.151)}$$

The NTU of the two-phase region is then defined in Equation (A.152):

$$NTU_{\text{cc,C2}}=-\ln\left(1-\varepsilon\right)=-\ln\left(1-0.07398\right)=0.0769 \quad \text{(A.152)}$$

The area of the two-phase condenser heat region is calculated with Equation (A.153):

$$A_{\text{cc,C2}}=\frac{NTU_{\text{cc,C2}}\left(C_{\text{water}}\right)}{U_{\text{cc,C2}}}=\frac{0.0769\left(1.046\times10^{6}\right)}{752.1}=106.9\ [\text{m}^2] \quad \text{(A.153)}$$

The pressure drop of this region will be calculated next. The Kuo Friction factor for this region is calculated with Equation (A.154):

$$f_{\text{tp,cond}}=21500Re_{\text{eq}}^{-1.14}Bo^{-0.085}=21500\left(8.85\times10^{-5}\right)\left(1.621\right)=3.084 \quad \text{(A.154)}$$

The length of the two-phase region was calculated with Equation (A.155):

$$L_{\text{tp}}=\frac{A_{\text{tp}}}{\left(N_{\text{plates}}-1\right)w_{\text{plate}}}=\frac{106.9}{\left(90\right)1.17}=1.02\ [\text{m}] \quad \text{(A.155)}$$

Then, the two-phase pressure drop is calculated with Equation (A.156):

$$\Delta P_{\text{tp}}=\frac{2f_{\text{tp}}G^2}{\rho_{\text{mean}}}\frac{L_{\text{tp}}}{D_{\text{h,channel}}}=2\left(3.084\right)\frac{499.9696}{103.5411}\left(\frac{1.02}{0.008966}\right)$$
$$=3388\ [\text{Pa}]=3.388\ [\text{kPa}] \quad \text{(A.156)}$$

In the third region of the condenser, the working fluid is a subcooled liquid. The heat transfer coefficient of the working fluid is calculated with Equation (A.157):

$$h_{\text{cc,r,C3}}=0.2998Re_{\text{plate}}^{0.645}Pr^{1/3}\frac{k}{D_{\text{hyd}}}=0.2998\left(1204\right)^{0.645}\left(3.206\right)^{1/3}\left(8.5925\right)$$
$$=368.6\ [\text{W m}^{-2}\ \text{K}^{-1}] \quad \text{(A.157)}$$

The water side heat transfer coefficient was calculated with Equation (A.158):

$$h_{\mathrm{w,C3}} = 0.023Re_{\mathrm{plate}}^{0.8}Pr^{0.4}\frac{k_{\mathrm{l}}}{D_{\mathrm{hyd}}} = 0.023\left(12695\right)^{0.8}\left(5.17\right)^{0.4}\left(67.7\right) = 5766\ [\mathrm{W\,m^{-2}\,K^{-1}}]$$

(A.158)

Thus, the overall heat transfer coefficient is determined in Equation (A.159):

$$\frac{1}{U_{\mathrm{cc,C3}}} = \frac{1}{h_{\mathrm{cc,r,C3}}} + R_{\mathrm{wall}} + \frac{1}{h_{\mathrm{cc,w,C3}}} = \frac{1}{368.6} + 3.17\times10^{-5} + \frac{1}{5766} = 342.7\ [\mathrm{W\,m^{-2}\ K^{-1}}] \quad (\mathrm{A.159})$$

Then, the number of transfer units for the subcooled region is calculated in Equation (A.160):

$$NTU_{\mathrm{cc,C3}} = \frac{1}{C_{\mathrm{r}}-1}\ln\left(\frac{\varepsilon-1}{\varepsilon C_{\mathrm{r}}-1}\right) = \frac{1}{0.007528-1}\ln\left(\frac{0.485-1}{\left(0.485\right)0.007528-1}\right) = 0.666 \quad (\mathrm{A.160})$$

The area of this region is computed in Equation (A.161):

$$A_{\mathrm{cc,C3}} = \frac{NTU_{\mathrm{cc,C3}}\left(C_{\mathrm{ref}}\right)}{U_{\mathrm{cc,C3}}} = \frac{0.666\left(7873\right)}{342.7} = 15.31\,[\mathrm{m^2}] \quad (\mathrm{A.161})$$

The pressure drop in the subcooled region of the condenser was modeled as the sum of the outlet header pressure drop, the pressure drop from the channels to the header, and the pressure drop of the subcooled liquid flowing through the plate channels. The pressure drop of the outlet header was calculated using Equation (A.162):

$$\begin{aligned}\Delta P_{\mathrm{header}} &= \rho u_{\mathrm{header}}^{2}\left(\frac{K_{\mathrm{tee,line}}}{2} + 2f_{\mathrm{sp}}\frac{L_{\mathrm{header}}}{D_{\mathrm{header}}}\right)\\ &= 0.6424\left(\frac{0.9}{2} + \left(0.005118\right)\frac{\left(0.459\right)}{0.35}\right) = 0.293\,[\mathrm{Pa}]\end{aligned} \quad (\mathrm{A.162})$$

The pressure drop from the working fluid leaving the channels and entering the header is calculated with Equation (A.163):

$$\Delta P_{\mathrm{tee}} = \frac{\left(K_{\mathrm{tee,branch}} + \mathrm{K}_{\mathrm{exp}}\right)\rho u_{\mathrm{channel}}^{2}}{2} = \left(2+0.8935\right)\left(\frac{0.4405}{2}\right) = 0.637\ [\mathrm{Pa}] \quad (\mathrm{A.163})$$

The length of the subcooled region in the condenser is calculated with Equation (A.164):

$$L_{\text{sc}} = \frac{A_{\text{sc}}}{\left(N_{\text{plates}} - 1\right) w_{\text{plate}}} = \frac{15.31}{(90)1.17} = 0.1454\ [\text{m}] \tag{A.164}$$

The pressure drop of the subcooled liquid flowing through the plate channels was calculated with Equation (A.165):

$$\begin{aligned} \Delta P_{\text{channel}} &= \frac{2 f_{\text{Fanning}} \rho u_{\text{channel}}^2 L_{\text{sp}}}{D_{\text{h,channel}}} = 2\left(0.2024\right) \frac{1138\left(0.0197\right)^2 \left(0.1454\right)}{0.008966} \\ &= 2.9\ [\text{Pa}] \end{aligned} \tag{A.165}$$

The total pressure drop in the subcooled region of the cooling cycle condenser is then calculated in Equation (A.166):

$$\begin{aligned} \Delta P_{\text{C3}} &= \Delta P_{\text{header}} + \Delta P_{\text{tee,out}} + \Delta P_{\text{channel}} = 0.239 + 0.637 + 2.9 \\ &= 3.78\ [\text{Pa}] = 0.00378\ [\text{kPa}] \end{aligned} \tag{A.166}$$

The overall pressure drop through the cooling cycle condenser is calculated with Equation (A.167):

$$\Delta P_{\text{C}} = \Delta P_{\text{C1}} + \Delta P_{\text{C2}} + \Delta P_{\text{C3}} = 54.5 + 3388 + 3.78 = 3446\ [\text{Pa}] = 3.446\ [\text{kPa}] \tag{A.167}$$

The total area of the cooling cycle condenser is then calculated with Equation (A.168):

$$A_{\text{total,C}} = A_{\text{sh}} + A_{\text{tp}} + A_{\text{sc}} = 14.24 + 106.9 + 15.31 = 136.5\ [\text{m}^2] \tag{A.168}$$

The number of plates for the power cycle condenser is calculated with Equation (A.169):

$$N_{\text{plates}} - 1 = \frac{A_{\text{total,C}}}{A_{\text{plate}}} = 1 + \frac{136.5}{1.544} = 89.4 = 90\ \text{Plates} \tag{A.169}$$

A.3. Economic Model and Payback Period

After calculating the total heat exchange area, pressure drop, and number of plates for all the heat exchangers, the economic block of the model begins. The cost of the power cycle boiler, power condenser, cooling cycle chiller, and cooling condenser are calculated in Equations (A.170) through (A.173):

$$\begin{aligned} cost_{\text{boiler}} &= 475A^{0.54}F_{\text{mat}}F_{\text{pressure}}F_{\text{gasket}}\frac{CEPCI_{2016}}{CEPCI_{2005}} \\ &= 475\left(2646\right)^{0.54}\left(1\right)\left(1.35\right)\left(1\right)\frac{541.7}{460} = \$53,239 \end{aligned} \tag{A.170}$$

$$\begin{aligned} cost_{\text{pc,cond}} &= 475A^{0.54}F_{\text{mat}}F_{\text{pressure}}F_{\text{gasket}}\frac{CEPCI_{2016}}{CEPCI_{2005}} \\ &= 475\left(3382\right)^{0.54}\left(1.6\right)\left(1\right)\left(1\right)\frac{541.7}{460} = \$72,039 \end{aligned} \tag{A.171}$$

$$\begin{aligned} cost_{\text{chiller}} &= 475A^{0.54}F_{\text{mat}}F_{\text{pressure}}F_{\text{gasket}}\frac{CEPCI_{2016}}{CEPCI_{2005}} \\ &= 475\left(1762\right)^{0.54}\left(1\right)\left(1\right)\left(1\right)\frac{541.7}{460} = \$31,663 \end{aligned} \tag{A.172}$$

$$\begin{aligned} cost_{\text{cc,cond}} &= 475A^{0.54}F_{\text{mat}}F_{\text{pressure}}F_{\text{gasket}}\frac{CEPCI_{2016}}{CEPCI_{2005}} \\ &= 475\left(1469\right)^{0.54}\left(1.6\right)\left(1\right)\left(1\right)\frac{541.7}{460} = \$45,926 \end{aligned} \tag{A.173}$$

The amount of refrigerant in each heat exchanger was calculated based on the internal volume. The refrigerant charge was calculated for the inlet and outlet headers and in each region: subcooled, two-phase, and superheated.

The power cycle boiler charge calculations will be presented first. The charge in the inlet header was calculated using Equation (A.174) and the charge in the outlet header was calculated with Equation (A.175):

$$m_{\text{header,i}} = \rho_{\text{liquid}}\left(\frac{\pi D^2}{4}\right)\times L_{\text{header}} = 919.4\left(\frac{\pi 0.350^2}{4}\right)\left(0.8334\right) = 73.72\text{ [kg]} \tag{A.174}$$

$$m_{\text{header,o}} = \rho_{\text{vapor}}\left(\frac{\pi D^2}{4}\right)\times L_{\text{header}} = 161.0\left(\frac{\pi 0.350^2}{4}\right)\left(0.8334\right) = 12.91\text{ [kg]} \tag{A.175}$$

The charge in the subcooled plates of the boiler was calculated in Equation (A.176):

$$m_{\text{sc}} = \rho_{\text{liquid}}\left(V_{\text{sc}}\right) = \rho\left(A_{\text{sc}}\right)\left(s_{\text{plate}}\right) = 919.4\left(71.20\right)\left(0.0045\right) = 294.6\text{ [kg]} \tag{A.176}$$

The charge in the two-phase plates of the boiler was calculated in Equation (A.177):

$$\begin{aligned} m_{\text{tp}} &= \rho_{\text{ave}}\left(V_{\text{tp}}\right) = \frac{\rho_{\text{liquid}} + \rho_{\text{vapor}}}{2}\left(A_{\text{tp}}\right)\left(s_{\text{plate}}\right) \\ &= \left(540.2\right)\left(139.9\right)\left(0.0045\right) = 340.1\,[\text{kg}] \end{aligned} \tag{A.177}$$

The charge in the superheated region of the boiler was calculated in Equation (A.178):

$$m_{\text{sh}} = \rho_{\text{vapor}}\left(V_{\text{sh}}\right) = \rho\left(A_{\text{sh}}\right)\left(s_{\text{plate}}\right) = 161\left(34.74\right)\left(0.0045\right) = 25.17\ [\text{kg}] \tag{A.178}$$

The total charge in the boiler is then calculated in Equation (A.179):

$$m_{\text{boiler}} = m_{\text{sc}} + m_{\text{tp}} + m_{\text{sh}} + m_{\text{header,i}} + m_{\text{header,o}} = 747\ [\text{kg}] \tag{A.179}$$

From supplier quotes, the cost per kilogram of R134a was found to be \$11 kg^{-1}. Thus, the cost of the refrigerant charge in the boiler is calculated in Equation (A.180):

$$cost_{\text{ref,boiler}} = m_{\text{boiler}}cost_{\text{ref, spec}} = 747\left(11\right) = \$8,217 \tag{A.180}$$

The power cycle condenser charge calculations will be presented next. The charge in the inlet header was calculated using Equation (A.181) and the charge in the outlet header was calculated with Equation (A.182):

$$m_{\text{header,i}} = \rho_{\text{vapor}}\left(\frac{\pi D^2}{4}\right)\times L_{\text{header}} = 53.22\left(\frac{\pi 0.350^2}{4}\right)\left(1.057\right) = 5.41\,[\text{kg}] \tag{A.181}$$

$$m_{\text{header,o}} = \rho_{\text{liquid}}\left(\frac{\pi D^2}{4}\right)\times L_{\text{header}} = 1138\left(\frac{\pi 0.350^2}{4}\right)\left(1.057\right) = 115\ [\text{kg}] \tag{A.182}$$

The charge in the superheated plates of the condenser was calculated in Equation (A.183):

$$m_{\text{sh}} = \rho_{\text{vapor}}\left(V_{\text{sh}}\right) = \rho\left(A_{\text{sh}}\right)\left(s_{\text{plate}}\right) = 53.22\left(6.11\right)\left(0.0045\right) = 1.5\,[\text{kg}] \tag{A.183}$$

The charge in the two-phase plates of the condenser was calculated in Equation (A.184):

$$m_{\text{tp}} = \rho_{\text{ave}}\left(V_{\text{tp}}\right) = \frac{\rho_{\text{liquid}} + \rho_{\text{vapor}}}{2}\left(A_{\text{tp}}\right)\left(s_{\text{plate}}\right) = \left(595.75\right)\left(308\right)\left(0.0045\right) = 826\ [\text{kg}] \tag{A.184}$$

The charge in the subcooled region of the condenser was calculated in Equation (A.185):

$$m_{\mathrm{sc}} = \rho_{\mathrm{liquid}}\left(V_{\mathrm{sc}}\right) = \rho\left(A_{\mathrm{sc}}\right)\left(s_{\mathrm{plate}}\right) = 1138(0.055)(0.0045) = 0.282\ [\mathrm{kg}] \tag{A.185}$$

The total charge in the condenser is then calculated in Equation (A.186):

$$m_{\mathrm{pc,cond}} = m_{\mathrm{sh}} + m_{\mathrm{tp}} + m_{\mathrm{sc}} + m_{\mathrm{header,i}} + m_{\mathrm{header,o}} = 948\ [\mathrm{kg}] \tag{A.186}$$

The total cost of the refrigerant in the condenser is then Equation (A.187):

$$cost_{\mathrm{ref,pc,cond}} = m_{\mathrm{pc,cond}} cost_{\mathrm{ref,\ spec}} = 948(11) = \$10,428 \tag{A.187}$$

The evaporator on the cooling cycle was two-phase at the inlet header and superheated at the outlet header. The mass of refrigerant in the inlet and outlet headers was calculated according to Equation (A.188) and (A.189):

$$m_{\mathrm{header,i}} = \rho_{\mathrm{ave}}\left(\frac{\pi D^2}{4}\right) \times L_{\mathrm{header}} = 45.1\left(\frac{\pi 0.350^2}{4}\right)(0.5526) = 2.40\ [\mathrm{kg}] \tag{A.188}$$

$$m_{\mathrm{header,o}} = \rho_{\mathrm{vapor}}\left(\frac{\pi D^2}{4}\right) \times L_{\mathrm{header}} = 17.32\left(\frac{\pi 0.350^2}{4}\right)(0.5526) = 0.921\ [\mathrm{kg}] \tag{A.189}$$

The term ρ_{ave} is equal to Equation (A.190):

$$\rho_{\mathrm{ave}} = 0.5\left[\rho_{x=0.2307} + \rho_{x=1}\right] = 45.1 \tag{A.190}$$

The charge in the two-phase region of the plate channels in the chiller was calculated in Equation (A.191):

$$m_{\mathrm{tp}} = \rho_{\mathrm{ave}}\left(V_{\mathrm{tp}}\right) = \rho_{\mathrm{ave}}\left(A_{\mathrm{tp}}\right)\left(s_{\mathrm{plate}}\right) = (45.1)(163.7)(0.0045) = 33.2\ [\mathrm{kg}] \tag{A.191}$$

The charge in the superheated vapor region of the channels was calculated in Equation (A.192):

$$m_{\mathrm{sh}} = \rho_{\mathrm{vapor}}\left(V_{\mathrm{sh}}\right) = \rho\left(A_{\mathrm{sh}}\right)\left(s_{\mathrm{plate}}\right) = 17.32(0.0264)(0.0045) = 0.002\ [\mathrm{kg}] \tag{A.192}$$

Then, the total mass of refrigerant in the chiller is calculated with Equation (A.193):

$$m_{\mathrm{chiller}} = m_{\mathrm{sh}} + m_{\mathrm{tp}} + m_{\mathrm{header,i}} + m_{\mathrm{header,o}} = 36.5\ [\mathrm{kg}] \tag{A.193}$$

The total cost of the refrigerant in the chiller is then calculated in Equation (A.194):

$$cost_{\text{ref,chiller}} = m_{\text{chiller}} cost_{\text{ref, spec}} = 36.5(11) = \$402 \quad \text{(A.194)}$$

The refrigerant charge calculations in the cooling condenser will be presented next. The mass of refrigerant in the inlet and outlet headers is calculated in Equations (A.195) and (A.196):

$$m_{\text{header,i}} = \rho_{\text{vapor}} \left(\frac{\pi D^2}{4} \right) \times L_{\text{header}} = 54.25 \left(\frac{\pi 0.350^2}{4} \right) (0.459) = 2.40 \text{ [kg]} \quad \text{(A.195)}$$

$$m_{\text{header,o}} = \rho_{\text{liquid}} \left(\frac{\pi D^2}{4} \right) \times L_{\text{header}} = 1135 \left(\frac{\pi 0.350^2}{4} \right) (0.459) = 50.12 \text{ [kg]} \quad \text{(A.196)}$$

The charge in the superheated vapor region is calculated as Equation (A.197):

$$m_{\text{sh}} = \rho_{\text{vapor}} (V_{\text{sh}}) = \rho (A_{\text{sh}}) (s_{\text{plate}}) = 54.25(14.24)(0.0045) = 3.48 \text{ [kg]} \quad \text{(A.197)}$$

The charge in the two-phase region was calculated with Equation (A.198):

$$m_{\text{tp}} = \rho_{\text{ave}} (V_{\text{tp}}) = \frac{\rho_{\text{liquid}} + \rho_{\text{vapor}}}{2} (A_{\text{tp}}) (s_{\text{plate}}) = (594.3)(106.9)(0.0045) = 286 \text{ [kg]} \quad \text{(A.198)}$$

The charge in the subcooled region was calculated with Equation (A.199):

$$m_{\text{sc}} = \rho_{\text{liquid}} (V_{\text{sc}}) = \rho (A_{\text{sc}}) (s_{\text{plate}}) = 1135(15.31)(0.0045) = 78.2 \text{ [kg]} \quad \text{(A.199)}$$

The total charge in the cooling condenser is then calculated with Equation (A.200):

$$m_{\text{cc,cond}} = m_{\text{sh}} + m_{\text{tp}} + m_{\text{sc}} + m_{\text{header,i}} + m_{\text{header,o}} = 420.2 \text{ [kg]} \quad \text{(A.200)}$$

Thus, the total cost of refrigerant in the cooling condenser is calculating using Equation (A.201):

$$cost_{\text{ref,cc,cond}} = m_{\text{cc,cond}} cost_{\text{ref,spec}} = 420.20(11) = \$4622 \quad \text{(A.201)}$$

Based on the diameter, length, and working fluid phase in the piping in this system, the total charge was calculated to be 26 kg, yielding a cost of \$286. The total cost of refrigerant in this system is then shown in Equation (A.202):

$$cost_{\text{ref}} = cost_{\text{ref,HX}} + cost_{\text{ref,pipe}} = \$23,937 \quad \text{(A.202)}$$

The cost of the pump, turbocompressor, and piping will be presented next. The cost of the pump is calculated according to Equation (A.203):

$$cost_{\text{pump}} = F_{\text{type}} cost_{\text{base}} \frac{CEPCI_{2016}}{CEPCI_{1985}} = 1.853(2483)\frac{541.7}{325} = \$7,669 \tag{A.203}$$

The cost of the turbocompressor was calculated with Equation (A.204):

$$cost_{\text{TC}} = cost_{6kW}\left(\frac{\dot{W}_{\text{actual}}}{6kW}\right)^{\frac{\log\left(\frac{Cost10kW}{Cost6kW}\right)}{\log\left(\frac{10kW}{6kW}\right)}} = 2620\left(\frac{161.12}{6}\right)^{0.356915} = \$8,479 \tag{A.204}$$

The cost of the piping depends on the length, diameter, and number of fittings. The total cost of piping in the system was calculated to be \$5,164. Thus, the total system cost was calculated in Equation (A.205):

$$Cost_{\text{total}} = cost_{\text{HX}} + cost_{\text{pump}} + cost_{\text{TC}} + cost_{\text{piping}} + cost_{\text{refrigerant}} = \$247,819 \tag{A.205}$$

After finding the total system cost, the payback period can be determined. The first step to determining the payback period is to calculate how much power the turbo-compression cooling system would displace from the vapor compression chillers onboard the cargo ship. Equation (A.206) is used to calculate the amount of power displaced:

$$\dot{W}_{\text{displaced}} = 0.85\left(\frac{\dot{Q}_{\text{chiller}}}{COP_{\text{refrigeration}}} - \dot{W}_{\text{pump}}\right) = 0.85\left(\frac{774.9}{4} - 20.46\right) = 147.3\ [\text{kW}] \tag{A.206}$$

The amount of power displaced is divided by the efficiency of the power transfer from diesel engine to the generator to determine the required engine power input, shown in Equation (A.207):

$$\dot{W}_{\text{engine}} = \frac{\dot{W}_{\text{displaced}}}{\eta_{\text{generator}}} = \frac{147.3}{0.975} = 151.1\ [\text{kW}] \tag{A.207}$$

After this, the engine power is divided by the thermal efficiency of the diesel engine to determine the required heat input, as shown in Equation (A.208):

$$\dot{Q}_{\mathrm{in}} = \frac{\dot{W}_{\mathrm{engine}}}{\eta_{\mathrm{thermal}}} = \frac{151.1}{0.40} = 378\ [\mathrm{kW}] \tag{A.208}$$

The required mass flow rate of fuel to deliver this heat input is calculated by dividing the heat input by the average lower heating value for Marine Gas Oil, as shown in Equation (A.209):

$$\dot{m}_{\mathrm{fuel}} = \frac{\dot{Q}_{\mathrm{in}}}{Q_{\mathrm{MGO,ave}}} = \frac{378}{4.281\times10^{4}} = 0.00882\ [\mathrm{kg\ s^{-1}}] \tag{A.209}$$

The mass flow rate was converted to a yearly mass flow to understand how much fuel would be used per year. After this, the yearly mass flow rate was multiplied by the specific cost of the fuel to determine the annual cost savings from implementing a turbo-compression cooling system, as shown in Equation (A.210):

$$cost_{\mathrm{savings}} = \dot{m}_{\mathrm{fuel}} cost_{\mathrm{MGO}} = 278147\left(0.5335\right) = \$148,392\ \text{per year} \tag{A.210}$$

Thus, the simple payback period of the system was calculated using Equation (A.211):

$$\text{Payback Period} = \frac{cost_{\mathrm{totalsystem}}}{cost_{\mathrm{savings}}} = \frac{\$247,819}{\$148,392\,\text{per year}} = 1.67\ [\text{years}] \tag{A.211}$$

Table A-3 shows the cost of each major component in the turbo-compression cooling system with R134a.

This concludes the representative calculation for the liquid coupled turbo-compression cooling system applied to a cargo ship using R134a as the working fluid. The results from the representative calculation are compared with the results from the EES model in Table A-4.

Table A-3: Cost for each component in the optimized design point with R134a. Cost per kW_{th} is based on the cooling duty of the chiller.

Component	**Cost**	**Cost per kW_{th}**
Boiler	$53,239	$68.71
Chiller	$31,663	$40.87
Condenser - CC	$45,926	$59.27
Condenser - PC	$72,039	$92.98
Piping	$5,164	$6.66
Pump	$7,669	$9.90
Refrigerant Charge	$23,937	$30.89
Turbocompressor	$8,479	$10.94
Total	$247,819	$320.22

Table A-4: Comparison of results between the representative calculation and the EES simulation.

Values	***Hand Result***	***EES Result***	***Unit***
$\dot{W}_{\text{turbine}}$	162	161	kW
$Q_{\text{pc,cond}}$	1861	1859	kW
$Q_{\text{pc,boiler}}$	2000	2000	kW
$\dot{W}_{\text{pump}}$	21	21	kW
$Q_{\text{cc,cond}}$	928	928	kW
$\text{Q}_{\text{cc,chiller}}$	775	775	kW
$\dot{W}_{\text{comp}}$	153	153	kW
N	27887	27887	rpm
Ds_{turb}	1.30	1.30	lbf$^{1/4}$ s$^{1/2}$ lbm$^{-1/4}$ ft$^{-1/4}$
Ns_{comp}	108.7	108.7	ft$^{3/4}$ lbm$^{3/4}$ min^{-1} s$^{-1/2}$ lbf$^{-3/4}$
Ds_{comp}	1.56	1.56	lbf$^{1/4}$ s$^{1/2}$ lbm$^{-1/4}$ ft$^{-1/4}$
A_{boiler}	248.5	248.3	m^2
$A_{\text{pc,cond}}$	314.2	314.4	m^2
A_{chiller}	163.7	163.7	m^2
$A_{\text{cc,cond}}$	136.5	136.4	m^2
ΔP_{boiler}	0.768	0.769	kPa
$\Delta P_{\text{pc,cond}}$	4.23	4.27	kPa
$\Delta P_{\text{chiller}}$	5.65	5.66	kPa
$\Delta P_{\text{cc,cond}}$	3.45	3.50	kPa
$cost_{\text{total}}$	247,819	249,248	dollars
Payback Period	1.67	1.68	years

A.4. Kern Method for Shell and Tube Heat Exchanger Design

The results from the shell and tube heat exchanger sizing model will be confirmed in this section. The tube side heat transfer coefficient for the seawater was calculated using the Dittus-Boelter correlation for a fluid being heated, as shown in Equation:

$$h_{\text{tube}} = 0.023 Re_{\text{tube}}^{0.8} Pr^{0.4} \left(\frac{k}{D_{\text{h,tube}}} \right) = 0.023(18687)(1.65)(8.27) \\ = 6916\ [\text{W}\,\text{m}^{-2}\ \text{K}] \tag{A.212}$$

The pressure drop of the tube side was calculated using Equation (A.213):

$$\Delta P_{\text{tube}} = \frac{2 f \rho u^2 L_{\text{tube}}}{D_{\text{i,tube}}} = \frac{2(0.0037)995(5.26)5.029}{0.07326} \\ = 2658\ [\text{Pa}] = 2.66\ [\text{kPa}] \tag{A.213}$$

According to the Kern method, the cross sectional flow area of the shell is defined in Equation (A.214):

$$A_{\text{c,shell}} = \frac{D_{\text{i,shell}}}{P_{\text{tube}}} C^1 L_{\text{baffle}} = 0.288\ [\text{m}^2] \tag{A.214}$$

where C^1 is defined as the outer diameter of the tube subtracted from the tube pitch. Then, the shell side mass flux is calculated with Equation (A.215):

$$\dot{m}'' = \frac{\dot{m}}{A_{\text{c,shell}}} = 272.6\ [\text{kg s}^{-1}\ \text{m}^{-2}] \tag{A.215}$$

Then, the hydraulic diameter of the shell side is calculated with Equation (A.216):

$$D_{\text{h,shell}} = 4 \frac{\left(P_{\text{tube}}^2 - \frac{\pi D_{\text{o,tube}}^2}{4} \right)}{\pi D_{\text{o,tube}}} = 0.08753\ [\text{m}] \tag{A.216}$$

Then, the Reynolds number for the shell side engine coolant flow is calculated with Equation (A.217):

$$Re_{\text{shell}} = \frac{\dot{m}'' D_{\text{h,shell}}}{\mu} = 75860 \tag{A.217}$$

Finally, the heat transfer coefficient of the shell side can be calcualated with Equation (A.218):

$$\begin{aligned} h_{\text{shell}} &= 0.36 Re_{\text{shell}}^{0.55} Pr^{1/3} \left(\frac{k}{D_{\text{h,shell}}} \right) = 0.36(483.1)1.26(7.5551) \\ &= 1656 \text{ [W m}^{-2}\text{ K}^{-1}\text{]} \end{aligned} \tag{A.218}$$

Then, the pressure drop of the shell side flow is calculated with Equation (A.219):

$$\begin{aligned} \Delta P_{\text{shell}} &= 4 \frac{f_{\text{shell}} \left(\dot{m}''\right)^2 D_{\text{i,shell}} \left(N_{\text{baffle}} + 1\right)}{2 \rho D_{\text{h,shell}}} = 2 \frac{0.0492(74310.8)2.5(10)}{965.3(0.08753)} \\ &= 2164 \text{ [Pa]} = 2.2 \text{ [kPa]} \end{aligned} \tag{A.219}$$

The overall heat transfer coefficient of this shell and tube heat exchanger is then calculated with Equation (A.220):

$$\frac{1}{U} = \frac{1}{h_{\text{tube}}} + R_{\text{wall}} + \frac{1}{h_{\text{shell}}} = 1257.3 \text{ [W m}^{-2}\text{ K}^{-1}\text{]} \tag{A.220}$$

The results from this representative calculation are compared to the EES model in Table A-5.

Table A-5: Comparison of results between the representative calculation and the EES simulation.

Values	***Hand Result***	***EES Result***	***Unit***
h_{tube}	6916	6918	W m^{-2} K^{-1}
h_{shell}	1656	1654	W m^{-2} K^{-1}
ΔP_{tube}	2.7	2.6	kPa
ΔP_{shell}	2.2	2.2	kPa
U	1257	1256	W m^{-2} K^{-1}

APPENDIX B. Thermodynamic State Points for Turbo-Compression Cooling Systems

The following section provides the thermodynamic state points for each turbo-compression cooling system that was simulated with various working fluids.

Table B-1: State points for payback period optimized turbo-compression cooling system with R134a.

R134a	**Cooling Cycle**				**Power Cycle**			
	Temperature	**Enthalpy**	**Pressure**	**Entropy**	**Temperature**	**Enthalpy**	**Pressure**	**Entropy**
	°C	**kJ kg^{-1}**	**kPa**	**kJ kg^{-1} K^{-1}**	**°C**	**kJ kg^{-1}**	**kPa**	**kJ kg^{-1} K^{-1}**
1	5.3	253.5	353	0.9288	84.7	287.4	2699	0.907
2	52.1	283.0	1097	0.9471	43.1	273.3	1077	0.9181
3	52.1	283.0	1096	0.9472	43.1	273.3	1076	0.9182
4	42.8	272.5	1096	0.9143	42.1	272.2	1076	0.9146
5	42.7	112.3	1092	0.4074	42.0	111.2	1072	0.4041
6	37.4	104.4	1092	0.3824	42.0	111.2	1072	0.4041
7	37.4	104.4	1091	0.3824	41.9	111.2	1071	0.4041
8	5.8	104.4	360	0.393	43.4	113.0	2702	0.4052
9	5.8	104.4	359	0.393	43.4	113.0	2701	0.4052
10	5.3	253.5	354	0.9286	81.2	176.5	2701	0.5941
11	5.3	253.5	354	0.9286	81.2	280.4	2700	0.8875
12	-	-	-	0.9286	84.7	287.4	2700	0.907

Table B-2: State points for payback period optimized turbo-compression cooling system with R245fa.

R245fa	**Cooling Cycle**				**Power Cycle**			
	Temperature	**Enthalpy**	**Pressure**	**Entropy**	**Temperature**	**Enthalpy**	**Pressure**	**Entropy**
	°C	**kJ kg^{-1}**	**kPa**	**kJ kg^{-1} K^{-1}**	**°C**	**kJ kg^{-1}**	**kPa**	**kJ kg^{-1} K^{-1}**
1	0.5	404.9	53.4	1.750	82.2	465.3	752.4	1.792
2	47.7	440.5	281.8	1.772	59.1	451.6	300.5	1.803
3	47.6	440.5	280.8	1.772	59.1	451.6	299.5	1.803
4	43.6	436.4	280.8	1.759	45.6	437.8	299.4	1.760
5	42.1	255.5	267.7	1.188	44.4	258.5	287.6	1.198
6	40.3	253.0	267.7	1.180	44.3	258.5	287.6	1.198
7	40.3	253.0	266.7	1.180	44.3	258.5	286.6	1.198
8	6.1	253.0	69.3	1.190	44.6	259.0	757.2	1.198
9	5.7	253.0	68.3	1.190	44.6	259.0	756.2	1.198
10	0.6	404.9	54.4	1.748	78.2	306.6	756.1	1.340
11	0.6	404.9	54.4	1.749	78.1	460.4	753.5	1.778
12	-	-	-	-	82.2	465.3	753.4	1.792

Table B-3: State points for payback period optimized turbo-compression cooling system with R1234ze(E).

R1234ze(E)	**Cooling Cycle**				**Power Cycle**			
	Temperature	**Enthalpy**	**Pressure**	**Entropy**	**Temperature**	**Enthalpy**	**Pressure**	**Entropy**
	°C	**kJ kg^{-1}**	**kPa**	**kJ kg^{-1} K^{-1}**	**°C**	**kJ kg^{-1}**	**kPa**	**kJ kg^{-1} K^{-1}**
1	5.0	387.8	260.9	1.675	81.5	429.2	2071.0	1.685
2	41.9	412.7	755.5	1.691	46.2	415.8	821.3	1.696
3	41.9	412.7	754.5	1.691	46.1	415.8	820.3	1.696
4	42.5	411.3	754.5	1.686	42.5	411.3	820.2	1.681
5	39.2	254.5	750.2	1.185	42.3	259.0	815.8	1.199
6	35.1	248.6	750.2	1.166	42.3	259.0	815.8	1.199
7	35.1	248.6	749.2	1.166	42.2	259.0	814.8	1.199
8	5.9	248.6	269.4	1.174	43.3	260.4	2074.0	1.200
9	5.8	248.6	268.4	1.174	43.3	260.4	2073.0	1.200
10	5.1	387.6	261.9	1.674	81.5	320.9	2073.0	1.380
11	5.3	387.8	261.9	1.674	81.5	427.7	2072.0	1.681
12	-	-	-	-	81.6	429.2	2072.0	1.685

Table B-4: State points for payback period optimized turbo-compression cooling system with R152a.

R152a	**Cooling Cycle**				**Power Cycle**			
	Temperature	**Enthalpy**	**Pressure**	**Entropy**	**Temperature**	**Enthalpy**	**Pressure**	**Entropy**
	°C	**kJ kg^{-1}**	**kPa**	**kJ kg^{-1} K^{-1}**	**°C**	**kJ kg^{-1}**	**kPa**	**kJ kg^{-1} K^{-1}**
1	4.7	509.8	311.7	2.115	87.5	567.7	2072.0	2.099
2	61.9	558.7	1013.0	2.145	54.8	548.5	1017.0	2.114
3	61.9	558.7	1012.0	2.145	54.8	548.5	1016.0	2.114
4	44.0	532.9	1012.0	2.066	44.2	533.0	1016.0	2.066
5	43.9	279.1	1008.0	1.265	44.0	279.4	1011.0	1.266
6	38.4	268.6	1008.0	1.232	44.0	279.3	1011.0	1.266
7	38.4	268.6	1007.0	1.232	44.0	279.3	1010.0	1.266
8	5.4	268.6	319.1	1.247	44.9	280.9	2075.0	1.267
9	5.3	268.6	318.1	1.247	44.9	280.9	2074.0	1.267
10	4.8	509.8	312.7	2.115	74.3	341.2	2074.0	1.448
11	4.8	509.8	312.7	2.115	74.3	542.9	2074.0	2.029
12	-	-	-	-	87.5	567.7	2073.0	2.099

Table B-5: State points for payback period optimized turbo-compression cooling system with R600a.

R600a	**Cooling Cycle**				**Power Cycle**			
	Temperature	**Enthalpy**	**Pressure**	**Entropy**	**Temperature**	**Enthalpy**	**Pressure**	**Entropy**
	°C	**kJ kg^{-1}**	**kPa**	**kJ kg^{-1} K^{-1}**	**°C**	**kJ kg^{-1}**	**kPa**	**kJ kg^{-1} K^{-1}**
1	4.4	561.0	181.8	2.301	86.3	678.0	1224.0	2.431
2	44.1	614.9	567.7	2.335	64.6	654.2	600.3	2.449
3	44.1	614.9	566.7	2.336	64.6	654.2	599.3	2.449
4	42.5	611.7	566.6	2.326	44.7	614.6	599.2	2.328
5	42.1	302.5	561.0	1.346	44.4	308.2	594.2	1.364
6	37.8	291.4	561.0	1.311	44.3	308.2	594.2	1.364
7	37.8	291.4	560.0	1.311	44.3	308.2	593.2	1.364
8	5.6	291.4	190.4	1.328	44.9	309.7	1227.0	1.365
9	5.5	291.4	189.4	1.328	44.9	309.7	1226.0	1.365
10	4.4	561.0	182.9	2.301	75.7	393.2	1226.0	1.615
11	4.4	561.0	182.8	2.301	75.6	653.0	1225.0	2.360
12	-	-	-	-	86.3	678.0	1225.0	2.431